Monolayer MoS_2 and MoS_2/Quantum Dot hybrids: novel optoelectronic materials

By

Dhiraj Kumar Prasai

Dissertation
Submitted to the Faculty of the
Graduate School of Vanderbilt University
in partial fulfillment of the requirements
for the degree of

DOCTOR OF PHILOSOPHY
in

Interdisciplinary Materials Science
December, 2015
Nashville, Tennessee

Approved:

Professor Kirill I. Bolotin

Professor Jason G. Valentine

Professor G. Kane Jennings

Professor Richard F. Haglund Jr.

Professor Sharon M.Weiss

Copyright © 2015 by Dhiraj Prasai

ACKNOWLEDGEMENTS

The work presented in this thesis would not have been possible without the guidance and support of my friends and colleagues that I came to know during my tenure at Vanderbilt.

I am most thankful to my advisor, Dr. Kirill Bolotin, for taking me under his wing and shaping me into a curious and ethical scientist. I still remember the early days in the lab when he counseled me to consider him my “scientific father.” He has been much more than that. His sheer passion and relentless nature has pushed me into achieving things I didn’t think was possible. I will never forget writing 100+ drafts for my first paper, which in the end was all worth it. He taught me to consider research an art and to strive for scientific relevance rather than publicity. I consider myself very fortunate to have worked with one of the innovators in the field of 2D materials research.

I would like to thank Dr. AKM Newaz and Dr. Hiram Conley for mentoring me throughout my graduate career. They are possibly two of the most humble and patient teachers I have encountered. They have taught me everything I know about fabrication to running experiments. The countless discussion I had with them conjured up some of our most innovative works. I would also like to thank Alex Wynn, Ryan Nicholl and Andrey Klots for being great friends and group members to collaborate with. I will especially miss the great lunch conversations with Andrey in topics varying from Southpark to Idiocracy to the crazy boarding school experiences only to end up at quantum mechanics.

Dr. Hmelo, Dr. Schmidt, Dr. Choi, and Dr. Koktysh have also been of immense help throughout my graduate career. Thank you for being compliant to all of my peculiar and perhaps

galling VINSE demands. Without their help and support none of the device fabrication would have been possible.

The whole graduate school experience has been a memorable experience, thanks to my friends outside of the lab. Friday night pool at Sportsmans with Subhav, Suraj, Krishen, Brandon, Scotsman and Dima always made for good laugher and fun. The soccer crew (Gabe, Matt, Nano, Jeremy, Kevin, Adam, Jay) have all been great friends and I will miss the great games we had at below freezing temperatures at 7am. I will always cherish the moments shared with Parikshit, who joined the IMS program with me. It was always refreshing to meet outside of work and embrace the madness of graduate school and laugh at our offbeat humor.

My parents, Prahlad Prasai and Sita Prasai, have been nothing but a constant source of love and support. Thank you for always supporting my decision to go to graduate school and instilling a value for education in me. I would like to thank my brothers, Suraj and Niraj for always encouraging me on and making me see the bigger picture. My nephew, Aayan and niece, Aanya have also been a constant source of joy and humor. When things were tough, their goofiness always put a smile on my face.

Last but not the least; I would like to thank my loving wife, best friend, and partner in crime, Pranita Mishra, for keeping me sane and grounded. To steal a line from Radiohead “you are my center when I spin away…”

TABLE OF CONTENTS

Page

Acknowledgements ... iii

List of Figures ... viii

List of Publications ... xiii

Chapter 1: Introduction

1.1 Motivation ... 1
1.2 Carbon allotropes ... 2
1.3 Graphene band structure and its field effect ... 3
1.4 Molybdenum Disulfide (MoS_2) ... 7
1.5 Optics of MoS_2 ... 11
1.6 Photoluminescence and absorption of MoS_2 ... 12

Outline of the document ... 14

Chapter 2: Graphene as an anticorrosive coating

2.1 Introduction ... 17
2.2 Graphene: thinnest corrosion inhibiting coating ... 17
2.3 Electrochemical measurement setup ... 18
2.4 Cyclic voltammetry of Graphene/Cu samples ... 19
2.5 Tafel and corrosion rate calculation ... 23
2.6 Electrochemical impedance spectroscopy (EIS) and modeling corrosion pathways ... 26
2.7 Conclusion and future work ... 28

Chapter 3: Improving carrier mobility and identifying scattering mechanisms in MoS_2

3.1 Introduction ... 30
3.2 Field effect and Hall mobility in MoS_2 ... 30
3.3 Fabrication of high quality MoS_2 Hall-bar devices ... 32
3.4 Temperature dependent Hall-mobility ... 34
3.5 Mobility limiting factors ... 35
i. Contact Resistance (R_c) ... 35
ii. Phonons in MoS_2 ... 36
3.6 Metal to insulator (MIT) transition in MoS_2 ... 37
3.7 MoS_2 substrate engineering towards increasing mobility ... 38
3.8 Dual gated MoS_2 for suppress Coulomb scattering ... 43
3.9 Conclusion and future work ... 44

Chapter 4: Electrical control of optical properties of monolayer MoS_2

4.1 Introduction 47
4.2 PL modulation in MoS_2-FETs..48
4.3 Absorption modulation in MoS_2-FETs 49
4.4 Elucidating mechanism of PL/absorption modulation 51
4.5 Power dependent PL modulation in MoS_2 53
4.6 Trions in MoS_2 53
4.7 Conclusion and future work 55

Chapter 5: Electrical Control of near-Field Energy Transfer between Quantum Dots and monolayer MoS_2

5.1 Introduction 56
5.2 Förster resonant energy transfer (FRET) between MoS_2 and QDs 57
5.3 Experimental evidence of FRET 60
5.4 Electrical modulation of FRET 62
5.5 FRET modulation and MoS_2 absorption 64
5.6 Elucidating mechanism of QD PL modulation 69
5.7 Spectral selectivity of FRET 70
5.8 Conclusion and future work 72

Chapter 6: Future directions and conclusion

6.1 Thesis summary..74
6.2 Future directions: bandgap engineering in MoS_2 via vertical electrical fields. 74
6.3 Towards bandgap engineering in MoS_2: device geometries 77
6.4 Many body effects in TMDCs at high carrier density...79
6.5 Conclusion..81

Appendix

Fabrication and characterization

A1. Mechanical Exfoliation 82
A2. Raman Characterization 83
A3. Chemical vapor deposition..84
i. Monolayer graphene growth
ii. 3D graphene graphene growth
iii. Monolayer MoS_2 growth
A4. Polymer assisted transfer of 2D materials 89
A5. Suspending monolayer flakes and films..90
i. Dry transfer technique
ii. Wet technique: BOE and critical point drying
iii. Polymer free transfer for TEM/STEM samples
A6. Transfer of 2D material using PDMS stamping 97

i. Preparation of transfer slide
ii. Transfer of 2D flakes
A7. He-cryostate for low temperature measurements 100
A8. CdSSe QD fabrication 103
A9. QD layer fabrication 104
A10. Electrically contacted QD/MoS_2 layer fabrication 106
A11. Polymer-electrolyte ionic gating 106

REFERENCES 108

LIST OF FIGURES

Figure 1.1 (a) Schematic view of sp^3hybridization. (b) Crystal structure of diamond (2 interpenetrating fcc lattices). (c) sp^2 hybridization. (d) 2D honeycomb structure of graphene. Graphite, a stack of graphene. Carbon nanotubes, a rolled up version of graphene or wrapped up into a 0D buckyball. Figure acquired from reference [9]. 3

Figure 1.2 (a) Schematic view of the first Brillouin zone in the reciprocal latticeof graphene (b) Schematic of a graphene-FET (b) Ambipolar field effect in graphene. Cones representing bandstructure of graphene at the K point. Shaded region shows relative position of E_f at different external gate voltage (d) Quantum Hall effect for massless Dirac fermions in graphene. Figure acquired from reference [13] 6

Figure 1.3 (a) Lattice structure of MoS_2 (b) A top view of the monolayer MoS_2 lattice, (c) Band Structure of bulk and monolayer-MoS_2 as calculated from density functional theory. Arrows indicate fundamental bandgap (Indirect for bulk, direct for monolayer-MoS_2). Figure acquired from reference [16] (d) Bandstructure schematics of MoS_2 near K-point illustrating the origin of band-edge A- and B-excitons..9

Figure 1.4 Field effect in MoS_2 with n-type channel with large ~10^6 ON/OFF ratios. Inset shows the relative position of E_F at different Vg at the K-point..10

Figure 1.5 (a) Calculated mobility as a function of temperature for monolayer MoS_2. Black curve represents mobility vs temperature when scattering off of both acoustic and optical phonons is included. Red curve represents mobility when optical phonons are quenched. Blue curve represents mobility when only acoustic phonons are present. Figure acquired from reference [17](b) Comparing mobility and ON/OFF ratio of TMDCs with other materials researched for unconventional electronics. Figure acquired from reference [18]. 11

Figure 1.6 (a) Optical microscopy image of monolayer MoS_2 on SiO_2/Si. Scale bar is 10µm (b) Corresponding photoluminescence image. (c) Bandstructure of monolayer MoS_2 around the K-point. Valence band is split by ~200meV due to strong orbit interaction (d) Absorption spectra of MoS_2 dominated by A, B-excitonic peaks (e) Photoluminescence spectra of MoS_2 dominated by A peak, the ground state of MoS_2. 13

Figure 2.1 (a) Gr/Cu sample prepared via chemical vapor deposition, and its Raman spectrum exhibiting characteristic G and 2D peaks. Inset representing schematic of foils mounted onto PTFE 3-electrode cell where copper tape(1) is attached to the sample and $0.4cm^2$ of active area (2) is exposed to the $NaSO_4$ electrolyte. 19

Figure 2.2 (a) Cyclic Voltammetry measurements (electrolyte is 0.1M Na_2SO_4) in the potential window -700 to 200 mV for bare Cu and Gr/Cu samples. Blue line corresponds to the measurement with nitrogen bubbled through the solution. (b) XPS core level spectrum of Cu (Ambient), Cu (100mV) and Cu(Sputter Cleaned), region (i) displaying shoulder due to CuO,

region (ii) peaks due to Cu_2O/Metallic Cu (c) SEM images of Cu and Gr/Cu sample before and after CV scan.. 21

Figure 2.3 (a) Tafel plots of Cu and Gr/Cu samples. Best fits are represented by dotted lines. Inset: Raman spectrum of the Gr/Cu sample after completing Tafel analysis displays small defect-related “D” peaks. (b) Corrosion rates of Cu and Gr/Cu samples extracted from Tafel plots. (c) Corrosion rate of Ni and Graphene transferred onto Ni substrate. 25

Figure 2.4 (a) Bode Magnitude plots of Gr/SiO_2, Cu and Gr/Cu samples (solid symbols). Best fits to the equivalent circuit models are solid lines. (b) Equivalent circuit model used in modeling Gr/SiO_2 devices. (c) Equivalent circuit model for Cu and Gr/Cu devices. 27

Figure 3.1 (a) Optical image of a two-probe MoS_2-FET with Au-contacts. (b) Source-drain current vs. V_g of MoS_2 FET. Inset: linear I_{SD} vs. V_{SD} for various V_g values. 31

Figure 3.2 (a) Large MoS_2 flake after patterning a PMMA Hall bar (Scale Bar is 10μm) (b) PMMA/MoS_2 flake after O_2 plasma etch. (c) After PMMA removal using acetone. (d) Final MoS_2 device with Cr/Au metal contacts. Resistivity (e) Finished multiprobe MoS_2-FET on SiO_2/Si substrate. 33

Figure 3.3 (a) Hall voltage V_{xy} versus magnetic field B for various values of Vg measured at T=2K (b) Carrier density (calculated from Hall measurements) vs V_g. The capacitance calculated from slope of carrier density (n) vs V_g gives us Cg = 105 aFμm^{-2}. (c) Hall Mobility vs V_g at different temperature’s (d) Field effect mobility vs V_g at various temperatures. 34

Figure 3.4 Sample and contact resistance vs. V_g at various temperatures. Dotted lines are contact resistance values. Solid lines are sample resistance from Hall measurements 36

Figure 3.5 μ_{HALL} vs temperature plotted in log scale. Phonon limited mobility (>100K) modelled using $\mu \sim T^{-\gamma}$, γ=1.09. 37

Figure 3.6 Conductivity as a function of V_g at different temperatures showing metal-insulator transition in monolayer MoS_2. 38

Figure 3.7 (a) Field effect in MoS_2/SiO_2 devices (b) Field effect in MoS_2/BN devices................39

Figure 3.8 (a) Optical image of MoS_2/BN device. MoS_2 highlighted with white dotted line. (b) Electrical transport in MoS_2/BN device with Cr/Au contacts. Inset: photoluminescence image of contacted MoS_2 flake (c) Current vs. V_g characteristic of MoS_2/BN device (d) Photoluminescence spectra of 2 different MoS_2/BN devices and MoS_2/SiO_2 devices (e) Raman spectra of MoS_2/BN and MoS_2/SiO_2 devices..41

Figure 3.9 AFM scan of MoS_2/BN devices before and after Ar/H_2 annealing at various temperatures (a) Pre-annealed MoS_2/BN devices (b) After annealing in Ar/H_2 at 300℃ (c-d) After annealing in Ar/H_2 at 450℃...42

Figure 3.10 (a) Multi-probe MoS_2/SiO_2 devices. (b)After transferring thin ~7nm BN on top of MoS_2 and Au electrodes. (c) After Cr/Au (2nm/80nm) top-gate deposition (d) Device schematic (e) Current versus V_g for dual gated MoS_2 devices. (f) Mobility vs carrier density for dual gated devices. 44

Figure 3.11 (a) Z-contrast STEM image of synthesizes $MoSe_2$. Bright spots are Se_2. Red squares highlight area of synthesized $MoSe_2$ with high number of Se defects (b) STEM image of MoS_2. Bright spots are Mo atoms. 46

Figure 4.1 (a) Schematic of MoS_2-FET device (b) Optical image of MoS_2-FET used for our studies (c) Fluorescence image of the same device collected using a conventional fluorescence microscopy setup with a 605-615nm bandpass filter and green light (530–590 nm) excitation...48

Figure 4.2 (a) PL spectra of monolayer MoS_2 at different Vg. Inset: Band Structure of monolayer MoS_2 (b) Photoluminescence image of MoS_2-FET at various V_g. 49

Figure 4.3 Differential reflectivity ($\Delta R/R$) measurement in monolayer MoS_2. Green arrow used to highlights the laser excitation energy (2.33 eV) used to record PL. 50

Figure 4.4 (a) Electrical characterization of monolayer MoS2 FETs. (a) Source drain current I_{sd}vs. gate voltage V_g at applied source drain bias V_{sd}=50 mV. Inset shows the position of the E_F at V_g =-40V and +40V. At +40V free carriers occupy phase space decreasing osciallator strength of excitons forming at the K-point (b) The intensity of photoluminescence vs. V_g for the same device. The excitation wavelength was 2.33 eV, power ~ 1 µW, and the beam spot size ~ 1 µm. (c) PL spectra of a bilayer MoS_2-FET device recorded at gate voltages -50V,- 0V, 50V under 50 µW laser excitation power. Spectra at different V_g are unchanged. The inset shows the band structure of bilayer MoS_2. Along with “A” and “B” transitions, momentum-violating transition “I” across indirect band gap of bilayer MoS_2 is indicated. 52

Figure 4.5 Magnitude of PL modulation (PL_{-50V}/PL_{+50V}) vs $1/\sqrt{\text{Laser Power}}$. 53

Figure 4.6 (a) Photoluminescence spectra of MoS_2 at different Vg. Both neutral (A) and trion (A^-) features are identified. (b) Dependence on gate voltage of the drain–source current (right) and the integrated photoluminescence intensity of the A and A^- features and their total contribution (left). Adopted from reference [48] (c) Photoluminescence color plot of $MoSe_2$ at different Vg. With large electron (hole) doping, negatively (positively) charged excitons dominate the spectrum. (d) Illustration of quasi-particle trion formation with n and p doping. Adopted from reference [49]. 54

Figure 5.1 (a) Absorption spectra of monolayer MoS_2 at two different doping levels. Inset: bandstructure of MoS_2 near its K-point. (b) PL spectra of monolayer MoS_2 at two different doping levels. Inset: time-resolved PL due to A-excitons in MoS_2. (c) PL spectrum of CdSSe QDs. Inset: time-resolved PL of excitons in QDs. 58

Figure 5.2 (a) Device schematic of electrolyte gated QD/MoS_2 hybrid. Optical and photoluminescence images of an electrically contacted QD/MoS_2 device 60

Figure 5.3 (a) Ungated MoS_2/QD device along with its optical (left) and photoluminescence (right) images. PL image was recorded using a band-pass filter (605nm-615nm) only transmitting QD emission. (b) PL spectra and time-resolved PL (Inset) of QD/MoS_2 hybrid (red) and of bare QD film (black). The spectra were recorded from the same device shown in Fig. 3a at positions marked by red and black circles. The schematic on the right illustrates FRET between a QD and MoS_2.. 61

Figure 5.4 PL spectra of a QD/MoS_2 device at different V_g. Inset: QD photoluminescence intensity vs. V_g during a back-and-forth sweep between +2V and -2V..64

Figure 5.5 (a) Schematic of measurement set up for transmission microscopy. (b) Transmittance modulation of MoS_2. The dip at ~1.8eV is likely related to charged exciton absorption. 67

Figure 5.6 (a) Q(α) plot including the data for $0<V_g<0$. (b) Photoluminescence spectra of two different MoS_2-only devices without QDs, and of two different QD/MoS_2 devices. (c) Proposed Fermi level (E_F) positioning of MoS_2 in MoS_2-only and QD/MoS_2 devices. 68

Figure 5.7 (a) Device schematic for MoS_2/spacer/QD device. (b) Raman spectra of MoS_2 before (black) and after (red) SiO_2 spacer deposition. (c) QD quenching factor vs. spacer thickness. Inset: PL spectra of QD and QD/MoS_2 for 15nm spacer device. (d) Photoluminescence spectra for QDs covered by hBN (blue and green curves) and QDs away from hBN (black and red curves). Inset: schematic of a hBN/QD device. 70

Figure 5.8 (a) QD/MoS_2 gated device with QDs in resonance with MoS_2 B-peak (b) QD/graphene device with same QDs highlighting how QD PL is not affected by change in carrier density of 2D material on top 71

Figure 5.9 (a) Green QD/WS_2 gated device showing modulation of green QDs which are in resonance with WS_2B B-peak (b) Same QDs are not modulated by MoS_2..................................72

Figure 6.1 (a) Band gap versus mobility for various materials used in current photovoltaic technologies. Semiconductors with high mobility and bandgap near Shockley-Quessier limit (1.3eV) are desired for more efficient photovoltaic devices. TMDC compare favorably to other materials. Bandgap engineering of TMDCs could further enhance the performance of solar cells based on TMDCs. Figure acquired from reference [18] (b) Schematic for multi-junction semiconductor solar cell designed to absorb larger part of the solar spectrum. Such device structures can potentially be achieved by using TMDCs with graded bandgaps. Figure acquired from reference [90] (c) Schematic of strain engineered MoS_2 device allowing capture of photons of different energies and guidance of concentrated charge carriers towards contacts. Figure acquired from reference [86] Bandgap versus applied electric field for bilayer TMDCs. Figure acquired from reference [87] 76

Figure 6.2 (a) Transmittance of 50nm ITO films prepared through e-beam evaporation. (b) Au/bilayer MoS_2/BN/ITO devices. Optical image highlights damaged ITO at Au/ITO interface. (c) Transmittance of graphene. Figure acquired from reference [94] (d) Proposed device

schematic for applying vertical electrical fields through bilayer MoS_2 using graphene as a top transparent electrode. 79

Figure 6.3 (a) PL spectra of monolayer WS_2 vs. backgate. X_0 denotes the peak due to neutral band edge excitons while X^- denotes due to negatively charged trion peak. (b) PL spectra of ionically gated monolayer WS_2 device. The evolution of the X^- into a new quasi state X^B is evident (c) PL spectra of ionically gated monolayer WS_2 device plotted in log scale to elucidate the evolution of X^B at energies lower than trion peak <1.95eV. (d) Peak position vs. gate voltage (upon electrolyte gating). Peak positions acquired using Gaussian fits. All data taken at room temperature. 81

LIST OF PUBLICATIONS

1. H Conley, NV Lavrik, **D Prasai**, KI Bolotin, Graphene bimetallic-like cantilevers: probing graphene/substrate interactions, ***Nano Lett.***, 11, 4748-4752, (2011).
2. **D Prasai**, JC Tuberquia, RR Harl, GK. Jennings, and KI Bolotin, Graphene: Corrosion-Inhibiting Coating. ***ACS Nano***, 6, 4540-4540, (2012).
3. AKM Newaz, D Markov, **D Prasai**, KI Bolotin, Graphene transistor as a probe for streaming potential, ***Nano Lett.***, 12, 2931-2935, (2012)
4. AKM Newaz, **D Prasai**, JI Ziegler, D Caudel, S Robinson, RF Haglund Jr, KI Bolotin, Electrical control of optical properties of monolayer MoS2. ***Solid State Commun.***, 155, 49-52, (2013)
5. SW Crowder, **D. Prasai**, R Rath, DA Balikov, H Bae, KI Bolotin, H Sung. Three-dimensional graphene foams promote osteogenic differentiation of human mesenchymal stem cells. ***Nanoscale***, 5, 4171-4176, (2013)
6. D Gunther, G LeBlanc, **D Prasai**, JR Zhang, DE Cliffel, KI Bolotin, GK Jennings, Photosystem I on graphene as a highly transparent, photoactive electrode. ***Langmuir***, 9, 4177-4180, (2013)
7. AR Klots, AKM Newaz, Bin Wang, **D Prasai**, H Krzyzanowska, D Caudel, NJ Ghimire, J Yan, BL Ivanov, KA Velizhanin, A Burger, DG Mandrus, NH Tolk, ST Pantelides, KI Bolotin. Probing excitonic states in ultraclean suspended two-dimensional semiconductors by photocurrent spectroscopy. ***Sci. Rep.***, 4, 6608, (2014)
8. J Lin, O Cretu, Wu Zhou, K Suenaga, **D Prasai**, KI Bolotin, NT Cuong, M Otani, S Okada, AR Lupini, JC Idrobo, D Caudel, A Burger, N J Ghimire, J Yan, D G Mandrus, SJ Pennycook, ST Pantelides. Flexible metallic nanowires with self-adaptive contacts to semiconducting transition-metal dichalcogenide monolayers. ***Nat. Nanotechnol.***, 9, 436-442, (2014)
9. **D Prasai,** A Klots, AKM Newaz, JS Niezgoda, NJ Orfield, CA Escobar, A Wynn, A Efimov, GK Jennings, SJ Rosenthal, KI Bolotin, Electrical control of near-field energy transfer between quantum dots and 2D semiconductors ***Nano Lett.***, 15, 4374-4380, (2015)
10. W Wang, A Klots, **D Prasai**, Y Yang, KI Bolotin, J Valentine, Hot Electron-Based Infrared Photodetection Using Bilayer MoS_2 ***Nano Lett.***, DOI**:** 10.1021/acs.nanolett.5b02866 (2015)

CHAPTER 1: INTRODUCTION

1.1 Motivation

The discovery of graphene in 2004, by A.K. Geim and K.S. Novoselov, jumpstarted the field of two-dimensional (2D) material research [1, 2]. Geim and Novoselov isolated graphene, a single 2D atomic layer of graphite, and were able to fabricate field-effect transistors (FETs) out of it. Graphene was shown to have a unique dispersion relation and Dirac particles. Transport measurement on graphene devices showed high conductivity and room-temperature carrier mobilities of up to 15,000 $cm^2V^{-1}s^{-1}$[2] .

Despite graphene's rich electrical properties, the lack of an electrical band gap, a material property essential for modern digital logic transistors, has been its Achilles heel. In modern digital logic transistors, high carrier mobility is desired for fast operation and a high current ON/OFF ratio for effective switching. Fortunately, the research time invested in graphene has established the groundwork to delve into the expanding world of layered 2D layered materials. The recent rise of MoS_2, [3-5] a direct band gap analog of graphene, has made researchers optimistic about possibilities of incorporating 2D materials into modern-day electronics. Monolayer MoS_2 is also an interesting optically active material due its characteristic direct energy gap and the existence of tightly bound (~800meV) band-edge excitons [3, 6].

Two-dimensional materials are unique as they can be considered all "surface" due to the high surface-volume ratio. The interface of 2D materials with the environment can therefore significantly affect material properties and device performance. As an example, early MoS_2-based field effect transistors have shown to have much lower mobility values than what is predicted by theory [7, 8]. The factors limiting mobility in MoS_2 are not fully understood.

Additionally, the effects of interplay between free charge carriers and tightly bound MoS_2-excitons have also not been explored.

In this thesis we explore the effects of the environment on electrical transport and optical properties of monolayer MoS_2. In particular, we investigate the role of the underlying substrate, metallic contacts to MoS_2 and phonons on intrinsic transport properties (e.g. carrier mobility) of MoS_2. We then investigate the interplay between gate-induced charge carriers and excitons in MoS_2 and discover the tunability of MoS_2-optical properties (absorption/photoluminescence). Such strong electron-exciton interaction in MoS_2 also opens up the possibility to study interesting quasi particles like trions and biexcitons in a 2D system. We then thoroughly investigate Förster resonant energy transfer (FRET), a uniquely efficient long-range optical process, between quantum dots and monolayer MoS_2. We discover that modest gate-induced variation in the excitonic absorption of MoS_2 lead to large (~500%) changes in the FRET rate and allows modulation of quantum dot photoluminescence intensity.

1.2 Carbon allotropes

One of the most famous allotropes of carbon is diamond, where each carbon atom forms four C-C bonds (bond length=1.54 Å) in a sp^3 hybridized state (Fig. 1a,b). All four valence electrons in the outer atomic shell are used in the formation of the σ bonds. Since there are no free electrons, diamond is an insulator with a large band gap of 5.47eV.

The second stable atomic arrangement of carbon atoms, graphite, is a sp^2 hybridized state. Each carbon forms three covalent C-C, σ bonds (bond length 1.42 Å) in the x-y plane leaving a perpendicular $2p_z$ orbital (Fig. 1c). The p_z orbital gives rise to a highly delocalized π-orbital. Graphene is a single sheet of sp^2 hybridized carbon atoms that are packed in a honeycomb lattice

(Fig. 1d) that is 3.4 Å thick. Multiple stacks of graphene form graphite. The π-orbital in graphene makes it highly conductive while the C-C bonds gives it it's great mechanical strength. The 0D allotrope of sp^2 hybridized C atoms is fullerenes while the 1D allotrope is carbon nanotubes that can be viewed as a rolled up graphene sheet.

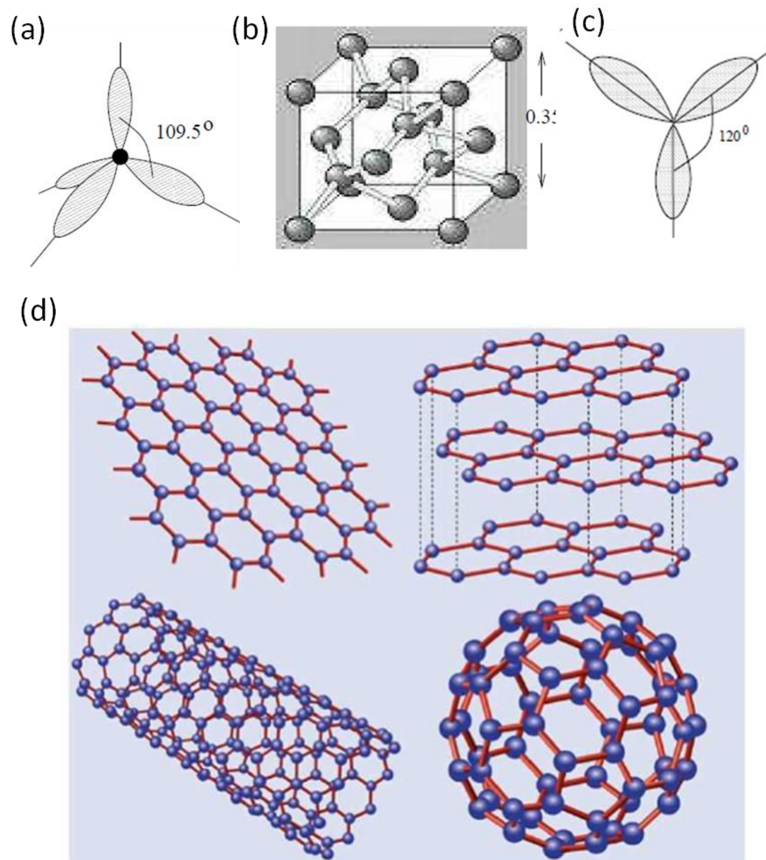

Figure 1.1 *(a) Schematic view of sp^3hybridization. (b) Crystal structure of diamond (2 interpenetrating fcc lattices). (c) sp^2 hybridization. (d) 2D honeycomb structure of graphene. Graphite, a stack of graphene. Carbon nanotubes, a rolled up version of graphene or wrapped up into a 0D buckyball. Figure acquired from reference [9].*

1.3 Graphene band structure and its field effect

Modern-day semiconductor electronic devices are based primarily on digital logic devices. Such logic devices require reading of distinct voltage states which corresponds to either true "1"

or false "0". Current electronic devices consist of a large number of logic gates consisting of several transistors. Such distinct voltage states are currently provided by silicon based metal-oxide-semiconductor FET (MOSFET). Silicon which has a bandgap of 1eV allows for large ON/OFF ratios (between 10^4 to 10^7) required for switching. The bandgap is an intrinsic property that governs the electrical transport and optical characteristics of any material. It plays a critical role in device physics and directs the operation of semiconductor devices such as p-n junctions and transistors.

A FET operates by changing conductivity in the FET channel (Si) by an electric-field effect. Size scaling of such devices allows for more complex integrated circuits and faster operation. Current day processors can contain up to two billions MOSFETs. However, the understanding within the semiconductor-based electronic community is that current MOSFETs are approaching their scaling limit. New materials are therefore needed to replace Si.

Graphene is a semimetal and therefore has no band gap (Fig. 1.2a), [1, 2] Graphene shows a linear dispersion relation near the K and K` points of its Brillioun zone where electrons behave like massless Dirac fermions:

$$E\ (k) = \hbar k v_F,$$

$$where\ v_F = 10^6\ m/s.$$

In a typical graphene-FET (Fig 1.2b), a single graphene crystal is exfoliated on top of 300nm thick insulating SiO_2 on an *n*-type Si substrate that acts as a back gate. This sandwich of graphene-SiO_2-backgate can be viewed as a parallel plate capacitor, which has a capacitance of:

$$C = Q/V_g = \varepsilon_o \varepsilon A/d$$

Here, $Q = en_{2D}A$ is the capacitor charge, V_g is the gate voltage, d = 300nm is thickness of SiO_2 layer, $\varepsilon = 3.7$ (dielectric constant of SiO_2), $\varepsilon_o = 8.85 \times 10^{-12}\ Fm^{-1}$ (vacuum permittivity).

Therefore, the carrier density (n) induced by the filed effect is $n = \alpha V_g$ where $\alpha = \varepsilon_o\varepsilon/ed \sim 10^{10}\ cm^2/V$. So, by varying gate voltage between -100V and 100V, we can induce maximal carrier densities around $\sim 7 \times 10^{12}\ cm^2$. An important parameter in FETs is the carrier mobility (μ). It is defined as $\mu = v/E = \sigma/en$, where v is a carrier drift velocity, E- applied electrical field, σ is conductivity and n is carrier density. Room temperature mobility for exfoliated flakes is reported to be as high as 15,000 cm^2/Vs. Mobility values can reach as high as 40,000 cm^2/Vs by substrate engineering (boron nitride substrates).[2, 10]

In a graphene-FET (Fig.1.2b), by changing n, the current can be switched leading to an ambipolar field effect (Fig 1.2c). Due to the gapless nature of graphene, at any V_g the carrier density is non-zero and the conductivity cannot be turned off. Inducing a band gap in graphene is very difficult and requires either complex fabrication procedures or high voltage.[11, 12] The lack of a bandgap in graphene essentially makes it unusable for logic applications.

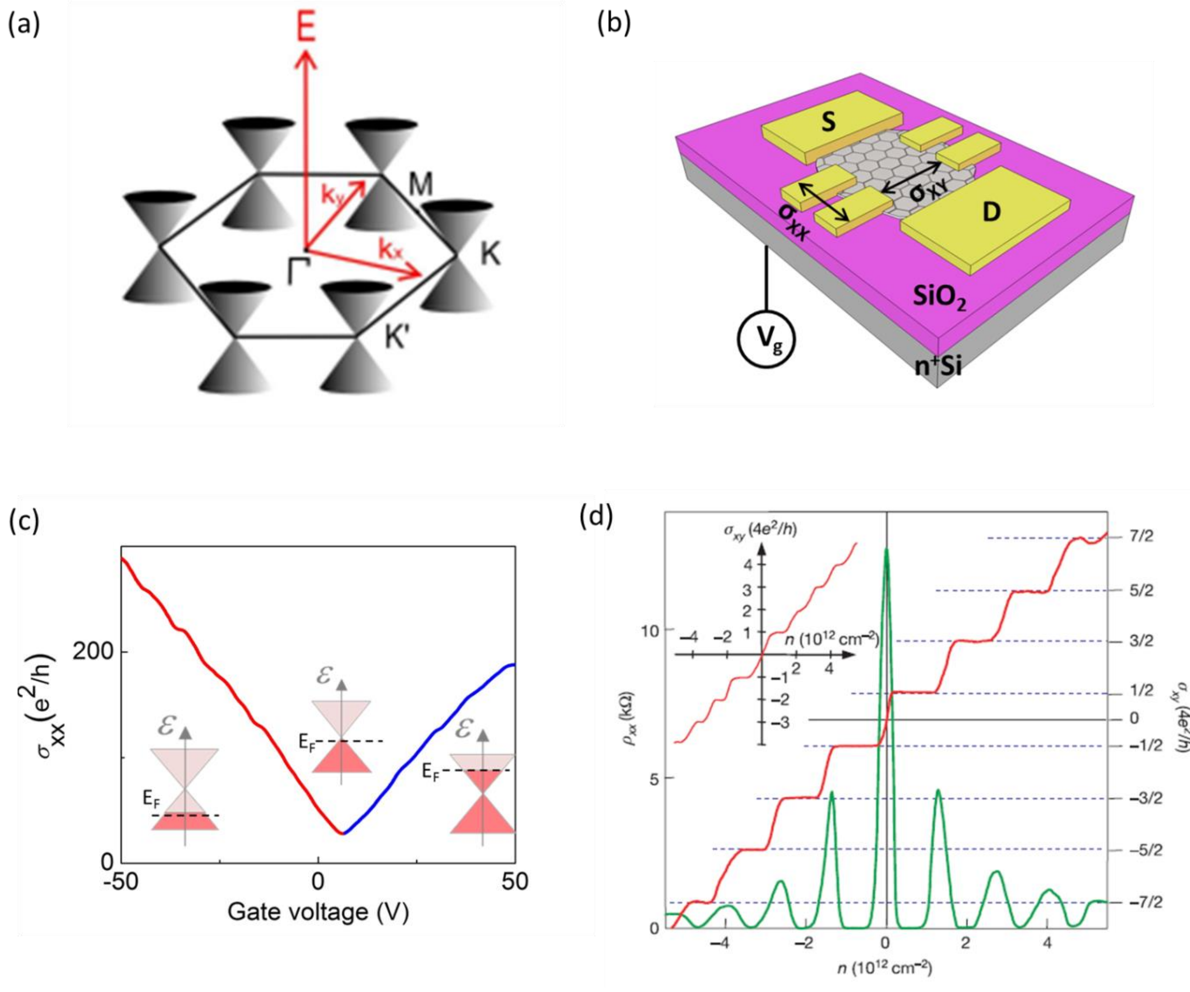

Figure 1.2 *(a) Schematic view of the first Brillouin zone in the reciprocal latticeof graphene (b) Schematic of a graphene-FET (b) Ambipolar field effect in graphene. Cones representing bandstructure of graphene at the K point. Shaded region shows relative position of E_f at different external gate voltage (d) Quantum Hall effect for massless Dirac fermions in graphene. Figure acquired from reference [13]*

Despite its limited use in FET operation, graphene is a nice platform to study correlated electronic systems. Electrons in a 2D system like graphene under strong magnetic fields can interact very strongly, seen in transport measurements of the Hall conductivity as quantum Hall effect and fractional quantum Hall effect under high fields (Fig. 1.2d).

The semiconductor industry initially was very excited about graphene due to the high room temperature mobility (μ) in the material (~15,000 cm^2/Vs for graphene on SiO_2). Even higher mobilities can be achieved by suspending graphene to remove all external sources of electron scattering. In such devices, μ=200,000 cm^2/Vs have been reported at low temperatures [14]. Despite graphene being unsuitable for digital logic based devices it still holds a lot of promise for transparent and flexible electronics. Transparent conductors are key components in electronic products such as touch screen displays and e-paper. They also have uses in solar cell and light-emitting diode applications. For such devices, a material with low sheet resistance and high transmittance is required. Graphene fulfills all such requirements and has the added benefit of being very durable and being able to withstand ~20% tensile strain without any degradation in electrical quality [15]. With the advancement in growth and graphene production we may expect to see ITO (Indium tin oxide), the most commonly used transparent conducting material, slowly replaced by graphene from future devices.

1.4 Molybedum Disuflide (MoS_2)

The rise of graphene has provided researchers in the field with tools and skills to pursue the study of other layered 2D materials. One such material is MoS_2 which is the main subject of research in this dissertation. MoS_2 comes from the family of layered transition-metal dichalcogenide (MX_2, M = Mo, W; X = S, Se, Te). The atomic strcutre of MoS_2 is a hexagonal arrangement of Mo and S atoms layered on top of each other to form a trigonal prismatic arrangement (Fig. 1.3a,b). The spacing between layers in a crystal is ~6.5 Å. Bulk MoS_2 is an indirect-gap semiconductor with a band gap of 1.29 eV. However, monolayer MoS_2 is a direct band-gap semiconductor with a band gap of ~1.9eV also making it optically active in the visible

range (Fig.1.3c) [3, 4]. The band gap at the K-point is related to the d orbitals of the sandwiched Mo atoms in the unit cell (S-Mo-S) which remains unchanged with layer thickness. The indirect band gap at the Γ point is related to the p_z oribitals of the S atoms and decreases with an increase in layer thickness hence even making bilayer-MoS_2 an indirect band gap material [3]. Similar to graphene, the bandgap is also located at the K (K`)-points. The band structure at the K-point in MoS_2 is further modified due to strong spin-orbit interactions caused by the high atomic number of the transition metal. This causes spin-splitting of the valence band at the K-point by ~150meV (Fig. 1.3d). This splitting gives rise to the “A” and “B” excitonic photoluminescence/absorption features discussed later.

Unlike graphene, the dispersion relation in MoS_2 is given by:

$$E_F = \hbar^2 \pi n / 2 m_e e^2,$$

here m_e is the electron band mass given by $m_e = 0.35 m_o$

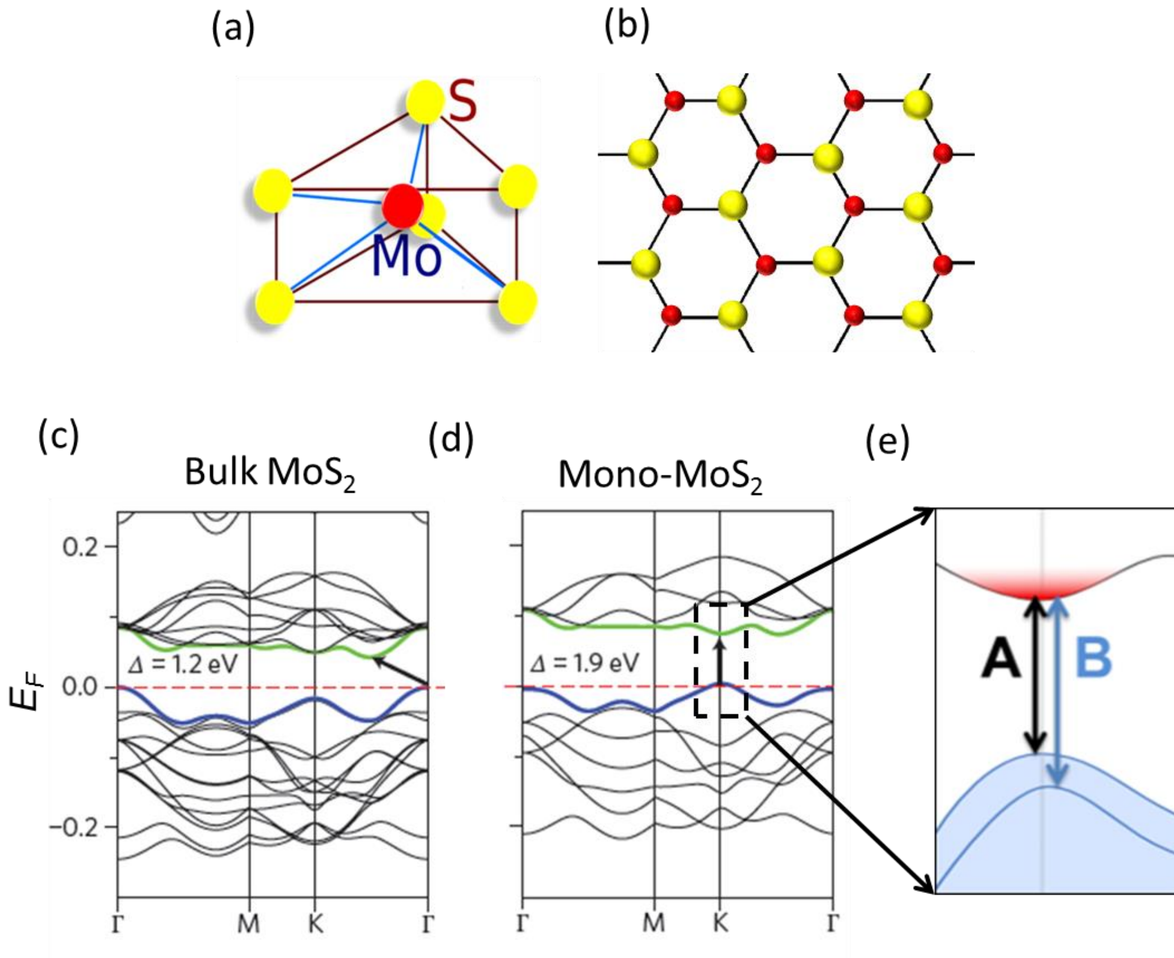

Figure 1.3 *(a) Lattice structure of* MoS_2 *(b) A top view of the monolayer* MoS_2 *lattice, (c) Band Structure of bulk and monolayer-*MoS_2 *as calculated from density functional theory. Arrows indicate fundamental bandgap (Indirect for bulk, direct for monolayer-*MoS_2*). Figure acquired from reference [16] (d) Bandstructure schematics of* MoS_2 *near K-point illustrating the origin of band-edge A- and B-excitons.*

The existence of a band gap in MoS_2 significantly alters its field effect (Fig. 1.4). When the Fermi level (E_F) lies in the band gap, there are no conduction electrons and there conductivity is small. When E_F is shifted into the conduction band with an external gate voltage V_g, MoS_2 starts conducting as shown in Fig. 1.4. MoS_2-FETs operate in the electron-doping regime and can be switched off, unlike their graphene counterparts.

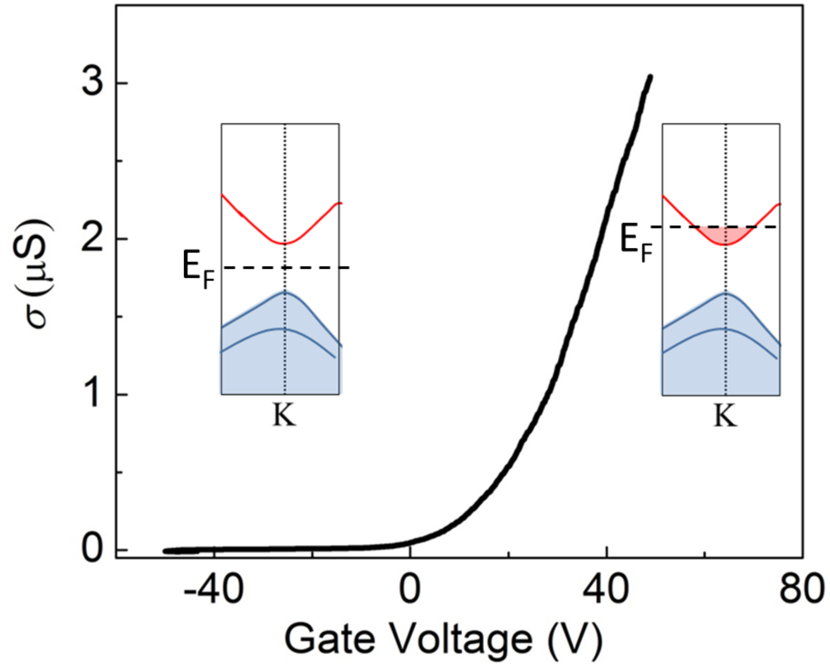

Figure 1.4 *Field effect in MoS_2 with n-type channel with large ~10^6 ON/OFF ratios. Inset shows the relative position of E_F at different Vg at the K-point.*

The major setback in MoS_2-FETs is their low room temperature mobility. Early two-probe measurements of MoS_2 showed really low mobility $\sim 3cm^2/Vs$ in the material compared to theoretically predicted values (Fig. 1.5) [7] The low values reported for MoS_2-FETs motivated us to carefully measure mobility in MoS_2 and to identify the major factors limiting it, which is one of the main goals of this thesis.

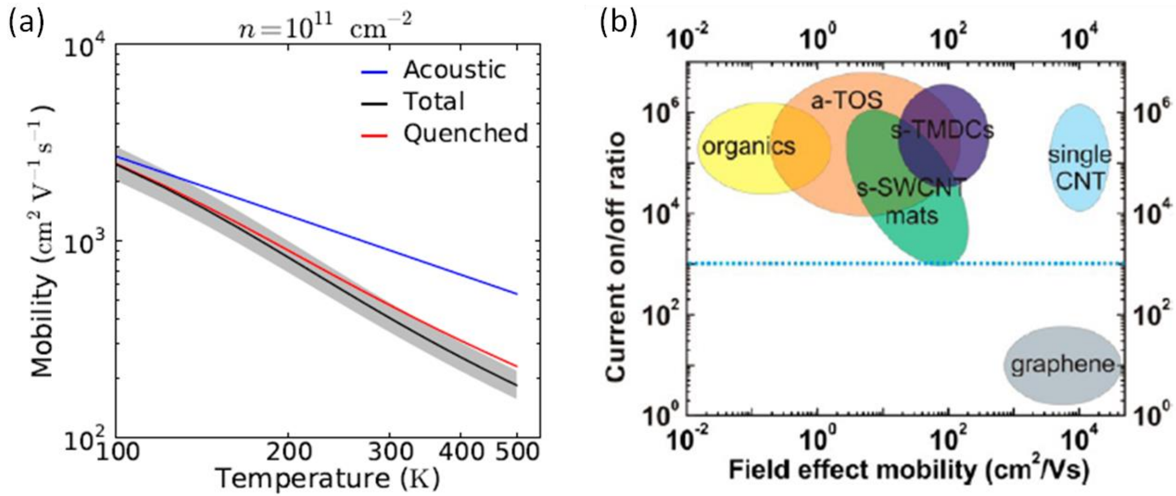

Figure 1.5 (a) *Calculated mobility as a function of temperature for monolayer MoS_2. Black curve represents mobility vs temperature when scattering off of both acoustic and optical phonons is included. Red curve represents mobility when optical phonons are quenched. Blue curve represents mobility when only acoustic phonons are present. Figure acquired from reference [17](b) Comparing mobility and ON/OFF ratio of TMDCs with other materials researched for unconventional electronics. Figure acquired from reference [18].*

1.5 Optics of MoS_2

As discussed in the previous section, monolayer MoS_2 is a direct band gap semiconductor (Fig. 1.3). When direct band gap semiconductors are excited by photons ($\hbar\omega > E_g$), an electron can be excited into the conduction band leaving a hole in a valence band. The recombination of this electron-hole pair can lead to light emission from the material with energy corresponding to E_g. However, in 2D systems such as MoS_2, low dielectric screening, 2D-confinement and high effective carrier mass lead to strong electron-electron interactions and emergence of tightly bound excitons. Excitons in MoS_2 are purely 2D in nature, and their binding energies can be

determined by solving a 2D Hydrogen-like Schrödinger equation. Confinement effects in 2D-systems lead to energy levels,[19]

$$E_N = -\frac{R_x}{(n-\frac{1}{2})^2}, \textit{ for } n = 1,2,3,4\ldots$$

Here, n (integer) is the principle quantum number.

The effective Bohr's radius and Rydberg are:

$$a_B = \frac{\hbar^2 \varepsilon}{\mu e^2},\ R_x = \frac{e^2}{2\varepsilon a_B}.$$

We see that the ground-state exciton has a binding energy of $4R_x$. Using $\varepsilon = 3.4$ and the effective Bohr radius a_B ~1nm, we estimate a ground-state binding energy of ~800meV. This high binding exciton energy in monolayer MoS_2 means that the excitons are stable even at room temperatures (k_bT=25meV). We therefore expect optical absorption and emission spectra of MoS_2 to be strongly modified by excitonic effects.

1.6 Photoluminescence and absorption of MoS_2

Optical transitions in MoS_2 can be probed using absorption or photoluminescence (PL) spectroscopies. The PL in bilayer and bulk MoS_2 is significantly lower compared to monolayer samples as there is a crossover from indirect to direct band gap material (Fig. 1.6b).[3, 4] This crossover from direct-indirect band gap produces large disparity in the quantum efficiency between bilayer and monolayer MoS_2 (Fig. 1.6b).

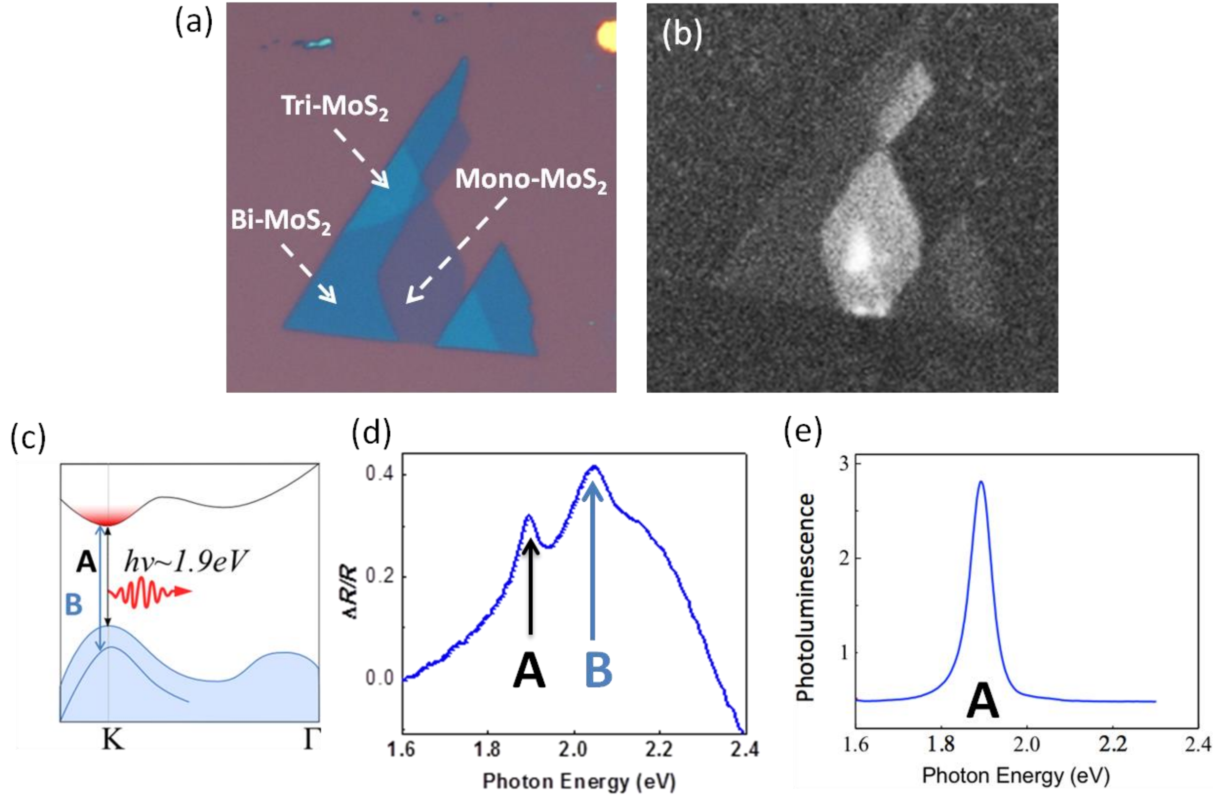

Figure 1.6 *(a) Optical microscopy image of monolayer* MoS_2 *on* SiO_2/Si*. Scale bar is 10µm (b) Corresponding photoluminescence image. (c) Bandstructure of monolayer* MoS_2 *around the K-point. Valence band is split by ~200meV due to strong orbit interaction (d) Absorption spectra of* MoS_2 *dominated by A, B-excitonic peaks (e) Photoluminescence spectra of* MoS_2 *dominated by A peak, the ground state of* MoS_2*.*

In monolayer MoS_2, the dominant optical transitions “A”(~1.9eV) and “B” (~2.1eV) correspond to excitonic transitions between the valence band split by spin-orbit interaction and the conductance band (Fig. 1.6c) [3, 4, 20]. These features can be seen in the absorption spectra in Fig. 1.6d. The photoluminescence spectrum (Fig. 1.6e) matches the lower absorption peak “A” (1.9eV) attributing the PL in monolayers to recombination across the direct band gap.

OUTLINE OF THE DOCUMENT

As stated in the motivation section, the primary goal of this thesis is to investigate the environmental factors that govern electrical and optical properties of 2D materials. This thesis has been organized to address this goal through a series of electrochemical, transport and opto-electronic measurements in 2D material: graphene and MoS_2.

In chapter 2, we examine the use of graphene as an atomically thin protective coating of an underlying metallic substrate. We investigate how films of graphene can be used to decouple underlying metallic substrates from the environment to passivate corrosion. In testing this, we employed electrochemical impedance spectroscopy (EIS), Tafel and X-ray photoelectron spectroscopy (XPS) analysis to quantify protection against corrosion and to identify its mechanism. These results are published in *ACS Nano* [21].

In chapter 3, we investigate carrier scattering mechanisms in monolayer MoS_2 through transport measurements in field effect transistors. We fabricate multi probe MoS_2 devices to study temperature dependent transport and extract carrier density and Hall-mobility at temperature range 300K-2K. We identify mobility-limiting factors in the material and attribute it to phonon scattering at temperature >100K and defect scattering at low temperature (<100K). We then demonstrate the detrimental role of contacts in such devices and a carrier density induced metal-insulator transition in MoS_2. We present techniques to engineer the MoS_2 substrate with the hope of increasing mobility and demonstrate a dual-gated device geometry that increases carrier mobility in MoS_2.

In chapter 4, we investigate electrical modulation of optical properties of monolayer MoS_2. We explore the photoluminescence of single layer MoS_2 while electrically gating the material. We demonstrate that we can modulate PL in MoS_2 by ~100 times and absorption by 50%. We attribute this modulation to phase space filling effect. We also present an alternate explanation of the PL field effect due to trion (charged exctitons) formation in the material. This result is published in *Solid State Communication* [20].

In chapter 5, we investigate optical properties of hybrid MoS_2/fluorescent quantum dot system. We study Förster resonant energy transfer (FRET) between highly fluorescent CdSSe graded-alloy QDs and monolayer MoS_2 and demonstrate electrical tunability of that FRET. We demonstrate ~75% tunability of QD photoluminescence intensity in ionically gated hybrid MoS_2/quantum dots (QDs) FETs via FRET modulation. This result is published in *Nano Letters* [22].

In chapter 6, we highlight the future research prospects for TMDC materials. We discuss some ongoing projects where we investigate new approaches towards tailoring the optical properties of TMDCs. We first explore the effects of vertical electric fields on the bandgap and hence the optical properties of TMDCs. We also examine the electron-exciton interaction in highly doped ($>10^{13}cm^{-2}$) TMDCs.

In the Appendix, we detail fabrication (exfoliation, growth, transfer) and characterization techniques (Raman spectroscopy) used to make high-quality graphene and MoS_2 devices. Details

on operating closed cycle He-cryostat are also included in the Appendix. Finally, we detail techniques developed to make hybrid QD/MoS_2 devices.

CHAPTER 2: GRAPHENE AS AN ANTICORROSIVE COATING

In this chapter we discuss our results published in ACS Nano, "*Graphene: Corrosion-Inhibiting Coating"*[21]. We investigate how films of graphene can be used to decouple underlying metallic substrates from the environment to passivate corrosion. In testing this, we employed cyclic voltammetry, electrochemical impedance spectroscopy (EIS), Tafel and X-ray photoelectron spectroscopies (XPS) analysis to quantify protection against corrosion and its mechanism.

2.1 Introduction

Metal corrosion costs the US industries more than $200 billion dollars annually. Corrosion can lead to serious device degradation. Not only can it cause electronic parts to malfunction, it can also seriously affect the strength and structure in large scale devices. Corrosion can be inhibited or controlled by introducing a stable protective layer between a metal and a corrosive environment. Current research on protective coatings is primarily focused on using inert metals, conductive polymers and even thiol-based monolayers [23, 24]. However, these protective coatings have their limitations. Thiolated SAMs can only be assembled on coinage metals (gold and copper) and do not withstand high temperature (~100℃). Polymeric coatings, although very effective, are thick and can alter the physical properties of the underlying material.

2.2 Graphene: thinnest corrosion inhibiting coating

Graphene possesses a unique combination of properties that are ideal for corrosion-inhibiting coating in applications such as microelectronic components and implantable devices. Graphene is chemically inert, stable in ambient atmosphere up to 400℃. Both single-layer and

multilayer films are exceptionally transparent (>90% transmittance for 4-layered films),[25] which means the films do not perturb the optical properties of the underlying metal. Several studies have demonstrated that graphene can effectively decouple the surface under it from the environment. First, Bunch *et al*. have shown the single graphene films are impermeable to gas molecules. Second, Chen et al. have demonstrated that graphene can inhibit oxidation of the underlying copper metal [26, 27]. For this study we investigated the corrosion-protection properties of graphene coatings on two prototypical metals – nickel and copper. These metals are chosen as they are technologically relevant, readily corrode in aqueous environments, and because graphene films can either be grown or mechanically transferred onto them. We fabricated seven different kinds of samples to study the effect of graphene coatings on corrosion. First, to obtain baseline corrosion rates, we studied bare copper samples (Cu) and bare nickel samples (Ni). Second, we obtained samples with graphene grown on either copper (Gr/Cu) or nickel (Gr/Ni). Finally, we studied devices where CVD grown graphene on copper was mechanically transferred onto a surface of a different metal – initially pristine nickel. We use electrochemical techniques such as Tafel analysis [15] to measure corrosion rates and electrochemical impedance spectroscopy (EIS) to elucidate the pathways of corrosion reactions [28].

2.3 Electrochemical measurement setup

All electrochemical measurements were performed in a polytetrafluoroethylene (PTFE) three-electrode cell. A platinum wire was used as a counter electrode, an Ag/AgCl (Gamry Instruments Part No. 930-29) was used as a reference electrode, and the sample of interest was used as the working electrode. The Cu and Gr/Cu foils were laterally mounted in the cell exposing a sample area of 0.4 cm^2 (Fig. 2.1a Inset). The sample foils are typically 1 × 1cm

squares. They are clasped onto a 0.4 cm^2 opening on the PTFE cell that houses the electrolyte. An O-ring is used to make a seal between the electrolyte and the outside space. Copper tape is attached to the sample foil to make electrical contact. Once the sample is mounted onto the electrode cell, it is filled with 0.1 M $NaSO_4$ electrolyte. A Pt counter electrode and Ag/AgCl reference electrode are immersed into the electrolyte. Schematic of a PTFE sample holder is shown in Fig. 2.1.

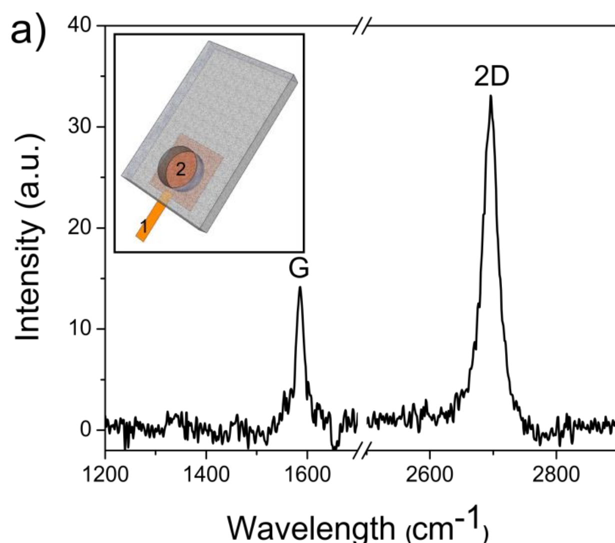

Figure 2.1 (a) *Gr/Cu sample prepared via chemical vapor deposition, and its Raman spectrum exhibiting characteristic G and 2D peaks. Inset representing schematic of foils mounted onto PTFE 3-electrode cell where copper tape(1) is attached to the sample and 0.4*cm^2 *of active area (2) is exposed to the* $NaSO_4$ *electrolyte.*

2.4 Cyclic Voltammetry (CV) of Gr/Cu samples

Our first goal is to elucidate the impact of using graphene as a protective layer on the chemical reactions involved in a corrosion process via cyclic voltammetry. In the case of bare Cu samples, we expect the corrosion process to be comprised of anodic oxidation that creates

soluble Cu^{2+} ions and cathodic reduction reactions that consume the electrons released from the anodic reaction. [29]

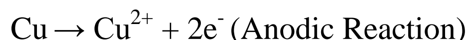

$Cu \rightarrow Cu^{2+} + 2e^-$ (Anodic Reaction)

$O_2 + 2H_2O + 4e^- \rightarrow 4OH^-$ (Cathodic Reduction of O_2) [23]

These two reactions complement each other so that impeding one of them slows the overall corrosion process.

For bare Cu devices, CV measurements provide signatures compatible with these reactions. First, Fig. 2.2a shows that in the positive sweep, bare Cu exhibits a cathodic current that decreases as the potential is made less negative, followed by an anodic peak at -150 mV (*vs.* Ag/AgCl) that we attribute to the formation of adsorbed species on the copper surface. This adsorbed species are then subsequently dissolved as shown by quartz crystal microbalance (QCM) and a rotating ring-disk electrode (RRDE) experiments. In the negative sweep, the CV shows additional electrodissolution of copper (200 to 80 mV) that is influenced by the high concentration of H^+ ions near the surface characteristic in Na_2SO_4 media. The CV also shows three cathodic peaks at 0, -250, and -550 mV that we attributed to the electroredution of copper ions, the reduction of Cu^{+2} to Cu^{+1} species, and the reduction of Cu^{+1} to metallic Cu. To confirm the relation of these peaks to the cathodic reduction of oxygen, we collected the CVs under low oxygen concentration conditions (which was achieved by bubbling N_2 gas through the electrolyte for 10 min) and observed their significant suppression.

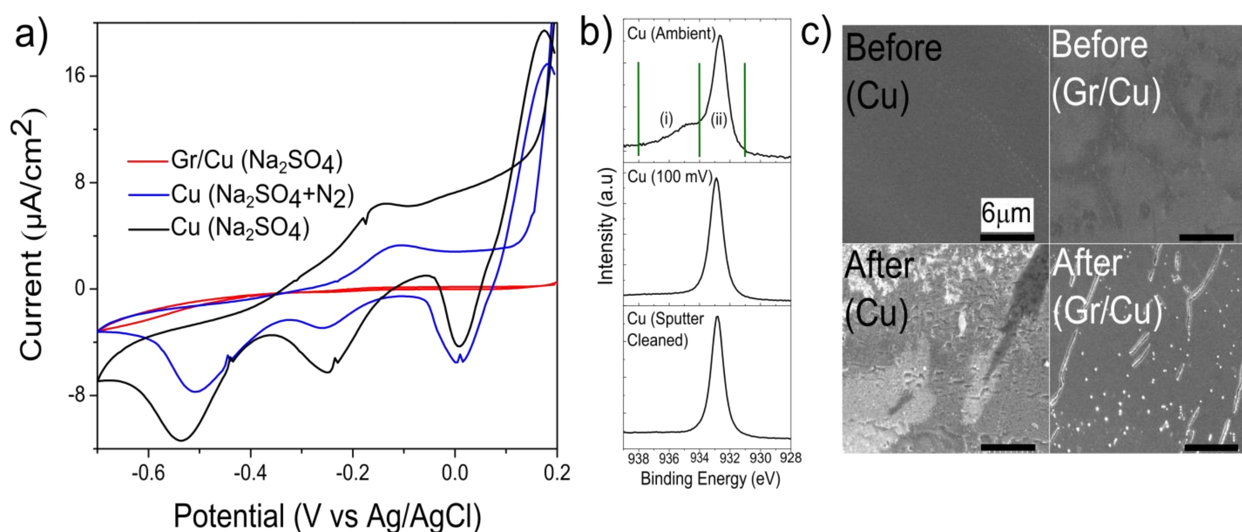

Figure 2.2 *(a) Cyclic Voltammetry measurements (electrolyte is 0.1M Na_2SO_4) in the potential window -700 to 200 mV for bare Cu and Gr/Cu samples. Blue line corresponds to the measurement with nitrogen bubbled through the solution. (b) XPS core level spectrum of Cu (Ambient), Cu (100mV) and Cu(Sputter Cleaned), region (i) displaying shoulder due to CuO, region (ii) peaks due to Cu_2O/Metallic Cu (c) SEM images of Cu and Gr/Cu sample before and after CV scan.*

In contrast, the Gr/Cu samples do not feature any peaks at negative potentials and exhibit dramatically lower current at positive potentials (red curve in Fig. 2a). This provides the first indication that a graphene monolayer exhibits a much lower affinity towards oxygen reduction and forms a barrier between the solution and the copper surface and provides the first evidence that graphene indeed provides corrosion protection.

Three techniques indicate there is little to no oxide layer formation in the bare copper and graphene-protected copper. First, the CVs do not exhibit anodization maxima associated with the formation of a stable oxide layer [29]. Second, Pourbaix diagrams indicate that upon application of positive potentials to the copper electrode in a $NaSO_4$(aq) electrolyte (pH ~7), soluble Cu^{2+} ions are produced rather than a stable CuO layer. Finally, the XPS analysis suggests only trace

amounts of oxide on the copper surface. Fig. 2b shows results from XPS characterization of i) a Cu sample that has been kept in the ambient atmosphere for over a week, ii) a Cu sample that have been taken to +100mV potential in Na_2SO_4 iii) a sputter-cleaned Cu surface which is free of all oxides (Fig. 2.2b). The XPS core-level Cu2p spectrum of sputter-cleaned Cu exhibits a very sharp peak that indicates the lack of copper oxides. In contrast, the copper peak (932 eV) is broadened both in the sample that was kept in the ambient atmosphere and in the samples that was kept at +100mV in the electrolyte. This broadening is likely caused by the Cu_2O peak (due to the formation of native copper oxide) that is very similar in peak position and FWHM to that of clean Cu metal. However, since the broadening is smaller for the electrochemically-processed sample compared to the sample kept at ambient conditions, we once again conclude that the oxide layer are not formed electrochemically.

SEM images provide additional information about the nature of corrosion in Gr/Cu devices (Fig. 2.2c). While the entire surface of the bare Cu sample is damaged after exposure to positive potentials (200 mV from the open circuit potential (OCP)) in the electrolytes, in Gr/Cu samples the surface degrades at isolated areas, while leaving most of the sample surface undamaged (Fig. 2c). As graphene does not corrode in the potential window used in our experiment, we expect that these changes occur at regions of the copper surface that is not covered by graphene, *i.e.* at cracks in the graphene film. This graphene protection mechanism is later verified using electrochemical impedance spectroscopy.

2.5 Tafel and corrosion rate calculation

An electrochemical reaction under kinetic control obeys the Butler-Volmer equation, which relates the exponential dependence of current to the deviation of voltage from the open circuit potential (OCP) value [30]. The OCP is where the rates of the anodic and cathodic processes are balanced. The Tafel equation describes the behavior of an isolated reaction.

$$I = I_O e^{(2.3\frac{E-E_O}{\beta})}$$

Where, I is the current resulting from the reaction, I_o is reaction dependent constant called the exchange current, E is the electrode potential, E_o is the equilibrium potential (constant for a given reaction), β is the reaction Tafel constant

In the case of a corrosion system, we have two differing reactions: anodic and cathodic. Corrosion occurs at a rate determined by equilibrium between opposing electrochemical reactions. The anodic reaction releases electrons into the metal while the cathodic reaction reduces O_2 and removes electrons from the metal. In the case of Cu we have the following reactions:

- $Cu \rightarrow Cu^{2+} + 2e^-$ (Anodic Reaction)
- $O_2 + 2H_2O + 4e^- \rightarrow 4OH^-$ (Cathodic Reduction of O_2)

The Butler-Volmer equation then takes the form:

$$I = I_A + I_C = I_{Corr}\ (e^{(2.3\frac{E-E_{OC}}{\beta_A})} - e^{(2.3\frac{E-E_{OC}}{\beta_C})})$$

Where, I_{Corr} = the corrosion current in amps, E is the electrode potential, E_{OC} is the open circuit potential in volts, β_A is the anodic Beta Tafel constant, β_C is the cathodic Betal Tafel constant.

Potentiostatically measuring the dependence and plotting the logarithm of the current density (i) vs. the electrode potential (V), makes it possible to extract the reaction kinetic parameters, such as the corrosion rate (CR). The OCPs for Cu samples were found to be around -100 mV while for Gr/Cu it was ~-75mV. The cathodic/anodic branches were obtained by sweeping the voltage -150 mV/150 mV from the OCP using scan rates of 0.005mV/s. We then obtain the linear fit using a minimum square error to the Butler-Volmer equation excluding the part of the curve at large overpotentials (over ± 200 mV) and obtain I_{corr} from the point of intersection (Fig. 2.1). Finally, the corrosion rate is given by:

$$CR = \frac{I_{Corr} \times K \times EW}{\rho A}$$

Here, the corrosion rate constant K=1.288×10^5 milli-inches/amp-cm-year. The equivalent weight EW=31.7 g for Cu (29 g for Ni), the material density ρ = 8.94 g/cm^3 for Cu (8.90 g/cm^3 for Ni), and the sample area A= 0.4 cm^2.

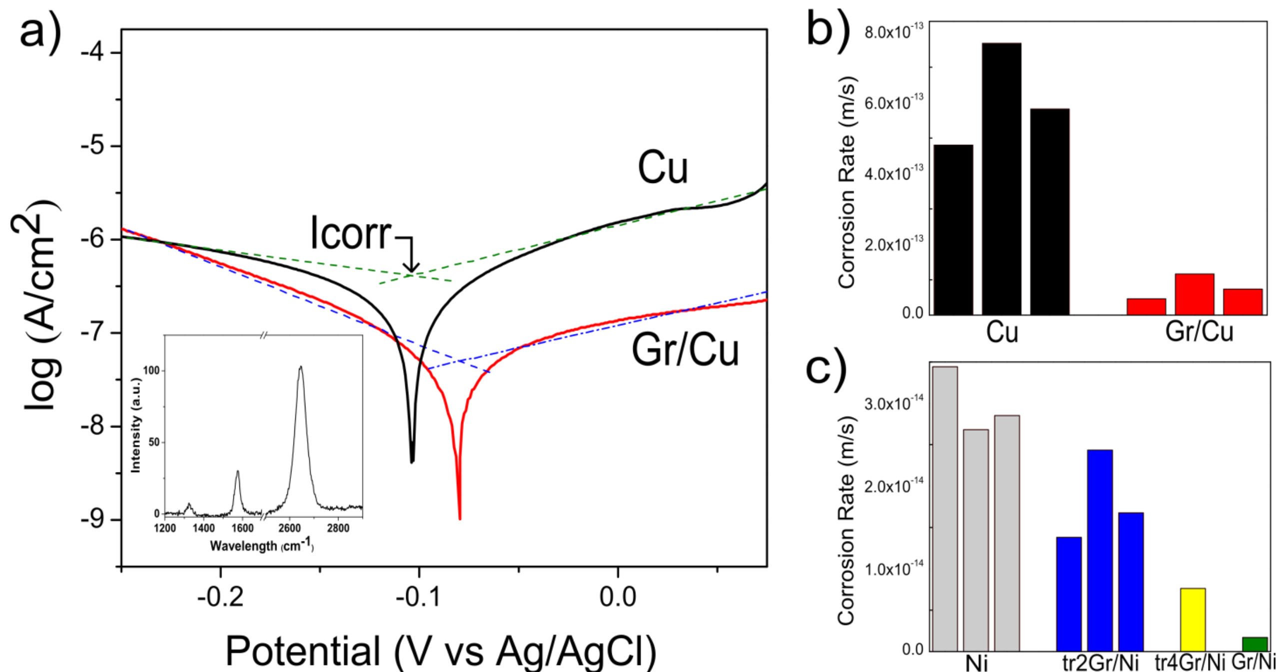

Figure 2.3 *(a) Tafel plots of Cu and Gr/Cu samples. Best fits are represented by dotted lines. Inset: Raman spectrum of the Gr/Cu sample after completing Tafel analysis displays small defect-related "D" peaks. (b) Corrosion rates of Cu and Gr/Cu samples extracted from Tafel plots. (c) Corrosion rate of Ni and Graphene transferred onto Ni substrate.*

Interestingly, Raman spectra taken on graphene samples after electrochemical measurements indicate near-pristine and only lightly damaged graphene. For samples taken to positive potentials, we find that graphene is still intact, while a small defect-related D-peak at ~1350 cm^{-1} appears in some of the samples (Fig. 2.3a, Inset).[i] This change in the Raman spectra suggests graphene does not exhibit appreciable corrosion at the potentials employed in the experiment.

For bare metal samples we obtained the rates of $5.76 \times 10^{-13} \pm 1.9 \times 10^{-13}$ m/s for Cu, and $2.99 \times 10^{-14} \pm 4.0 \times 10^{-15}$ m/s for Ni. Graphene grown via CVD was found to significantly slow down corrosion. For Gr/Cu samples the corrosion rate was $7.85 \times 10^{-14} \pm 3.5 \times 10^{-14}$ m/s, a reduction of ~7 times compared to the bare sample, and for Gr/Ni – 1.71×10^{-15} m/s, a reduction of ~20 times was observed. We have similarly extracted the corrosion rates for samples where the graphene films grown on copper were mechanically transferred onto a target nickel substrate. We have found that a single layer graphene transferred onto nickel does not reduce the corrosion rate of nickel significantly. This is likely a result of tears and rips in the graphene film that may result during its transfer onto the Ni substrate. However, for the case where two or four layers of graphene are transferred onto nickel sequentially, the corrosion rate decreased to 1.83×10^{-14} m/s and to 7.62×10^{-15} m/s respectively. The latter value represents a four-fold reduction of the corrosion rate for bare nickel. All calculated corrosion rates are given in table 2.1.

Table: 2.1

Bare Samples	Corrosion Rate (m/s)	CVD Grown Samples	Corrosion Rate (m/s)	Graphene Transfer Samples	Corrosion Rate (m/s)
Cu	5.76E-13	Gr/Cu	7.85E-14	2Gr/Ni	1.83E-14
Ni	2.99E-13	Gr/Ni	1.71E-15	4Gr/NI	7.62E-15

2.6 Electrochemical Impedance Spectroscopy (EIS) and modeling corrosion pathways

EIS is a very useful tool to elucidate the mechanism of corrosion protection by graphene. In EIS, a small sinusoidal perturbation is applied to the sample under examination and the impedance modulus */Z/* is recorded as a function of frequency *ω*. Fig. 2.4a shows a Bode magnitude plot (*log /Z/ vs. log ω*) for Gr/SiO_2 (blue squares), Gr/Cu (red), and Cu (black) samples. The observed behaviors can be understood by fitting the data to simple equivalent circuit models shown in Figure 2.4b, c.

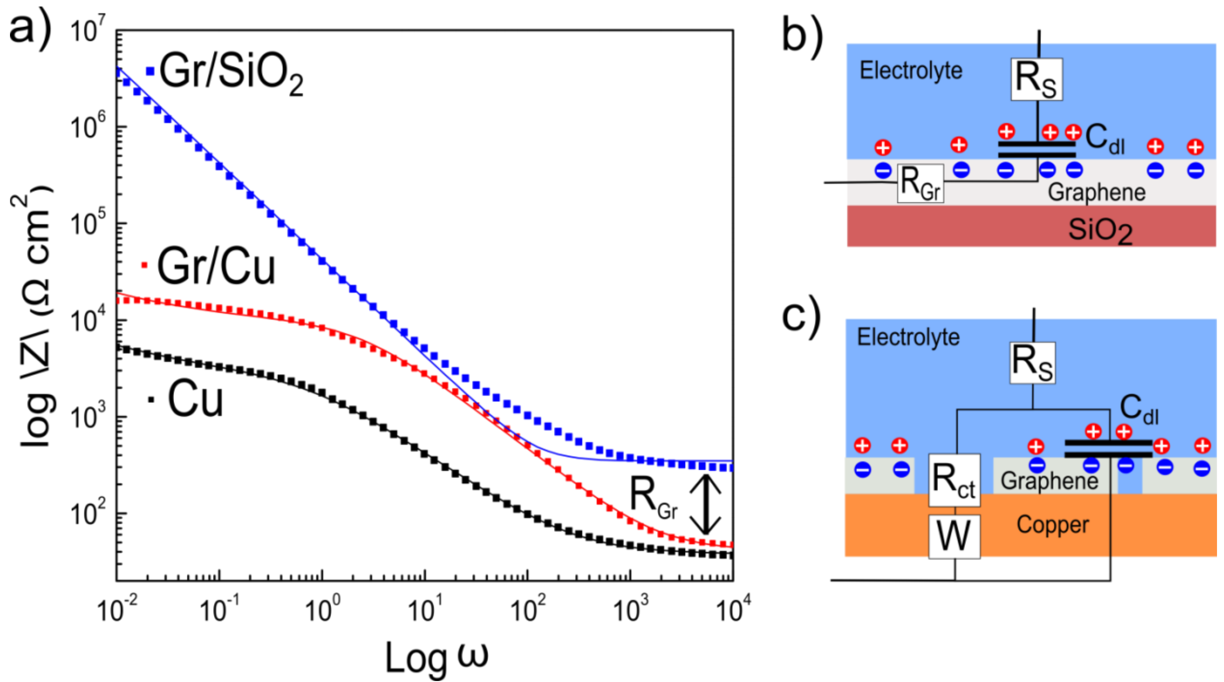

Figure 2.4 *(a) Bode Magnitude plots of Gr/SiO_2, Cu and Gr/Cu samples (solid symbols). Best fits to the equivalent circuit models are solid lines. (b) Equivalent circuit model used in modeling Gr/SiO_2 devices. (c) Equivalent circuit model for Cu and Gr/Cu devices.*

Here we look at the impedance behavior of bare Cu and Gr/SiO_2 as the two extremes of a spectrum. A pure metal for the first and a perfectly protected surface for the later. Understanding the behavior of the two should give us an understanding of Gr/Cu. From the Bode plots we can see that the Gr/Cu surface exhibits an intermediate behavior consistent with the behavior of a graphene-protected metal with minor defects. At high frequencies, the surface exhibits conductivity similar to that of conductive metal. At intermediate frequencies, the surface favors the collection of charges in a similar way as graphene surface does it since its capacitive behavior resembles to that of Gr/SiO_2. And at low frequencies, the surface exhibits a charge transfer behavior indicative of copper degradation. The increased value of R_{CT} at low frequencies in comparison with the corresponding R_{CT}^0 for Cu samples indicates that only the fraction of the

copper that is not covered by graphene is able to participate in the process of corrosion. Our data indicate that corrosion occurs in the cracks of graphene, but the efficiency of the corrosion inhibition may be greatly enhanced by developing protocols to grow highly uniform and large-grain graphene and by performing high fidelity mechanical transfer of graphene onto various metallic surfaces. Values extracted from the EIS data are shown in table 2.2:

Table 2.2:

	C (F/cm2)	R_{ct} (ohm*cm2)	R_{sol} (ohms*cm2)
Cu	4.59E-05	2.95E+03	4.51E+01
Gr/Cu	9.38E-06	1.01E+04	3.75E+01
Gr/SiO2	3.78E-06	N/a	4.39E+02

We can also estimate the fractional area of the uncoated regions via A ~ $R_{CT}^{0}/ R_{CT,}$ which gives us a value A~0.29, which is much larger than the estimations from optical microscopy images (A<0.05). We propose that corrosion is initiated at the defects of the graphene film, followed by electrolyte permeation under the graphene surfaces, leading to a larger apparent corroded area.

2.7 Conclusion and Future Work

In this research project, we were able to demonstrate that graphene layers can serve as a corrosion inhibiting coatings. The efficiency of corrosion inhibition can be greatly enhanced by developing protocols to grow highly uniform and large-grain graphene and by performing high fidelity mechanical transfer of graphene onto various metallic surfaces. More viable solution for depositing thin films of graphene on any arbitrary substrates is needed. For this purpose

graphene oxide (GO) dispersed in solution worth exploring since it can be directly spun coated or even printed using a conventional inkjet printer onto any arbitrary substrate. The GO can then be reduced using a green approach using aluminum powder or endophytic microorganisms present in the carrot root which act as reducing agents.[31, 32] This method allows for the deposition of large area sheets on top of substrates needing passivation without going through the process of polymer assisted transfer methods.

CHAPTER 3: IMPROVING CARRIER MOBILITY AND IDENTIFYING SCATTERING MECHANISMS IN MoS_2

3.1 Introduction

The understanding within the semiconductor-based electronic community is that current MOSFETs are approaching their scaling limit and new materials are required to replace Si. High mobility and atomic thickness of 2D materials make them good alternatives to Si. Since the lack of a sizeable bandgap, a key requirement for transistor operation, rendered graphene ineffective, single layer MoS_2 with its thermal and chemical stability and intrinsic bandgap (1.8eV) started to emerge as a possible alternative for transistor devices [4]. However, early reported mobility values ($\sim 3cm^2/Vs$) of MoS_2 are lower even compared to mobility of Si (<1000 cm^2/Vs).

In this chapter, we fabricate high quality MoS_2-FETs to investigate mobility limiting factors in MoS_2 and explore approaches to mitigate scattering. Mobility limiting factors can be intrinsic (defects in the crystal) or extrinsic (substrate related scattering and metal contact effects). Our primary focus is to investigate the role of extrinsic scattering mechanisms in MoS_2 devices. We study the role of contact resistance (arising from metal-semiconductor interface), electron-phonon interactions and substrate impurities (Coulomb scattering) on electron mobility. We then investigate approaches to increase mobility in MoS_2 via substrate and dielectric engineering.

3.2 Field Effect and Hall mobility in MoS_2

We fabricated two-probe MoS_2-FETs similar to the very first devices studied by Novoselov *et al.* [7]. Electrical transport measurements of a representative backgated, two-probe MoS_2 device is shown in Fig. 3.1. The conductance is varied by applying a backgate (V_g) using a

Keithley 2400 sourcemeter. The current is increased in the MoS_2 channel as V_g is increased and can be completely turned off by applying a negative V_g.

The field effect mobility can be expressed as $\mu_{FE} = (L/WC_g)(dR^{-1}/dV_g)$ where L,W, and R are the length, width and resistance of the device, respectively and $C_G \sim 116\ aF\mu m^{-2}$ is the geometrical capacitance between MoS_2 and the silicon back gate. The resistance (R) is calculated by taking the slope of the linear regime of the current (I) vs. V_g plots. For the device in Fig. 3.1, the μ_{FE} was calculated to be 8.22 cm^2/Vs. The room temperature mobility was comparable to values reported by Novoselov *et al.* [7]. As discussed in chapter 1, these mobility values are much smaller compared to theoretically predicted values [17].

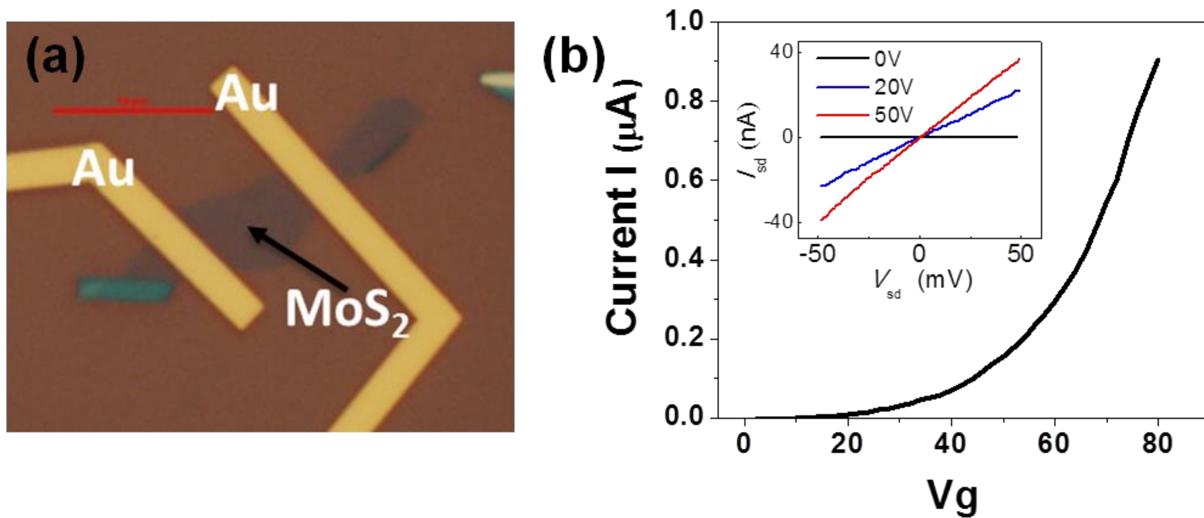

Figure 3.1 (a) *Optical image of a two-probe MoS_2-FET with Au-contacts. (b) Source-drain current vs. V_g of MoS_2 FET. Inset: linear I_{SD} vs. V_{SD} for various V_g values.*

As previously mentioned, scattering in MoS_2 devices can be caused by the following:

1. Metal contacts in MoS_2-FETs can scatter carriers before they reach MoS_2
2. Phonons in MoS_2 can scatter charge carriers inside the channel.
3. Carriers can be scattered by defects in MoS_2 or impurities in the substrate.

Unfortunately, two-probe measurement cannot be used to distinguish between different scattering mechanisms. To overcome this limitation we employ multi probe Hall bar shaped samples. We can study the first two mechanisms by studying multi-probe MoS_2 devices at low temperatures. From four-probe longitudinal resistance (R_{xx}), we can extract the contribution due to contacts (R_c) and also accurately measure the Hall mobility μ_{Hall}. From temperature-dependent measurements of R_{xx}, we can extract scattering contribution due to phonons. Finally, carrier density dependent mobility measurements can inform us about charge impurity scattering from the substrates.

3.3 Fabrication of high quality MoS_2 Hall-bar devices

By studying devices on different substrates, we can investigate substrate induced scattering. We fabricated multi-probe MoS_2 devices by patterning large (~300μm^2) flakes into a Hall bar geometry and carried out low temperature measurement in a closed cycle He-cryostat (details in Appendix: A7). Large MoS_2 flakes were first located on Si wafers with 300nm of thermal oxide on top. Once large flakes are identified and verified using Raman microscopy (Appendix:A2), a Hall bar shape is patterned on top of the flake using e-beam lithography (A6 496 PMMA is used as resist) (Fig. 3.2a). After developing in 3:1 MIBK:IPA for 1 minute, the resist around the Hall shape is removed. This allows us to pattern an arbitrary MoS_2 flake into a well-defined geometry with known dimensions, helping us to accurately measure resistance of the device. Parts of MoS_2 not covered by PMMA are removed (Fig. 3.2b) using a O_2 plasma etch (parameters: 30sccm, 120V, 5s). The PMMA was then removed using acetone leaving a well-defined MoS_2 flake with known dimensions. Another step of e-beam lithography was used to define and evaporate metal

contacts (50nm thick Au) to the MoS_2. To increase device quality we did not use chrome adhesion layer.

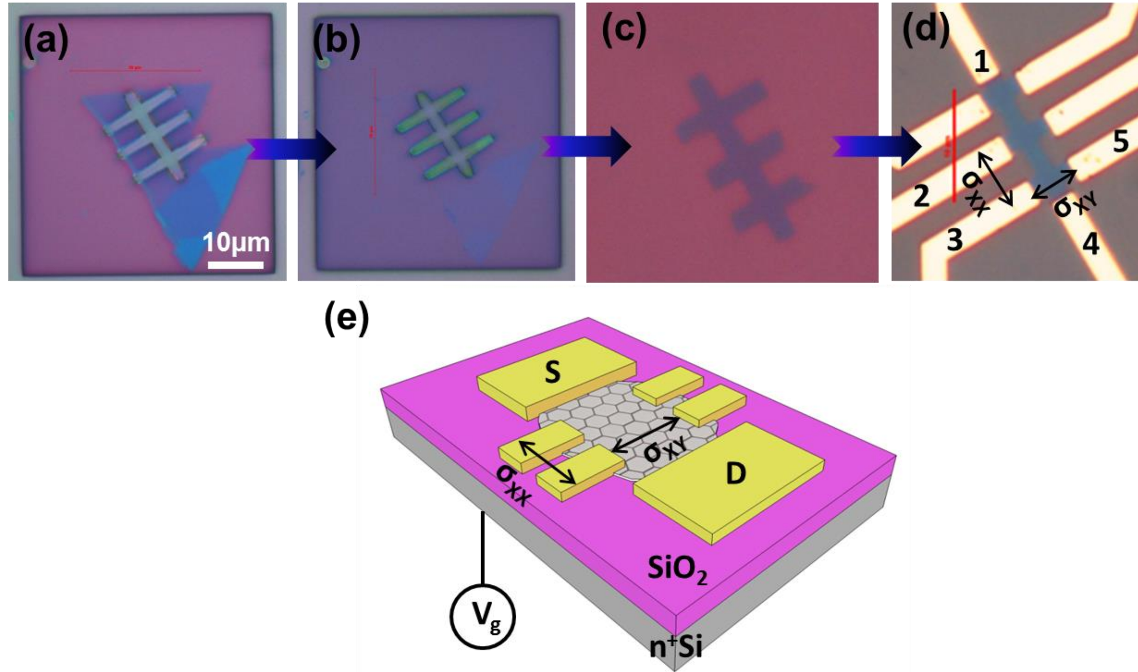

Figure 3.2 *(a) Large MoS_2 flake after patterning a PMMA Hall bar (Scale Bar is 10μm) (b) PMMA/MoS_2 flake after O_2 plasma etch. (c) After PMMA removal using acetone. (d) Final MoS_2 device with Cr/Au metal contacts. Resistivity (e) Finished multiprobe MoS_2-FET on SiO_2/Si substrate.*

In a typical measurement, current I_{DS} is sent between leads 1 and 4 (Figure 3.2d) while recording voltage V_{xx} between leads 2 and 3 and V_{xy} between leads 3 and 5.

Steps to measure Hall mobility are as follows:

- The channel resistance is determined as $R_{xx} = V_{xx}/I$,
- Sheet resistivity $\rho_{xx} = R_{xx}(W/L)$ is calculated where W is width of the device and L is the distance between lead 1 and 4
- Contact resistance is found $R_C = R_{2-probe} - R_{xx} = \frac{V_{DS}}{I_{DS}} - R_{xx}$
- Magnetic field is applied and the Hall resistance is given by $R_{xy} = V_{xy}/I$

- The carrier density $n = B/eR_{xy} = BI/eV_{xy}$,where B is the applied field.
- Finally, Hall mobility $\mu_{Hall} = 1/en\rho_{xx}$.

3.4 Temperature dependent Hall-mobility

Figure 3.3a shows Hall voltage V_{xy} vs. magnetic field (B) for different V_g at 4K. Figure 3.3b shows carrier densities n at different V_g values. Figure 3.3c shows the Hall mobility μ_{Hall} as a function of V_g at 4K and shows that the mobility increases with carrier density (n). In our high quality multi-probe FETs at 4K, we recorded μ_{Hall}= 500 cm^2/Vs for monolayer devices which is orders of magnitudes higher than μ_{FE} = 8.22 cm^2/Vs measured at similar temperatures for two-probe devices. This was the highest mobility reported in literature at the time of our measurements[5].

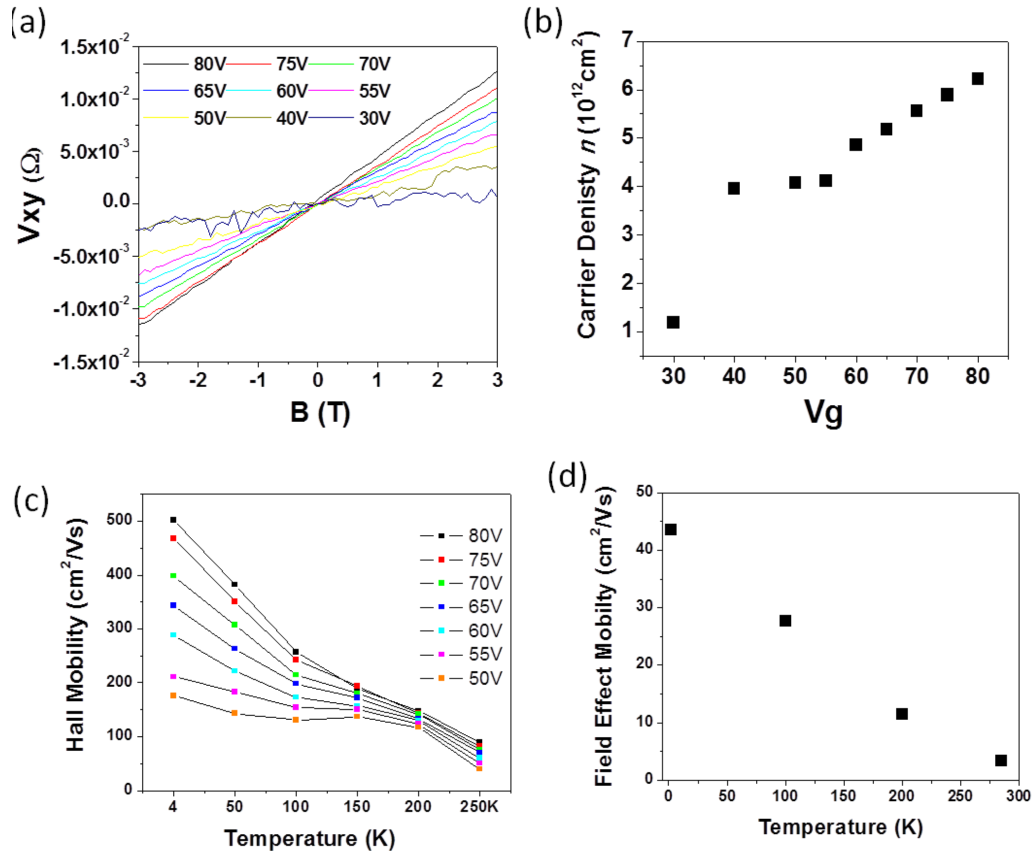

Figure 3.3 *(a) Hall voltage V_{xy} versus magnetic field B for various values of Vg measured at T=2K (b) Carrier density (calculated from Hall measurements) vs V_g. The capacitance calculated from slope of carrier density (n) vs V_g gives us Cg = 105 aFμm^{-2}. (c) Hall Mobility vs V_g at different temperature's (d) Field effect mobility vs V_g at various temperatures.*

3.5 Mobility limiting factors

Values for μ_{Hall} measured in our devices are much higher than μ_{FE} from two-probe devices (Fig. 3.3 c,d). To explain this, we separately analyzed effects of metal contacts and phonon scattering on carrier mobility of MoS_2.

I. Contact Resistance

As shown in the previous section, we can extract both sample resistance (R_{xx}) and contact resistance (R_c) through a combination of Hall and two-probe measurements. The sample resistance and contact resistance are plotted in Fig. 3.4 for various temperatures. We can see that the contact resistance is orders of magnitude higher than the sample resistance. In two-probe measurements, the total resistance is dominated by R_c. This high R_c values is likely caused by the formation of a Schottky barrier at the Au/MoS_2 interface. This arises due to the difference in work function between Au (~5.1eV) and MoS_2 (~4eV) [33-35]. We conclude that the Au contacts are not ideal for electron injection into two-probe MoS_2 devices. We also notice that R_c can be tuned with V_g which is indicative of gate modulation of the Schottky barrier height at Au/MoS_2 junction.

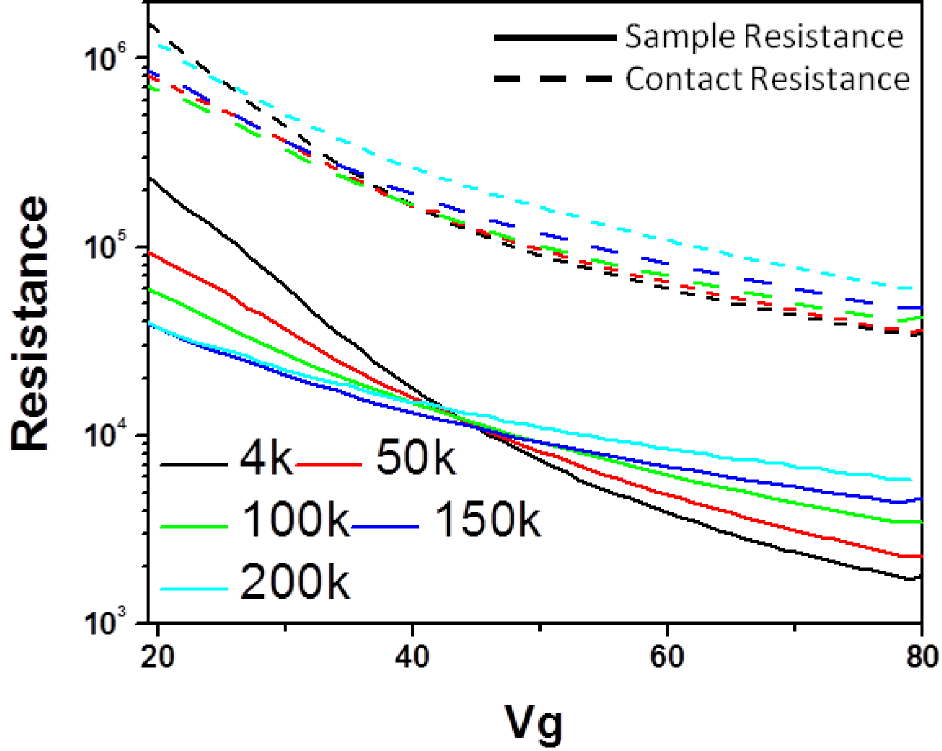

Fig 3.4 *Sample and contact resistance vs. V_g at various temperatures. Dotted lines are contact resistance values. Solid lines are sample resistance from Hall measurements*

II. Phonons in MoS_2

Figure 3.3 illustrates dependence of mobility on temperature. The observed decrease of carrier mobility with increasing temperature (*T*) is due to electron-phonons scattering in MoS_2.This is a clear indication of phonon limited transport. Theoretical calculations predict that scattering due to homopolar out-of-plane (~50meV) and polar optical (~48meV) phonons is dominant at temperatures T>100K [8]. It has been shown that in the temperature range 100K-300K the optical phonon limited mobility can be fitted to $\mu \sim T^{\gamma}$, where $\gamma \sim 1.7$ is predicted for monolayers MoS_2 [8]. It is predicted that homopolar out-of-plane mode can be quenched in top-gated samples leading to a decrease in the exponent to $\gamma = 1.52$ [8]. Our experimentally measured Hall mobility follows power law dependence with $\gamma \sim 1.09$ for temperatures T>100K (Fig. 3.5).

Jariwala *et al.*[36] have also shown γ values for uncapsulated MoS_2-FETs to be a lot lower. This variation in γ value may be due to variation of the crystalline quality of MoS_2 used in various studies and may indicate that better theory is needed.

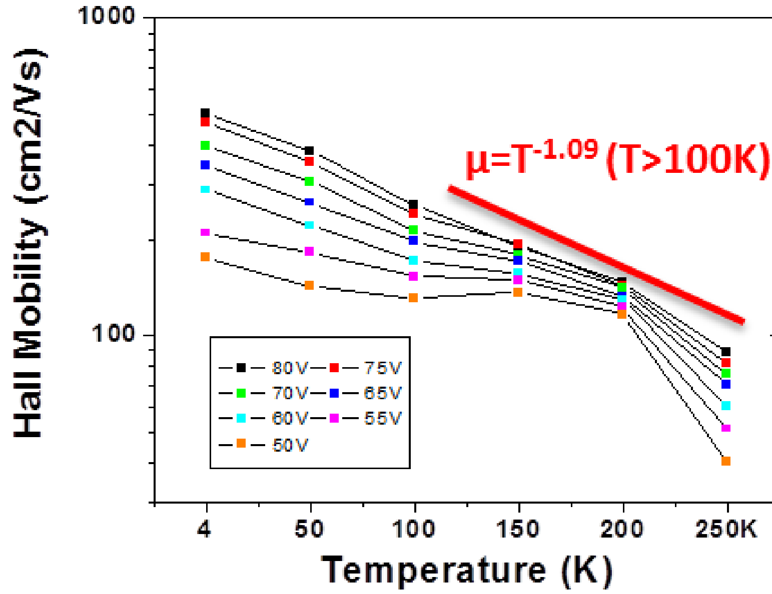

Fig 3.5 *μ_{HALL} vs temperature plotted in log scale. Phonon limited mobility (>100K) modelled using μ~$T^{-\gamma}$, γ=1.09.*

3.6 Metal to Insulator (MIT) Transition in MoS_2

In addition to previously considered scattering mechanisms in MoS_2, we found an interesting crossover in the conductivity ρ_{xx} vs. V_g data at different temperatures (Fig. 3.6). For V_g<40V, MoS_2 behaves as an insulator and its conductivity increases with temperature. At high n (V_g>40V), MoS_2 displays band-like transport and conductivity decreases with temperature. This type of carrier density n induced transition has been observed in materials with localized states. Studies have shown that sulfur vacancies create localized gap states in MoS_2. At low n, transport in MoS_2 takes place by hoping via defect-induced localized states. This short range disorder is the most likely source of dominant scattering mechanism at low temperatures.

The Ioffe-Regel criterion for disordered systems predicts a metal to insulator transition in a 2D semiconductor when $k_F l_e \sim 1$, where $k_F = \sqrt{2\pi n_{2D}}$, and $l_e = \sqrt{2\pi n_{2D}}\frac{\mu h}{2\pi e}$ is mean free path of electrons [37, 38]. The 2D system becomes metallic if $k_F l_e$>>1 and insulating if $k_F l_e$<<1. In fact at V_g=40V, $n = 3\times10^{12}\text{cm}^{-2}$, μ_{Hall} = 50cm^2/Vs, l_e~1.5nm, $k_F l_e$ = 0.6 which is very close to the Ioffe-Regel criterion hence showing the disordered nature of our MoS_2 system at low n. During the course of our study, *Kis et al.* [38] demonstrated a similar metal-insulator transition for top gated MoS_2 devices.

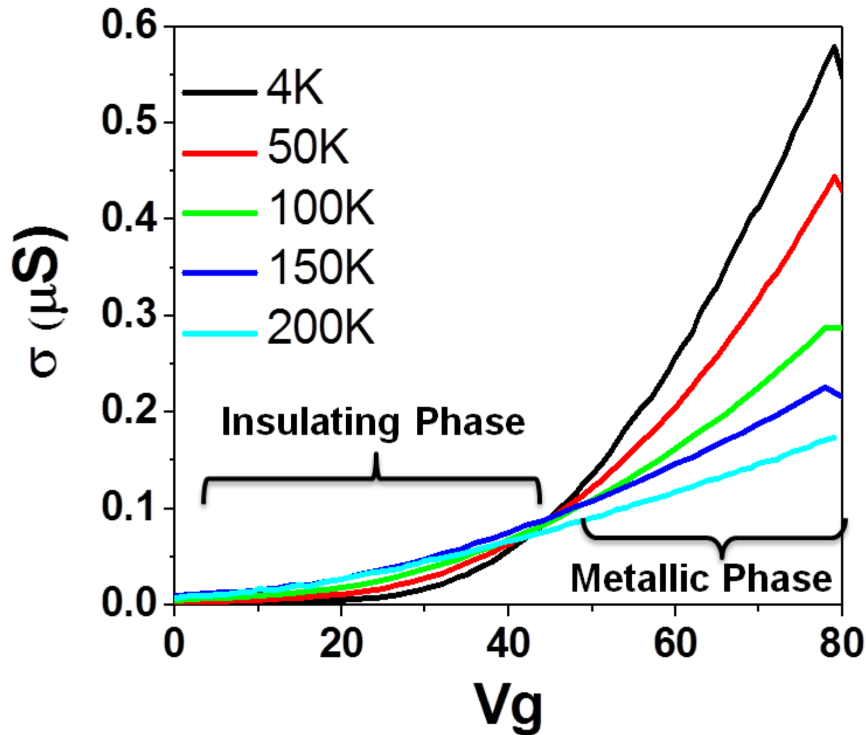

Fig 3.6 *Conductivity as a function of V_g at different temperatures showing metal-insulator transition in monolayer MoS_2.*

3.7 MoS_2 substrate engineering towards increasing mobility

All discussed MoS_2-FETs have been prepared on SiO_2/Si substrates. Electrons propagating in MoS_2 are also expected to scatter off of charged impurities in underlying SiO_2 substrates, similar

to the well-studied case of graphene [14, 24]. Our experimental results (Fig. 3.4) show hints of this. At low temperatures (4K), mobility shows a strong dependence on carrier density. We see that the mobility values go up with V_g at low temperatures (4K). At these temperatures we do not expect phonons to contribute to scattering. An increase in mobility at high carrier densities is indicative of screening of coulomb fields of charge impurity on SiO_2 by conduction electrons. Substrate engineering has been shown to alleviate effects of charge impurity scattering from SiO_2. Recent work has shown that transferring graphene on hexagonal Boron Nitride (BN) substrates can drastically enhance graphene electrical properties [39, 40]. BN is known to be atomically flat and chemically inert meaning there are not many charge impurities and dangling bonds on the surface. Using a transfer technique (Details in Appendix: A6), we transfer MoS_2 onto high quality BN flakes to make MoS_2/BN devices. By initially comparing simple two-probe MoS_2 devices on SiO_2 and on BN we can see differences in device characteristic (Fig. 3.7a,b)

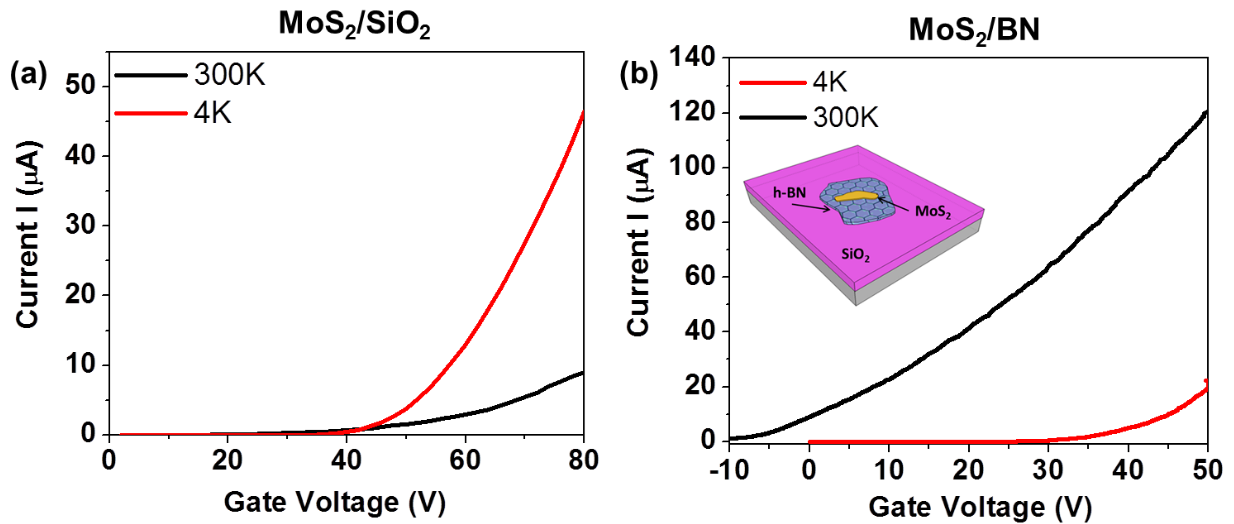

Figure 3.7 ***(a)*** *Field effect in MoS_2/SiO_2 devices* ***(b)*** *Field effect in MoS_2/BN devices*

First, MoS_2 device on SiO_2 have a significantly higher threshold voltage (~40V) at room temperature compared to devices on BN (Fig. 3.7b). Second, temperature dependent

measurements reveal that MoS_2 on SiO_2 is in an insulator as discussed in section 3.6 while MoS_2 on top of BN devices exhibit metallic behavior and is more conductive at low temperatures (4K). Finally, the room temperature field effect mobility of MoS_2/BN is slightly higher (~11cm^2/Vs) compared to MoS_2/SiO_2 (~8cm^2/Vs).

To get a clearer understanding of MoS_2/BN devices, we fabricated large area Hall-bar shaped devices (Fig. 3.8). The MoS_2 flake is highlighted with a white dotted line for clarity. Following the transfer procedure, Cr/Au (2nm/90nm) contacts were deposited using a combination of e-beam lithography and thermal deposition. An electrically contacted MoS_2/BN device is shown in Fig. 3.8b along with its photoluminescence image taken using a conventional fluorescence microscope setup. Unfortunately, electrical characterization of such large MoS_2/BN device was not possible due to the lack of good electrical contact across the large MoS_2 channel (Fig. 3.8c). To check the integrity of the MoS_2 flake on BN we looked at both photoluminescence spectra and Raman spectra of the MoS_2. The PL spectrum of MoS_2 on BN clearly has a smaller FWHM compared to MoS_2 on SiO_2. This may indicate reduced disorder in this sample. Unfortunately, Raman spectra of MoS_2 on BN are very weak compared to MoS_2 on SiO_2. This leads us to believe that there can be structural damage of MoS_2 during the transfer process. It is therefore essential to study the interface between MoS_2 and BN.

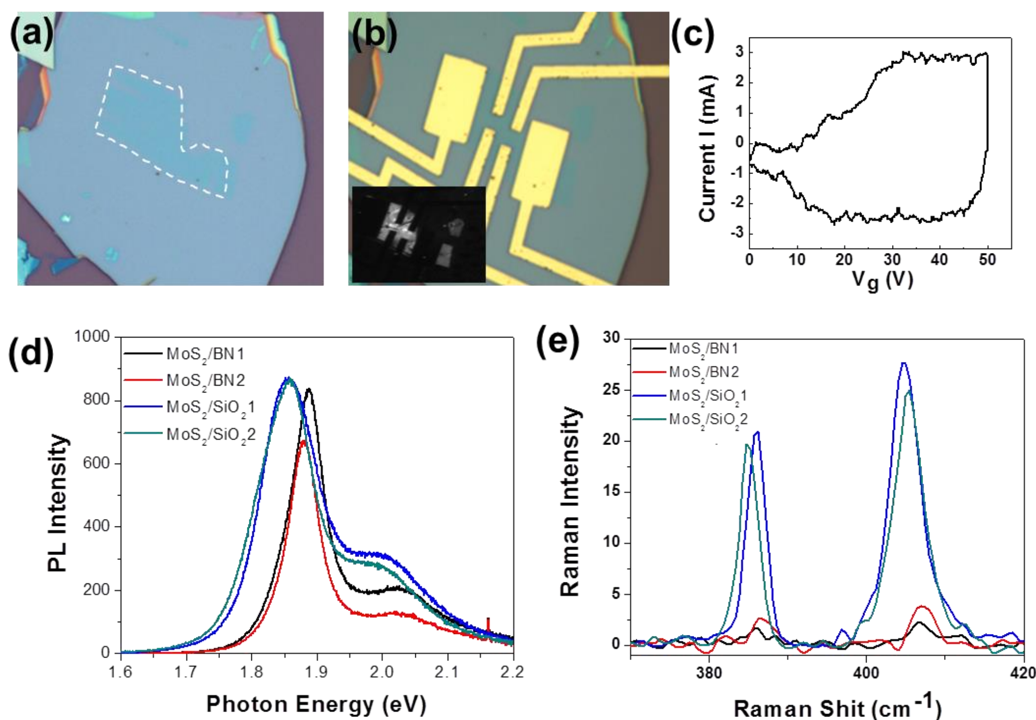

***Figure 3.8** (**a**) Optical image of MoS_2/BN device. MoS_2 highlighted with white dotted line. (**b**) Electrical transport in MoS_2/BN device with Cr/Au contacts. Inset: photoluminescence image of contacted MoS_2 flake (**c**) Current vs. V_g characteristic of MoS_2/BN device (**d**) Photoluminescence spectra of 2 different MoS_2/BN devices and MoS_2/SiO_2 devices (**e**) Raman spectra of MoS_2/BN and MoS_2/SiO_2 devices.*

Atomic force microscopy (tapping mode) was used to study the interface of large area MoS_2/BN devices. AFM of as pre-prepared MoS_2/BN devices reveals a high density of >20nm bubbles between MoS_2 and BN (Fig. 3.9). Unlike previously reported papers that show graphene conforming nicely to BN, it seems that MoS_2 transfer is little bit more restricted. We looked into trying different annealing recipes in an Ar/H_2 (flowrate: 100/10SCCM) environment to decrease the density of the bubbles and possibly migrate the bubbles to the edge of the MoS_2 flake. The results of the annealing are shown in Fig. 3.9. Annealing our MoS_2/BN samples at 300℃ for 2 hours does seem to agglomerate widely spaced bubbles into more concentrated structures (Fig. 3.9b). However, >20nm tall bubbles are still present and we believe that their presence is the

major reasons for failure of our MoS_2/BN devices. Annealing at higher temperatures (450℃) does seem to remove a majority of the bubbles but leads to deteriorate MoS_2. Degradation of MoS_2 at temperatures >300℃ is also observed for MoS_2/SiO_2 devices. Such devices have degraded electrical quality (bad gate response and low current levels). This highlights the need to develop transfer recipes (different transfer polymers, pre-annealing/treating of BN flakes) to fabricate MoS_2/BN substrates, and to understand the mechanism of bubble formation. With these improvements, carrier mobility of MoS_2 in MoS_2/BN can be further improved.

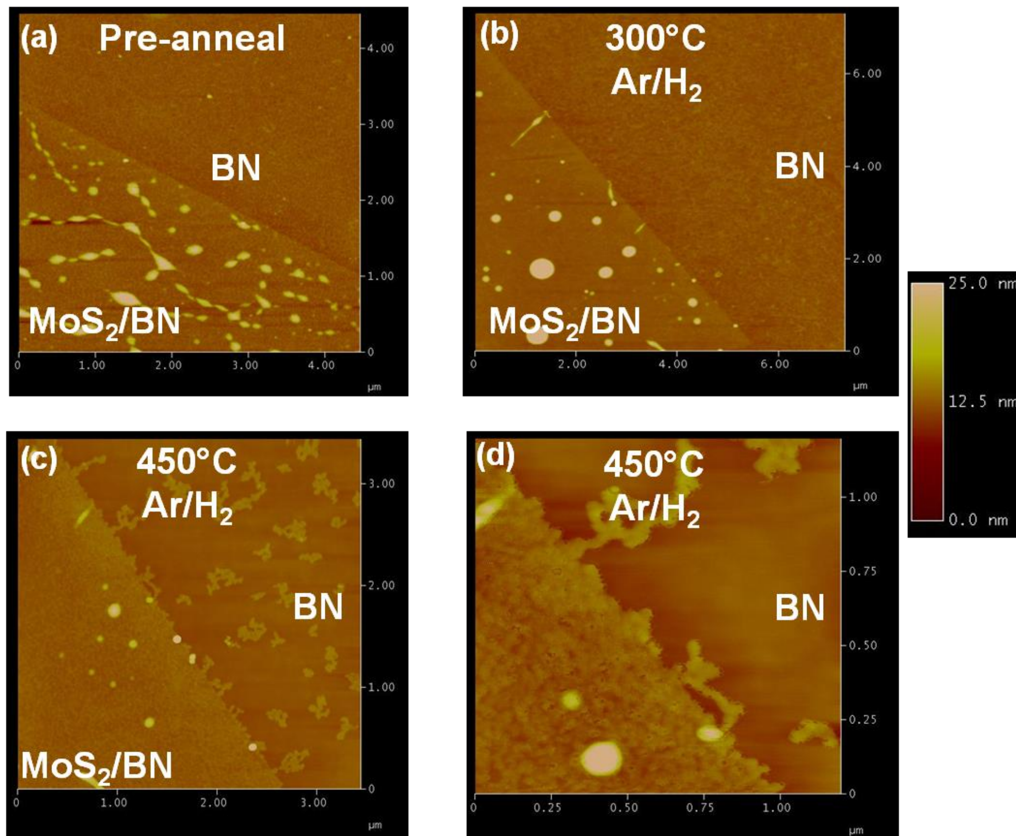

Figure 3.9 *AFM scan of MoS_2/BN devices before and after Ar/H_2 annealing at various temperatures* ***(a)*** *Pre-annealed MoS_2/BN devices* ***(b)*** *After annealing in Ar/H_2 at 300℃* ***(c-d)*** *After annealing in Ar/H_2 at 450℃.*

3.8 Dual gated MoS_2 devices to suppress Coulomb scattering

In the previous section we have shown that low-temperature mobility of MoS_2 is dominated by Coulomb scattering off of charge impurities on SiO_2. There can also be charged impurities/residues absorbed on the MoS_2 during the fabrication process which can act as scattering sites. Previous works on graphene have shown that it is possible to screen the effects of such scattering by placing the graphene in an environment with a high static dielectric constant [25]. Here we engineer the dielectric environment of MoS_2 by transferring BN (κ~4) onto a MoS_2/SiO_2 device. We also deposit a top electrode onto the BN/MoS2/SiO_2 device in order to dual-gate MoS_2. This device geometry has the added benefit of allowing us to further decrease contact resistance (R_c) by reaching higher carrier densities (Fig. 3.5) and also protecting the MoS_2 from environmental absorbates.

We fabricated high quality multi-probe monolayer MoS_2 devices (Fig. 3.10a). We then used the PDMS/polymer assisted transfer technique to transfer thin (5-10nm) of BN on top of the device (3.10b). We finally patterned and deposited a Cr/Au top electrode across device channel (Fig. 3.10c). A schematic of the dual gated device is shown in Fig. 3.10d. The carrier density in this device can be controlled by either Si backgate or Au top gate (Fig. 3.10e). Using dual gating we were able to reach very high carrier densities (~$2x10^{13}cm^{-2}$) and mobility ~$100cm^2/Vs$ (Fig. 3.10f). However, a direct comparison with MoS_2 on Si devices revealed that mobility in the former devices at similar carrier densities is actually lower. Hence, the direct effect of dielectric screening due to BN was not observed. Our BN top gated samples most probably suffer from the same interlayer bubbles shown in the previous section. This highlights the need to improve transfer techniques to carefully study such 2D-heterostructures and effects of dielectric screening of Coulomb scattering.

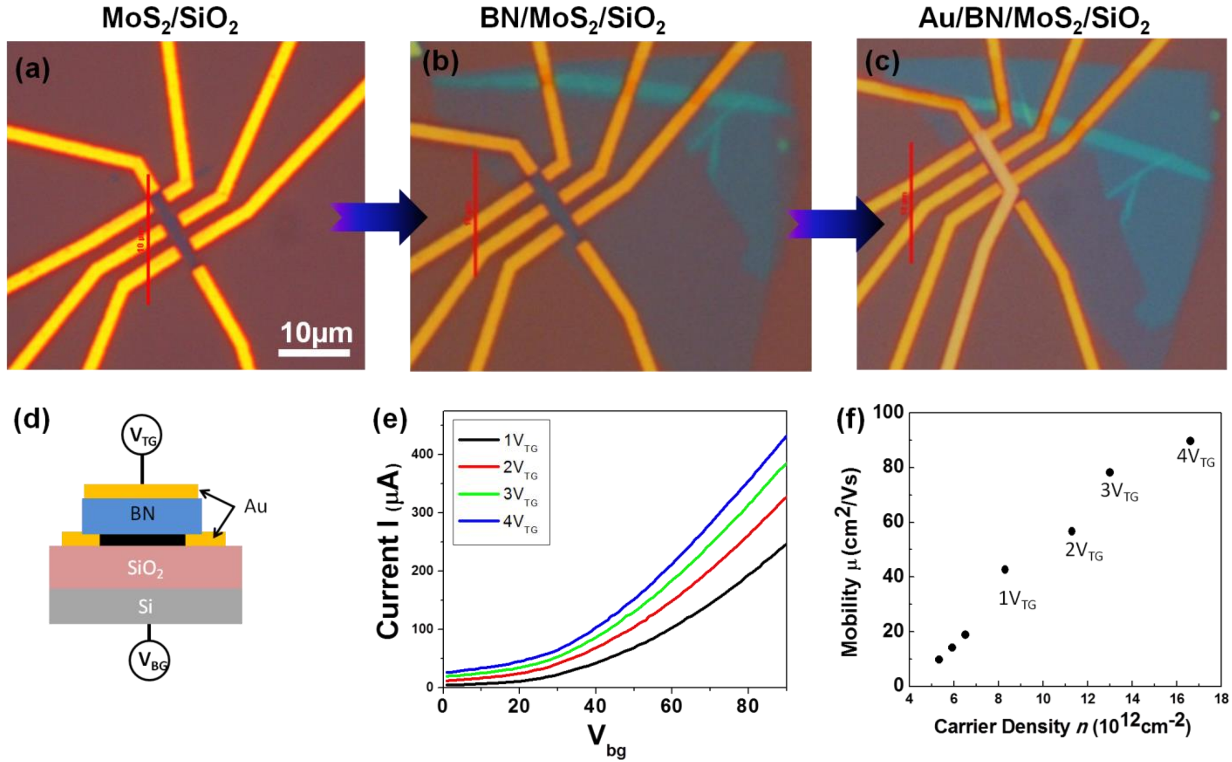

Figure 3.10 ***(a)*** *Multi-probe MoS_2/SiO_2 devices.* ***(b)****After transferring thin ~7nm BN on top of MoS_2 and Au electrodes.* ***(c)*** *After Cr/Au (2nm/80nm) top-gate deposition* ***(d)*** *Device schematic* ***(e)*** *Current versus V_g for dual gated MoS_2 devices.* ***(f)*** *Mobility vs carrier density for dual gated devices.*

3.9 Conclusion and Future Work

In this chapter we described a systematic method to study temperature dependent transport in monolayer MoS_2. We demonstrated the following:

- Contact effects account for most of the resistance in two-probe measurements if two probe MoS_2 devices. Hence, Hall effect measurements are essential for studying electronic properties of MoS_2. Once contact resistance was isolated, we achieved mobility ~500cm^2/Vs, the highest reported value at the time of measurement.
- At temperatures >100K , scattering is dominated by phonons in MoS_2.

- At low temperatures, scattering is dominated by Coulomb scattering, likely due to charge impurities on SiO_2.

We also demonstrated two approaches towards improving MoS_2-FETs: 1) substrate engineering and 2) dielectric engineering via BN top gates. While these approaches are promising, better transfer protocols need to be developed to make high-quality hybrid devices. Hexagonal boron nitride substrates are promising alternatives as substrates and top gate dielectric materials. However, to fully utilize the advantages of BN (low surface roughness, low density of surface impurity states), the interface between MoS_2 and BN needs to be free of any bubbles or defects.

Future development of MoS_2 electronic devices requires a careful study of scattering effects due to intrinsic defects. Recent STM studies have shown multilayer MoS_2 to have S vacancies [11]. A careful study of defects via STEM/STM and transport can guide growth techniques of TMDCs for future electronics. As an example, we examined defect density in synthesized $MoSe_2$ and MoS_2 from molybdenite using high resolution transmission electron microscopy (Fig. 3.11). We clearly observed that chemically synthesized $MoSe_2$ has a larger number of sulfur vacancies compared to naturally occurring MoS_2. Such studies should be carried out prior to making devices for transport studies.

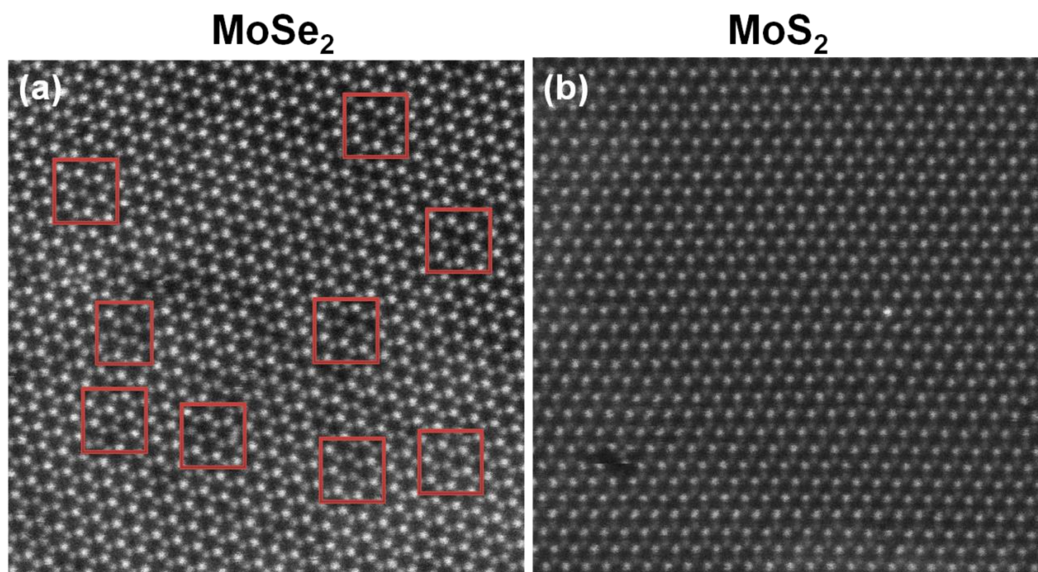

Figure 3.11 ***(a)*** *Z-contrast STEM image of synthesizes MoSe$_2$. Bright spots are Se$_2$. Red squares highlight area of synthesized MoSe$_2$ with high number of Se defects* ***(b)*** *STEM image of MoS$_2$. Bright spots are Mo atoms.*

CHAPTER 4: ELECTRICAL CONTROL OF OPTICAL PROPERTIES OF MONOLAYER MoS_2

In this chapter we discuss the results published in Solid State Comm., Newaz, Prasai *et al.*, "*Electrical control of optical properties of monolayer MoS_2*"[20]. We investigate electrical gating of photoluminescence and optical absorption in monolayer MoS_2 configured in a FET geometry and study the interplay between charge carriers and excitons in MoS_2. We demonstrate hundredfold increase in PL intensity and ~50% increase in MoS_2 absorption after gating MoS_2. We attribute this to the interaction of excitons in MoS_2 with free charge carriers via phase space filling effect.

4.1 Introduction

Materials with electrically controllable optical properties find uses in diverse applications ranging from electro-optical modulators to display screens. Unfortunately, the optical constants of most bulk semiconducting materials do not vary significantly with electric field. In the case of silicon, for instance, the variation in refractive index with gate voltage is smaller than 0.01%, limiting the footprint and the modulation depth of electro-optical modulators [41]. While larger electro-optical response has been demonstrated in other semiconductors, such as germanium and gallium arsenide, integration of these materials with silicon CMOS fabrication may prove difficult[42, 43]. In graphene, the most widely studied 2D material, changes in optical absorption larger than 100% produced by the electric field effect has been used to demonstrate nanoscale electro-optical modulators in the infrared range [44]. However, the lack of a band gap in graphene makes its uses at visible frequencies unfeasible.

As discussed in chapter 1, MoS_2 in its monolayer form is direct band gap semiconductor and is optically active. MoS_2 has an optical bandgap ~1.9eV modified by tightly bound excitons. In this section we optically investigate MoS_2-FETs and study how charge carriers induced via electrostatic gating interact with excitons in this system (Fig. 4.1 a,b,c)

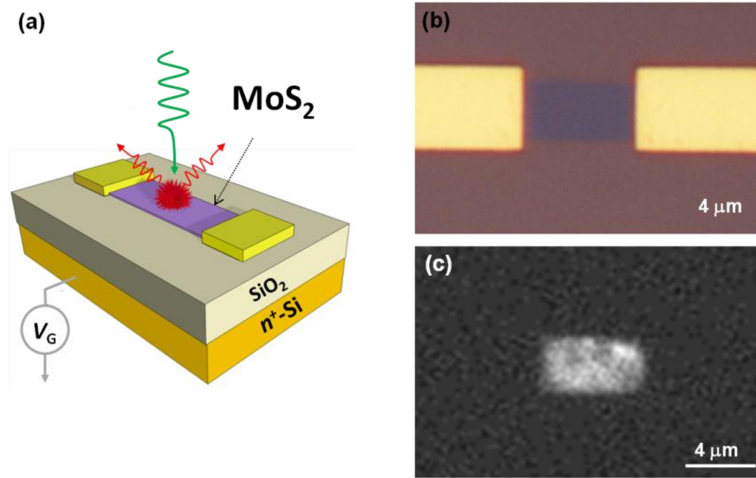

Figure 4.1 ***(a)*** *Schematic of MoS_2-FET device* ***(b)*** *Optical image of MoS_2-FET used for our studies* ***(c)*** *Fluorescence image of the same device collected using a conventional fluorescence microscopy setup with a 605-615nm bandpass filter and green light (530–590 nm) excitation.*

4.2 PL modulation in MoS_2-FETs

In the previous chapter we reported modulation of electrical conductivity in MoS_2 FETs using backgating. Here, we study changes in PL intensity of MoS_2 as a function of the carrier density n through backgate (V_g). All PL measurements were done using laser excitation with 1μW power at the wavelength 532nm. With changing V_g we notice drastic changes in PL intensity. In the range of gate voltages between +50 V and -50 V, the maximum PL intensity changes by more than factor of ~100 for a representative device in Fig. 4.2a. We see a hundredfold change in the PL intensity. Fluorescence image of the same device while changing V_g also shows the intensity of the monolayer flake changing. This process is completely

reversible as evident when looking at a series of fluorescence images while sweeping the gate voltage back and forth several times. This also rules out defect induced changes in the PL intensity. To better understand the origin of PL modulation we also study how absorption of MoS_2 changes with gate.

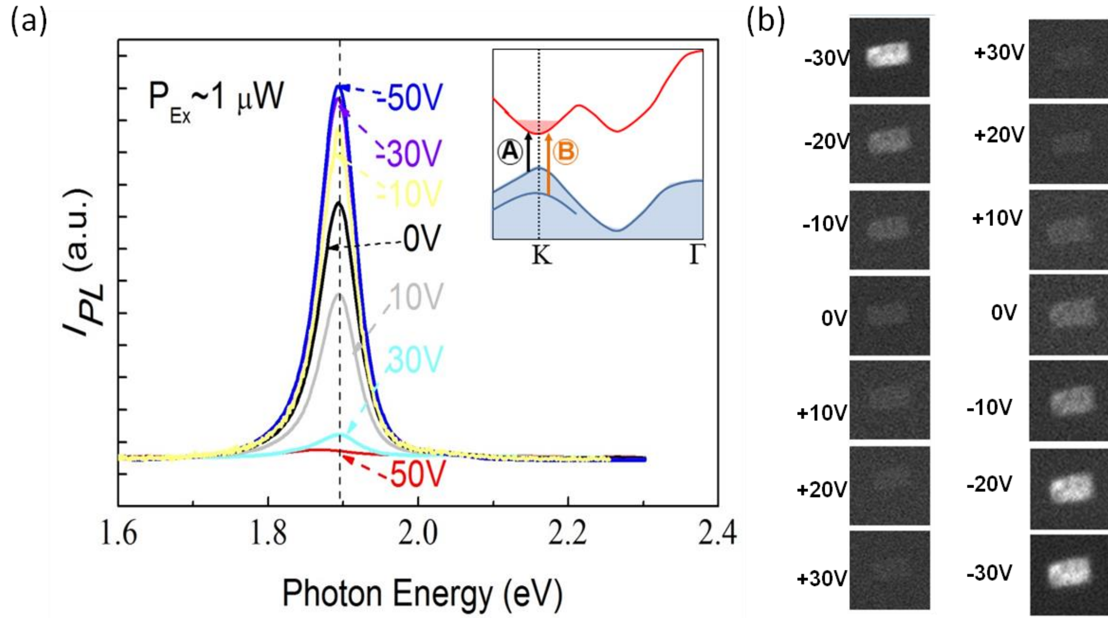

Figure 4.2 ***(a)*** *PL spectra of monolayer* MoS_2 *at different Vg. Inset: Band Structure of monolayer* MoS_2 ***(b)*** *Photoluminescence image of* MoS_2*-FET at various* V_g.

4.3 Absorption Modulation in MoS_2-FETs

In general, PL intensity can be described as:

$$I_{PL} \sim \alpha(\hbar\omega) \times \eta \sim \alpha(\hbar\omega) \frac{k_{rad}}{k_{rad} + k_{nonrad}}$$

Where, $\alpha(\hbar\omega)$ is the absorption coefficient at the excitation wavelength ν=532 nm (2.33 eV), η the luminescence quantum yield (number of photoexcited carriers per absorbed photon), k_{rad} and k_{nonrad} are respectively the rates of radiative and non-radiative transitions of photoexcited carriers[45].

It has been observed that an electrostatically induced shift of the Fermi energy in graphene affects the absorption *α(ħω)* at the excitation wavelength [46]. We conducted a differential reflectivity measurement to check if a similar phenomenon caused change in the absorption coefficient *α(ħω)* in monolayer MoS_2. Differential reflectivity at wavelengths corresponding to "A" and "B" peaks decreases with decreasing V_g (~50% change). At the same time, we observed no changes in diff. ref. at ~532nm, the wavelength of excitation in PL experiments.

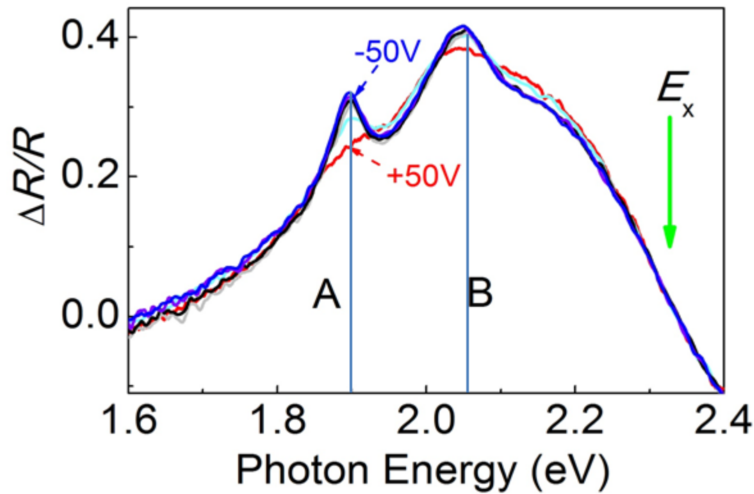

Figure 4.3 *Differential reflectivity (ΔR/R) measurement in monolayer MoS_2. Green arrow used to highlights the laser excitation energy (2.33 eV) used to record PL.*

This result is expected in the measured gate voltage range $\Delta V_g=100V$. In this range of V_g, field effect should produce variation in the carrier density $\Delta n=C_G\Delta V_g/e \sim 7\times10^{12}$ cm^{-2}. This change in the carrier density translates into a shift of the Fermi energy by $\pi\hbar^2 n/m_e$ ~ 60 meV, where $m_e \sim 0.3m_0$ *is* the effective electron mass in single layer MoS_2. This shift is small compared to the difference between fluorescence (1.85 eV) and excitation (2.33 eV) energies. Therefore, an electrostatically induced shift of the Fermi energy cannot account for the change in absorbance.

4.4 Elucidating mechanism of PL/Absorption modulation

We ascribe the observed modulation in photoluminescence and absorption to the phase space filling effect (PSF). In PSF, increase in carrier density due to field effect can make part of the phase space unavailable for exciton formation due to Pauli exclusion [47]. This in turn, causes a reduction in the exciton oscillator strength and a corresponding decrease of PL intensity and excitonic absorption. A simple estimate predicts that the PL intensity will be halved at the critical density of conduction electrons $n = 2/\pi a_o^2 \sim 6\, x\, 10^{12}\, cm^{-2}$, where $a_o \sim 1nm$ is an effect Bohr radius for an exciton. At this density (called "Mott density") electron-electron distance is equal to the exciton diameter. While this density is an order of magnitude larger than the variation of the carrier density $\Delta n \sim 7\, x\, 10^{12}\, cm^{-2}$ in our experiment, it is possible that this deviation is caused either by inaccuracies in the estimated exciton radius stemming from uncertainty in the dielectric constant of MoS_2 (for a monolayer MoS_2, the effective dielectric constant could be affected by either the underlying substrate or by the impurities on the surface of MoS_2). This phase space filling mechanism is consistent with what is observed in the bilayer case where the excitons and conduction electrons and excitons occupy different regions of the phase space. In the bilayer case the one-particle states that contribute to the formation of "A" and "B" excitons have momenta near the K-point while the conduction electrons reside away from the K-point. (Inset Fig. 4.4c)

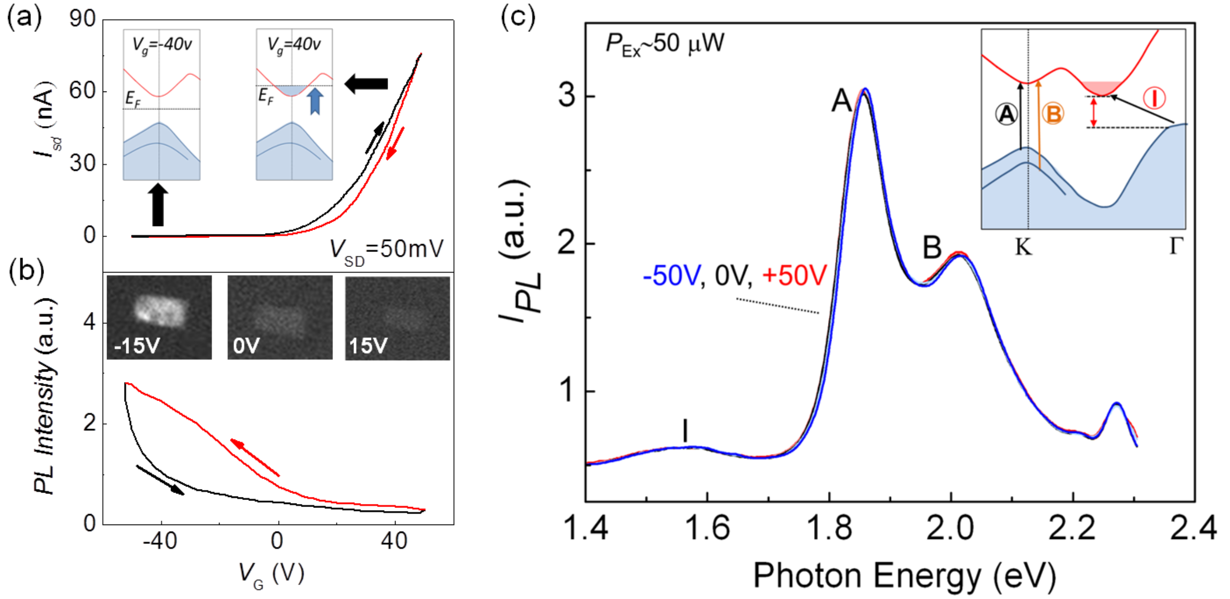

Figure 4.4 (a) *Electrical characterization of monolayer MoS2 FETs. (a) Source drain current I_{sd}vs. gate voltage V_g at applied source drain bias V_{sd}=50 mV. Inset shows the position of the E_F at V_g =-40V and +40V. At +40V free carriers occupy phase space decreasing osciallator strength of excitons forming at the K-point **(b)** The intensity of photoluminescence vs. V_g for the same device. The excitation wavelength was 2.33 eV, power ~ 1 μW, and the beam spot size ~ 1 μm. **(c)** PL spectra of a bilayer MoS_2-FET device recorded at gate voltages -50V,- 0V, 50V under 50 μW laser excitation power. Spectra at different V_g are unchanged. The inset shows the band structure of bilayer MoS_2. Along with "A" and "B" transitions, momentum-violating transition "I" across indirect band gap of bilayer MoS_2 is indicated.*

4.5 Power dependent PL modulation in MoS_2

At 532nm, laser with power P=1 µW was used as an excitation source in the experiments reported previously. In subsequent experiments, we discovered that the magnitude of PL modulation (PL_{-50V}/PL_{+50V}) depends dramatically on the power of the illumination. In most devices, PL modulation follows a $1/\sqrt{P}$ dependence (Fig. 4.5). We believe that this modulation can be ascribed to additional photoexcited carriers that are created at higher laser powers. Similar to conduction carriers, the presence of photoexcited carriers can lead to PL quenching.

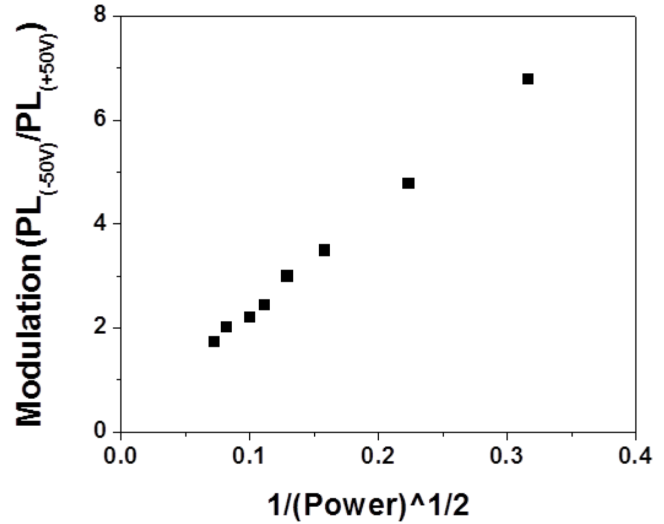

Figure 4.5 *Magnitude of PL modulation (PL_{-50V}/PL_{+50V}) vs $1/\sqrt{\textbf{Laser Power}}$.*

4.6 Trions in MoS_2

Two independent studies of gate independent PL of MoS_2 were published simultaneously with our work [48, 49]. They presented an alternate explanation to the observed change in optical properties of MoS_2 with electrical gating. By doing low temperature measurements PL they were able to spectrally identify signatures of tightly bound negative trions, quasiparticles composed of two electrons and a hole. These quasiparticles were shown to possess a binding energy (20-30 meV) and can only be identified at low temperatures. In the experiments of Heinz *et al.* and Ross *et al.,* the "A" exciton peak evolves into two resonances as the MoS_2 sample is electron doped ($V_g>0V$) (Fig. 4.6a). A lower energy resonance (A^-) is observed, which is attributed to trions. The reduction of PL intensity at high V_g at room temperature can be associated with transfer of the spectral weight from the "A" to broad "A^-" exciton (Fig. 4.6 a,b). The trion peak is however

broad and weaker due to thermal dissociation at room temperature. At low temperatures, the gated-induced trion peak intensity is comparable to the neutral excitons Fig. 4.6 c,d [49]. Overall, it is likely that this mechanism works in conjunction with previously discussed Pauli blocking.

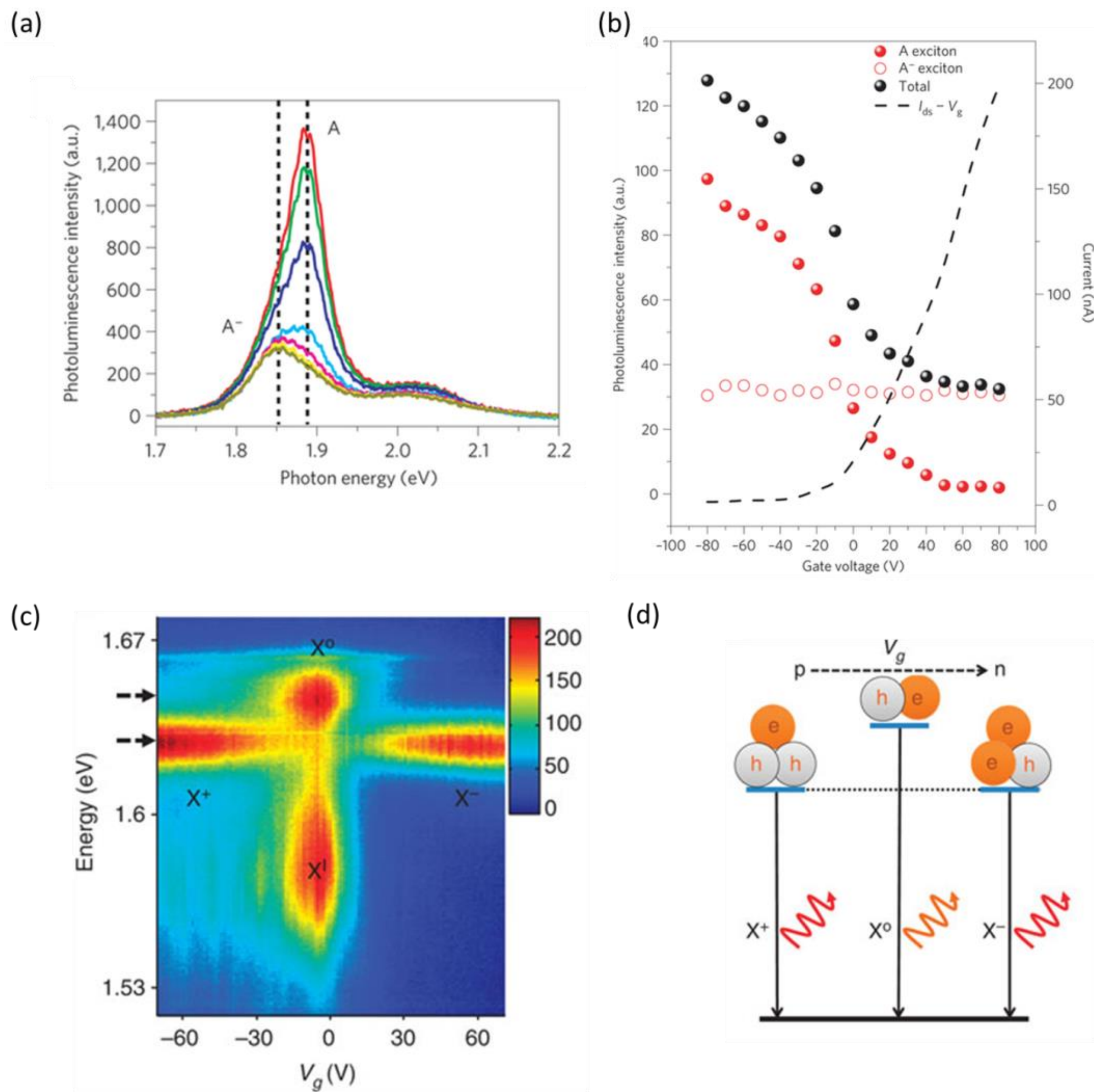

Figure 4.6 ***(a)*** *Photoluminescence spectra of MoS_2 at different Vg. Both neutral (A) and trion (A^-) features are identified.* ***(b)*** *Dependence on gate voltage of the drain–source current (right) and the integrated photoluminescence intensity of the A and A^- features and their total contribution (left).*

Adopted from reference [48] ***(c)*** *Photoluminescence color plot of* $MoSe_2$ *at different Vg. With large electron (hole) doping, negatively (positively) charged excitons dominate the spectrum.* ***(d)*** *Illustration of quasi-particle trion formation with n and p doping. Adopted from reference [49].*

4.7 Conclusion and Future Work

In summary, we investigated the interactions of tightly bound excitons with conduction electrons in monolayer MoS_2. We demonstrated electrical modulation of the optical excitonic absorption and PL in a MoS_2 FET, and attributed it to the phase space filling effect. Simultaneous work highlighted the effect of charged trions strong electron-exciton interaction coupled with controllable optical spin provides a platform to further study interesting excitonic physics. We intend to explore electron-exciton interaction at very high carrier densities $>10^{13}cm^2$ which cannot be achieved with current SiO_2/Si backgates. In this regime, we intent to investigate complex many body states such as biexcitons and bound excitons. One can also explore the effect of varying the dielectric environment on exciton binding energy. Finally, we envision the use of monolayer TMDCs in bioimaging. The strong effects of external doping on excitonic PL/absorption in MoS_2 and other monolayer TMDCs could be used for direct visualization of changes in electrical field induced by a biological system positioned on top of monolayer TMDCs.

CHAPTER 5: ELECTRICAL CONTROL OF NEAR-FIELD ENERGY TRANSFER BETWEEN QUANTUM DOTS AND MONOLAYER MoS_2

In this chapter we discuss the results published in *Nano Letters*, "*Electrical control of near-Field Energy Transfer between Quantum Dots and Two-dimensional Semiconductors"*[22]. This is a continuation of our work discussed in Chapter 4. In this study we investigate how a sub-monolayer of 0-dimensional quantum dots (QDs) interacts with a 2D-semiconductor MoS_2. We demonstrate efficient nonradiative Förster resonant energy transfer (FRET) from QDs into MoS_2 and prove that modest gate-induced variation in the excitonic absorption of MoS_2 leads to large changes in the FRET rate. This allows for up to ~75% electrical modulation of QD photoluminescence intensity.

5.1 Introduction

Nanoscale optical emitters – such as semiconductor quantum dots (QDs) or fluorophores - are strongly affected by their environment. An optical excitation in a nanoemitter can be transferred into the environment non-radiatively via processes such as charge transfer and Förster resonant energy transfer (FRET). Among these processes, FRET is a uniquely efficient long-range optical process.[50] Electrical control of FRET is desirable for potential applications of nanoemitters. To enable such control, materials with optical properties that respond to electric field are required. As discussed in chapter 4, due to the atomic thickness of MoS_2, its optical parameters can be controlled via electrostatic gating.[20, 46, 48, 49] We therefore expect that by placing a nanoemitter onto a 2D material like MoS_2, it may be possible to electrically control

FRET pathway between the two systems. In this chapter, we investigate near-field energy transfer between core-shell CdSSe QDs and 2-D semiconductor (2DSC), monolayer MoS_2.

5.2 Förster Resonant Energy Transfer (FRET) between MoS_2 and QDs

To explore near-field energy transfer between QDs and 2D-semiconductors (2DSCs) MoS_2, it is important to understand the conditions under which this type of transfer is expected. In general, FRET between two systems depends on their separation distance and the overlap between their absorption and emission spectra. The Fermi golden rule yields the following estimate for the FRET rate between 0D systems [50-52]:

$$k_{FRET(0D-0D)} \sim \left|\vec{E}\right|^2 \int_0^\infty \varepsilon_A(\lambda) f(\lambda) \lambda^4 d\lambda.$$

Here $\left|\vec{E}\right|^2$ is the square of electric field created by a QD dipole at the position of the other QD, $f(\lambda)$ is the normalized emission spectrum of the donor QD as a function of wavelength λ, and $\varepsilon_A(\lambda)$ is the acceptor molar extinction coefficient. Since dipole field decays with distance as r^{-3}, $\left|\vec{E}\right|^2$ is proportional to r^{-6}. For the case of FRET between a 0D and a 2D system, we can formally split a 2D material into a 2D array of point-like absorbers and then integrate $k_{FRET(0D-0D)}$ over 2D material area. If the 2D material is located in oXY plane and a QD is elevated above that plane by distance *d*, the distance *r* between QD and the point on the plane can be written as $r = \sqrt{d^2 + x^2 + y^2}$. Then integration over area yields:

$$k_{FRET(0D-2D)} \sim \int_{Area} d(Area)\, k_{FRET(0D-0D)} \sim \int_{Area} \frac{dxdy}{\sqrt{d^2 + x^2 + y^2}^6} \int_0^\infty \varepsilon_A(\lambda) f(\lambda) \lambda^4 d\lambda.$$

Replacing absorptivity $\varepsilon_A(\lambda)$ by 2D absorption coefficient $\alpha(\lambda)$ and performing simple integration over area we obtain a simplified expression:

$$k_{FRET} \sim \frac{1}{d^4} \int_0^\infty \alpha(\lambda) f(\lambda) \lambda^4 d\lambda. \quad (1)$$

In this expression $f(\lambda)$ is the normalized emission of QDs, $\alpha(\lambda)$ is the absorption coefficient for a 2DSC as a function of wavelength λ, and d is the distance between QDs and a 2DSC. The peculiar d^{-4} dependence of k_{FRET} is a characteristic of near-field coupling between excitations in 0D and 2D systems.[50, 52] Equation (1) indicates that in order to observe large k_{FRET}, the following conditions must be satisfied: *(i)* The optical absorption of the 2DSC must be sizable at the QD emission wavelength. *(ii)* A QD/2DSC separation d must be small. *(iii)* The lifetime of an exciton in QDs, τ_{QD}, must be longer than the inverse rate of energy transfer, k_{FRET}^{-1}. When this condition is fulfilled, an exciton in a QD lives long enough to transfer its energy into a 2DSC.

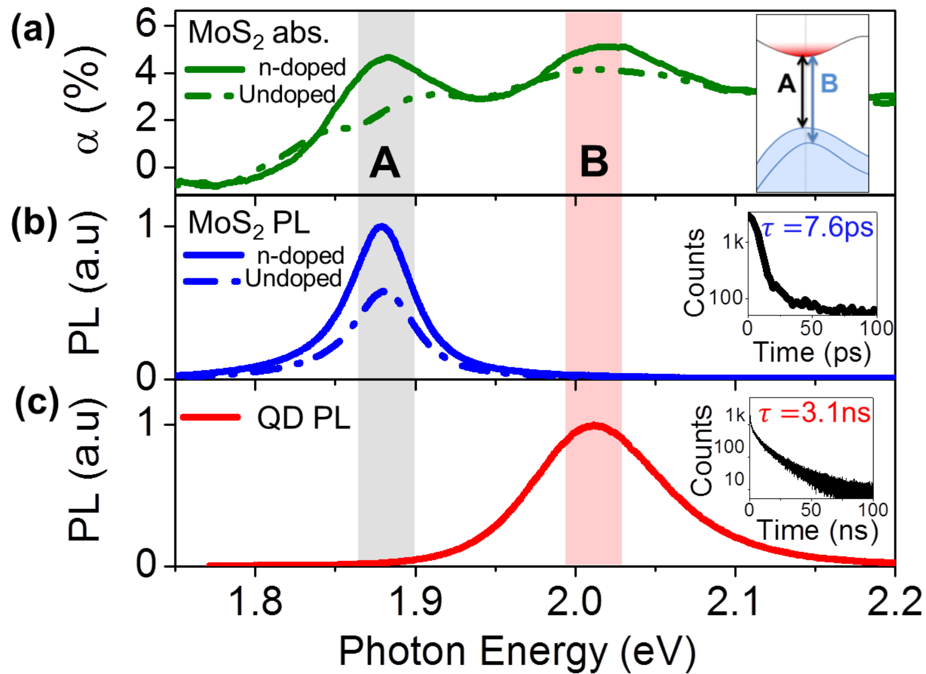

Figure 5.1 ***(a)*** *Absorption spectra of monolayer* MoS_2 *at two different doping levels. Inset: bandstructure of* MoS_2 *near its K-point.* ***(b)*** *PL spectra of monolayer* MoS_2 *at two different doping levels. Inset: time-resolved PL due to A-excitons in* MoS_2*.* ***(c)*** *PL spectrum of CdSSe QDs. Inset: time-resolved PL of excitons in QDs.*

We can now select the appropriate materials to observe and explore FRET between QDs and 2DSCs. From the diverse group of 2DSCs (*e.g.*: MoS_2, WSe_2, WS_2), we chose monolayer MoS_2, a direct band gap semiconductor that is well studied, readily available, and optically active in the visible range.[3, 53] The absorption spectrum of MoS_2 (Fig. 5.1a) is dominated by two strong excitonic PL peaks at 1.88eV (A) and 2.05eV (B). These features are due to absorption of light by tightly bound band-edge A- and B-excitons[54-57] residing at the K-point of the Brillouin zone (Fig 5.1a, inset). The energy separation between the excitons is due to strong spin-orbit interaction[57] that splits the valence band of MoS_2. The photoluminescence spectrum of MoS_2 is dominated by A-excitons, the lowest excited state (Fig. 5.1b). With increased electron doping, both absorption (Fig. 5.1a, dashed line) and photoluminescence (Fig. 5.1b, dashed line) of MoS_2 are strongly reduced for energies corresponding to A- and B-peaks. As discussed in Chapter 4, this strong electro-optical effect is related to the interaction between excitons and free charge carriers in MoS_2. Doping-induced reduction of absorption is attributed to a combination of phase-space filling effect (blocking of low-momentum states that are needed for exciton formation) and screening of electron-hole interactions by free carriers.[58, 59] Additionally, doping allows the formation of charged excitons (trions), [48, 49] that become the new lowest-energy excitonic state and hence modify the PL spectrum.

We chose compositionally graded alloy core-shell CdSSe QDs[60] as the emission source. The QDs were synthesized to emit at ~2.02eV (Fig. 5.1c), very close to the B-peak in the absorption spectrum of MoS_2 (Fig. 5.1a). Additionally, CdSSe QDs are bright (quantum yield ~50%) and have lifetimes ~3ns (Fig. 5.1c, Inset). This is much longer than the ~8ps lifetime of excitons in MoS_2 (Fig. 5.1b, Inset; see "Methods" for measurement details). This ensures that FRET will be directed from QDs to MoS_2 [61, 62]. Due to the spectral separation between the PL

peaks of QDs and MoS_2, their spectra can be analyzed independently in hybrid structures. Having selected the appropriate materials to observe FRET, we developed fabrication techniques (details in appendix: A8-11) to make hybrid QD/MoS_2 devices where MoS_2 is electrically contacted and its optical properties can be tuned electrostatically.

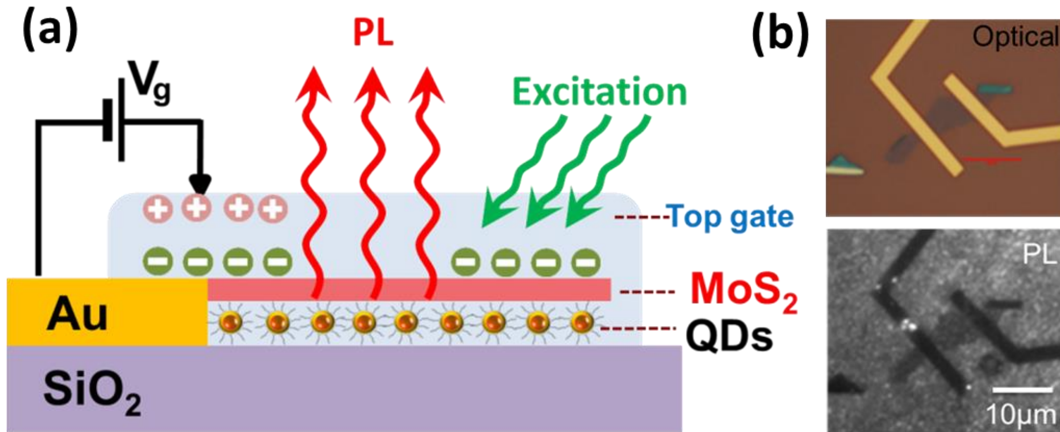

Figure 5.2 (a) *Device schematic of electrolyte gated QD/MoS_2 hybrid. Optical and photoluminescence images of an electrically contacted QD/MoS_2 device.*

5.3 Experimental evidence of FRET

Prior to studying electrically connected QD/MoS_2 devices it is natural to first examine ungated (V_g=0) QD/MoS_2 devices. Such an ungated QD/MoS_2 sample along with its optical and PL image is shown in Fig. 5.3a. Both the PL image and PL spectra (Fig. 5.3 a,b) indicate strong suppression of photoluminescence for the QDs that are close to MoS_2. To quantify this effect, we introduce the quenching factor $Q = I_{QD}/I_{QD/MoS_2}$. Here I_{QD/MoS_2} is the height of the QD photoluminescence peak at 2.02eV for the hybrid QD/MoS_2 device (acquired at a point marked red in Fig. 3a), and I_{QD} is the height of the same peak from QDs away from MoS_2 (acquired at a point marked black in Fig. 5.3a). We calculate $Q(0V)$~4.8 from the data shown in Fig. 5.4b. We also observed that the lifetimes of QDs reduce by a similar amount due to the presence of MoS_2,

$\tau_{QD}/\tau_{QD/MoS_2}$~ 4.4 (Fig. 5.3b, Inset). At the same time, the position of the PL peak due to QDs remained virtually unchanged at about ~2.02eV (Fig. 5.3b). This indicates that the QDs are not chemically or mechanically perturbed by MoS_2.

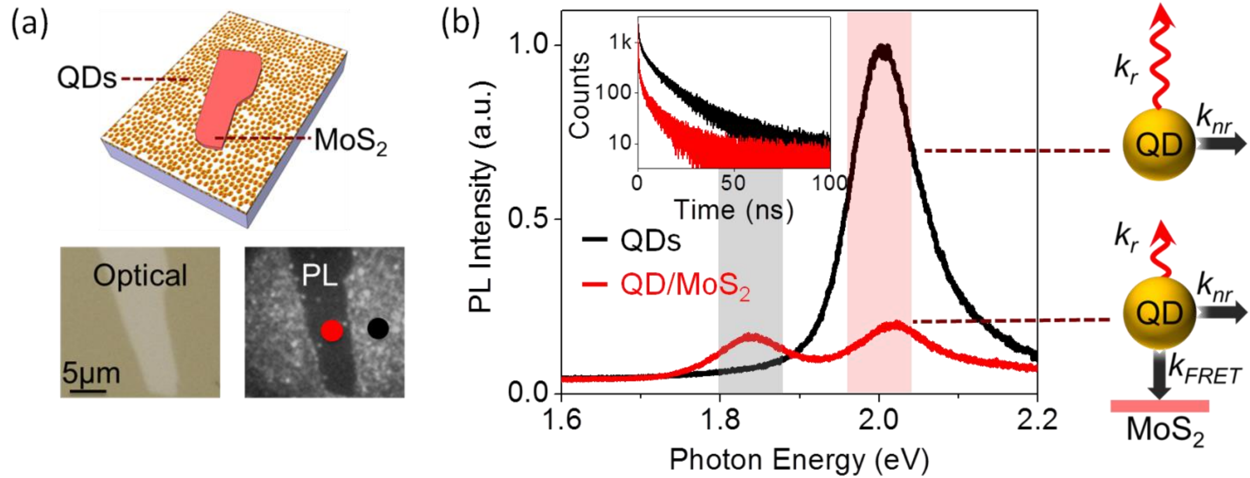

Figure 5.3 ***(a)*** *Ungated MoS_2/QD device along with its optical (left) and photoluminescence (right) images. PL image was recorded using a band-pass filter (605nm-615nm) only transmitting QD emission.* ***(b)*** *PL spectra and time-resolved PL (Inset) of QD/MoS_2 hybrid (red) and of bare QD film (black). The spectra were recorded from the same device shown in Fig. 3a at positions marked by red and black circles. The schematic on the right illustrates FRET between a QD and MoS_2.*

The quenched PL and decreased lifetimes indicate the opening of an additional non-radiative relaxation channel for the QDs next to MoS_2. We attribute this pathway to FRET. Strong spectral overlap between the emission spectrum of QDs and B-peak in absorption of MoS_2 coupled with very small QD/MoS_2 separation should, according to Eq. (1), lead to large k_{FRET}. Prior experiments on similar QDs next to 2D systems (graphene, MoS_2) arrived at a similar conclusion [63, 64].

The QD/MoS_2 FRET rate was estimated from measured suppression of QD photoluminescence and lifetimes. The intensity of QD photoluminescence depends on radiative (k_r) and non-radiative ($k_{nr,}k_{FRET}$) decay rates:

$$I_{QD} \sim \frac{k_r}{k_r + k_{nr}} = k_r \tau_{QD},$$

$$I_{QD/MoS_2} \sim \frac{k_r}{k_r + k_{nr} + k_{FRET}} = k_r \tau_{QD/MoS_2}. \quad (2)$$

In these equations, the lifetime of a QD is expressed as an inverse of the sum of radiative and non-radiative rates, and k_r is assumed to be unaffected by the environment. Equation (2) confirms that near-equal suppression of QD lifetime and PL intensity observed in our experiments is an expected consequence of FRET. From the measured PL quenching $Q \sim 4.8$, using equation (2) we determined $k_{FRET} = (Q-1)/\tau_{QD} \sim (1.1 \pm 0.2) \times 10^9 \mathrm{s}^{-1}$. Importantly, this rate corresponds to lifetime ~1ns, shorter than the intrinsic QD lifetime of ~3ns. From measured Q and assuming separation distance between QD-core and MoS_2 ~3.5nm (Fig 2b, inset), we evaluate FRET radius R_0~5nm.

5.4 Electrical modulation of FRET

Finally, we examined gate-induced modification of the optical properties of QD/MoS_2 devices. To enable such a study, we used fabrication described in the appendix A8-11. An optically transparent solid electrolyte was then deposited onto MoS_2 (Fig 5.2a). This configuration allows us to vary the carrier density inside MoS_2 while being able to perform optical measurements. It is also important to note that electric field is near-absent at the location of QDs and cannot affect their photoluminescence directly [65]. Although very high carrier densities, $n \sim 10^{14}$ cm^{-2}, can be reached with electrolyte gates,[66] our devices require much

smaller densities, $n \sim 10^{13}$ cm^{-2}, and efficiently operate at low gate voltages (-2V<V_g<2V). Overall, we fabricated and measured 4 devices including the representative device shown in Fig. 5.4a.

With increased electron doping (positive V_g), we observed a well-known suppression of the PL peak [20, 48] due to MoS_2 at 1.88eV as discussed earlier (Fig. 5.1a). On the other hand, photoluminescence of QDs at ~2.02eV strongly increases with V_g (Fig. 5.4). In our best device, we observed up to ~75% modulation of the QD photoluminescence intensity for V_g between -2V and 2V. This effect is reproducible for all measured devices and is stable over multiple sweeps of V_g (Fig. 5.4, Inset).

We attribute the modulation of PL to gate-induced modulation of the FRET rate k_{FRET}. Indeed, as discussed above, optical absorption $\alpha(\lambda)$ of MoS_2 is strongly changing with V_g at $2.05eV$, the energy corresponding to QD emission (Fig. 1c). According to equation (1), changes in $\alpha(\lambda)$ should lead to modulation of the FRET rate, and hence QD PL intensity.

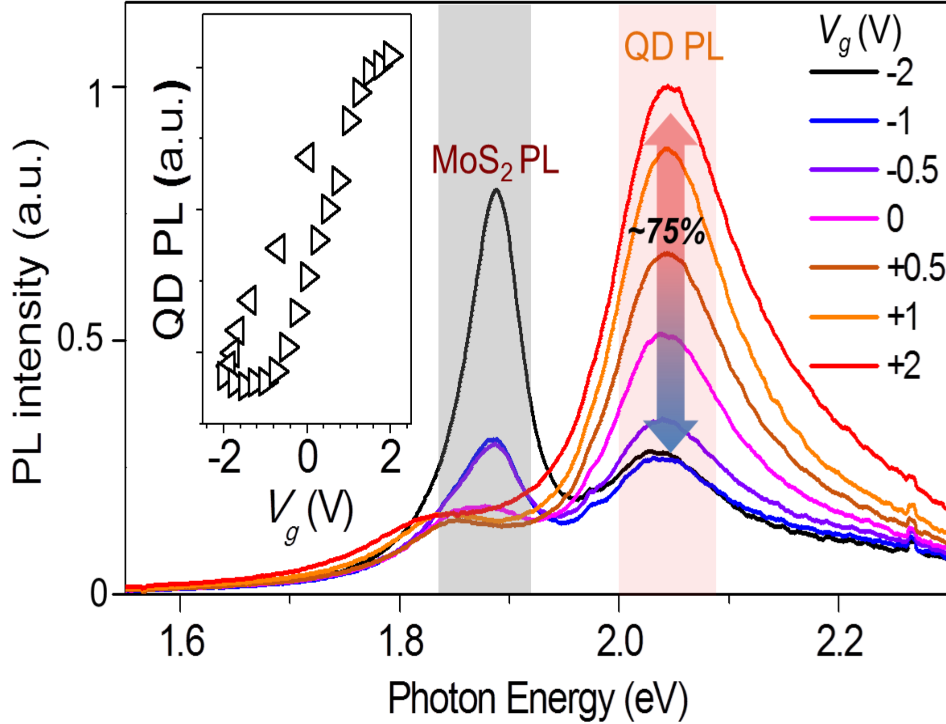

Figure 5.4 *PL spectra of a QD/MoS_2 device at different V_g. Inset: QD photoluminescence intensity vs. V_g during a back-and-forth sweep between +2V and -2V.*

5.5 FRET modulation and MoS_2 absorption

Our next goal is to understand the relationship between FRET modulation and MoS_2 absorption. We devised a simple model relating near-field FRET rate and quenching factor to far-field absorption of MoS_2. The normalized emission spectrum of an individual QD centered at wavelength λ is narrow compared to the relatively broad absorption features of MoS_2 [67]. In this situation, equation (1) can be simplified to

$$k_{FRET} \sim \frac{1}{d^4} \alpha(\lambda, V_g).$$

Combining this with equation (2), we obtain the following expression for the quenching factor Q:

$$Q\left(\lambda, V_g\right) = \frac{\tau_{QD}}{\tau_{QD/MoS_2}} = 1 + \tau_{QD} k_{FRET} = 1 + A\alpha\left(\lambda, V_g\right). \tag{3}$$

Here $A \sim \frac{\tau_{QD}}{d^4}$ is a proportionality constant relating the quenching factor to absorption of MoS_2. From experimentally measured $Q(V_g{=}0) \sim 5$ (Fig. 5.4) and $\alpha(V_g{=}0) \sim 5\%$ (Fig. 5.1) at λ=610nm (QD emission peak), we find $A = (Q(0) - 1)/\alpha(0) \sim 80$. The large value of A translates to large electrical modulation of PL of the QDs. To check the validity of our model, we created a $Q(\alpha)$ parametric plot from experimentally acquired values of Q and α. A QD/MoS_2 device (Fig. 5.5) was used for measurements of the quenching factor Q *vs.* V_g. However, absorption of the MoS_2 layer, α_{MoS_2}, could not be determined in the same device due to the strong background absorption of the QDs. For that reason, a separate MoS_2-only device without QDs was used for α_{MoS_2} *vs.* V_g measurements. In a separate measurement on a device without a QD layer, we used confocal transmission microscopy to record gate-induced transmittance modulation of MoS_2.

The absorption spectrum of MoS_2 could not be obtained directly from standard differential reflectivity measurements for our electrolyte gated MoS_2 samples. This is due to the non-uniformity of the solid electrolyte layer. Instead, we used confocal transmission microscopy to determine transmittance modulation of gated MoS_2 devices on transparent glass substrates (Fig. 5.5a). Experimentally (Fig. 5.5a), a broad (~1mm) light beam from a fiber-coupled halogen light source was used to illuminate our sample. Light passed through the sample was collected through a 40X objective and was further magnified ~10 times and focused on a screen with a ~0.5mm diameter pinhole. A magnified image of the device was projected on the screen. The pinhole was adjusted to block the light from the rest of the sample while transmitting light that

passes through MoS_2. The spectrum of the transmitted light as a function of gate voltage was recorded using Shamrock 303i spectrometer.

Transmittance modulation is defined as $M = \left(I\left(\hbar\omega,\ V_g\right) - I(\hbar\omega,\ 0V)\right)/I(\hbar\omega,\ 0V)$, where $I\left(\hbar\omega, V_g\right)$ is the intensity of light transmitted through MoS_2 at photon energy $\hbar\omega$ and gate voltage V_g. Transmittance modulation is closely related to absorption modulation. We can rewrite the definition of M as

$$M = \frac{\frac{I\left(\hbar\omega,\ V_g\right)}{I_0(\hbar\omega)} - \frac{I(\hbar\omega,\ 0V)}{I_0(\hbar\omega)}}{\frac{I(\hbar\omega,\ 0V)}{I_0(\hbar\omega)}}.$$

Here $I_0(\hbar\omega)$ is the intensity of the incident light. Since $I\left(\hbar\omega,\ V_g\right)/I_0(\hbar\omega) = 1 - \alpha\left(\hbar\omega,\ V_g\right)$, we get:

$$M = \frac{\alpha(\hbar\omega,\ 0V) - \alpha\left(\hbar\omega,\ V_g\right)}{1 - \alpha(\hbar\omega, 0V)}.$$

Since MoS_2 absorption is small (~5%) in our wavelength region, $M \approx \alpha(\hbar\omega,\ 0V) - \alpha\left(\hbar\omega,\ V_g\right)$ or $\alpha\left(\hbar\omega,\ V_g\right) = \alpha\left(\hbar\omega,\ V_g = 0V\right) - M\left(\hbar\omega,\ V_g\right)$. Therefore, we can estimate $\alpha\left(\hbar\omega,\ V_g\right)$ from measured M and $\alpha\left(\hbar\omega,\ V_g = 0V\right)$~5% obtained from an unbiased MoS_2 flake before deposition of solid electrolyte.

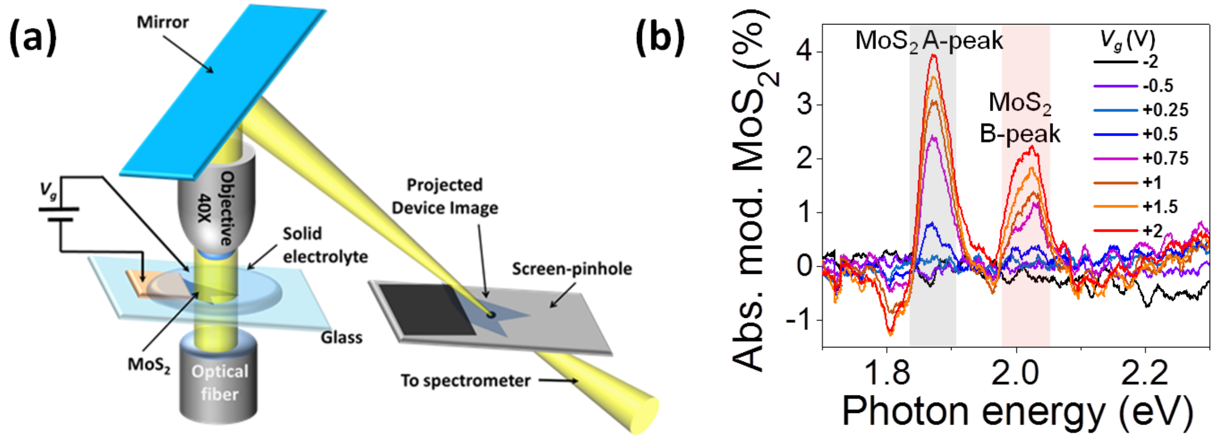

Figure 5.5 (a) *Schematic of measurement set up for transmission microscopy. (b) Transmittance modulation of* MoS_2*. The dip at ~1.8eV is likely related to charged exciton absorption.*

Within our gating range we observe only ~2% modulation of MoS_2 transmittance at ~2.05eV (Fig. 5.5b), much smaller than ~75% modulation in QD photoluminescence (Fig. 5.4).

The measured $Q(\alpha)$ along with the prediction of equation (3) (dashed line) are plotted in Fig. 5.6a. The agreement between the experimental data for (V_g>0) and our model confirms that the observed modulation of QD photoluminescence is a consequence of electrical modulation of FRET. However, interpretation of $Q(\alpha)$ data is complicated by the difference of the intrinsic doping levels of MoS_2 between QD/MoS_2 and MoS_2-only devices. Indeed, at $V_g=0$ we observed reduced PL due to MoS_2 (peak at ~1.9eV) in QD/MoS_2 as compared to MoS_2-only devices (Fig. 5.6b). Since PL of MoS_2 can be used as a proxy for free carrier density, this observation suggests that the intrinsic doping level of MoS_2 in MoS_2-only devices is *lower* than that of MoS_2 in QD/MoS_2 devices. Moreover, the observation of near-absent absorption modulation for MoS_2 in MoS_2-only devices (Fig. 5.5b) for V_g<0 (as compared to strong absorption modulation for V_g>0) suggests that the density of free carriers in that device approaches ~0 at V_g=0 (Fig. 5.4c). In contrast, robust changes of MoS_2 and QD photoluminescence in QD/MoS_2 devices (Fig. 5.4) hint

that the density of free carriers is changing throughout our gating range and the Fermi level always stays within the conduction band. In Fig.5.6c, we illustrated the proposed Fermi level positioning between MoS_2 and QD/MoS_2 devices due to difference in intrinsic doping levels.

Because of the difference in the intrinsic doping levels, we have to be careful in relating the experimentally measured α_{MoS_2} to the analysis of QD/MoS_2 devices. For V_g>0, the Fermi level of MoS_2 in both MoS_2-only and QD/MoS_2 devices is in the conduction band and the absorption of MoS_2 in both devices changes similarly. On the other hand, when V_g<0, the Fermi level of MoS_2 in MoS_2-only devices is shifted below the conduction band edge. In that case, the density of free carriers and hence α_{MoS_2} are nearly V_g-independent (Fig. 5.6). At the same time, the absorption of MoS_2 in QD/MoS_2 devices strongly changes with V_g. This means α_{MoS_2} in QD/MoS_2 and MoS_2-only devices are only close when V_g>0.

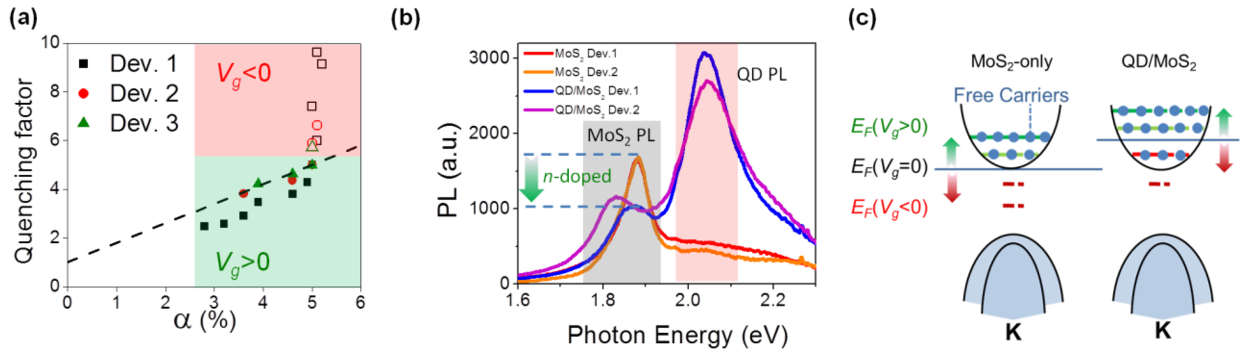

Figure 5.6 ***(a)*** *Q(α) plot including the data for 0<V_g<0.* ***(b)*** *Photoluminescence spectra of two different MoS_2-only devices without QDs, and of two different QD/MoS_2 devices. (**c**) Proposed Fermi level (E_F) positioning of MoS_2 in MoS_2-only and QD/MoS_2 devices.*

5.6 Elucidating Mechanism of QD PL Modulation

We confirmed that mechanisms other than FRET are not responsible for observed changes in PL in our devices. In principle, charge transfer between QDs and MoS_2 can also lead to non-radiative relaxation [68-70]. For our experiments we intentionally chose core-shell QDs with strong electron-hole pair confinement and long ligands [71]. Charge transfer in such core-shell QDs is likely inefficient or absent [72]. To further exclude the contribution of charge transfer, we fabricated devices with a spacer layer (5-15nm of SiO_2) inserted between QDs and MoS_2. Despite large MoS_2/QD separation, we observed significant quenching in PL of QDs atop of MoS_2 (Fig. 5.7c). Such quenching can only be attributed to long-range FRET, as short-range charge transfer should be fully suppressed in spacer devices [73]. It is also feasible that dielectric screening due to MoS_2 could affect the intensity of QD photoluminescence. To exclude this possibility, we fabricated devices where hBN, an optically transparent insulator, is transferred onto QDs instead of MoS_2 (Fig. 5.8d). While hBN has a dielectric constant $\varepsilon \sim 4–7$, [74] similar to that of monolayer MoS_2,[75] we did not observe any spectral changes or quenching for QDs in hBN/QD devices. This confirms that the QDs are not affected by dielectric screening due to neighboring materials. This also rules out the possibility of mechanical or chemical changes to the QD layer during the transfer procedure.

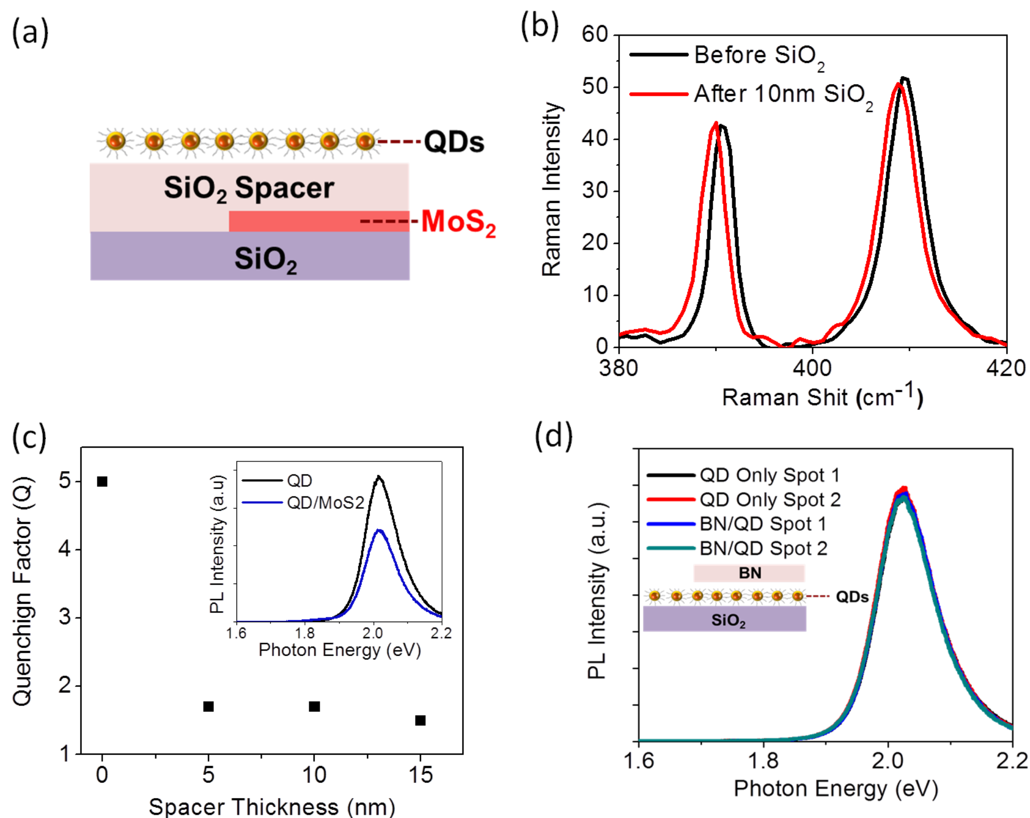

Figure 5.7 ***(a)*** *Device schematic for MoS_2/spacer/QD device.* ***(b)*** *Raman spectra of MoS_2 before (black) and after (red) SiO_2 spacer deposition.* ***(c)*** *QD quenching factor vs. spacer thickness. Inset: PL spectra of QD and QD/MoS_2 for 15nm spacer device.* ***(d)*** *Photoluminescence spectra for QDs covered by hBN (blue and green curves) and QDs away from hBN (black and red curves). Inset: schematic of a hBN/QD device.*

5.7 Spectral Selectivity of FRET

To further check possible contribution of charge transfer to QD photoluminescence modulation in QD/MoS_2, two additional types of devices were fabricated. In the first type of device Fig. 5.8a we used CdSSe QD with the emission peak at ~2.2eV (away from the excitonic absorption peak of MoS_2) to make hybrid QD/MoS_2 devices. In the second type of device Fig. 5.8b, same QDs as discussed in previous sections (emission peak at 2.02eV) were used, but MoS_2 was substituted by monolayer graphene. In both devices, optical absorption of the 2D

material was constant at relevant QD emission energies. PL spectra were recorded while varying the gate voltage V_g for both QD/MoS_2 and QD/graphene devices (Fig. 5.8a,b). In both cases, we observed no changes in the PL at the emission wavelength of the QDs (2.2 eV in (a) and 2.02eV in (b)). This further indicates that electrical modulation of the PL for the QDs is due to changes in excitonic absorption of MoS_2 and not just due to changes in its carrier density.

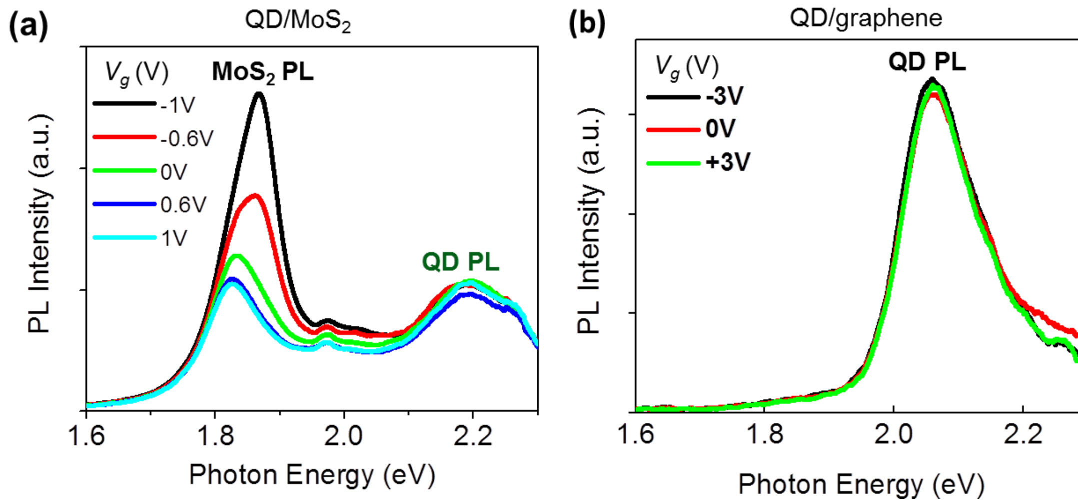

Figure 5.8 ***(a)*** *QD/MoS_2 gated device with QDs in resonance with MoS_2 B-peak* ***(b)*** *QD/graphene device with same QDs highlighting how QD PL is not affected by change in carrier density of 2D material on top*

We conducted additional experiments to demnonstrate that QDs can be modulated with spectral selectively. Below, we present the experimental evidence that **green** QDs (2.4eV) can be selectively modulated by using 2D semiconductor WS_2 (A-peak: 2.0eV, B-peak: 2.4eV)[76]. We find that the photoluminescence intensity of the QDs is only modulated *when their emission spectrum overlaps with the peak in excitonic absorption of a 2D semiconductor*. The PL of green QDs is modulated when they are underneath WS_2 (Fig. 5.9a) but not underneath MoS_2 (Fig. 5.9b).

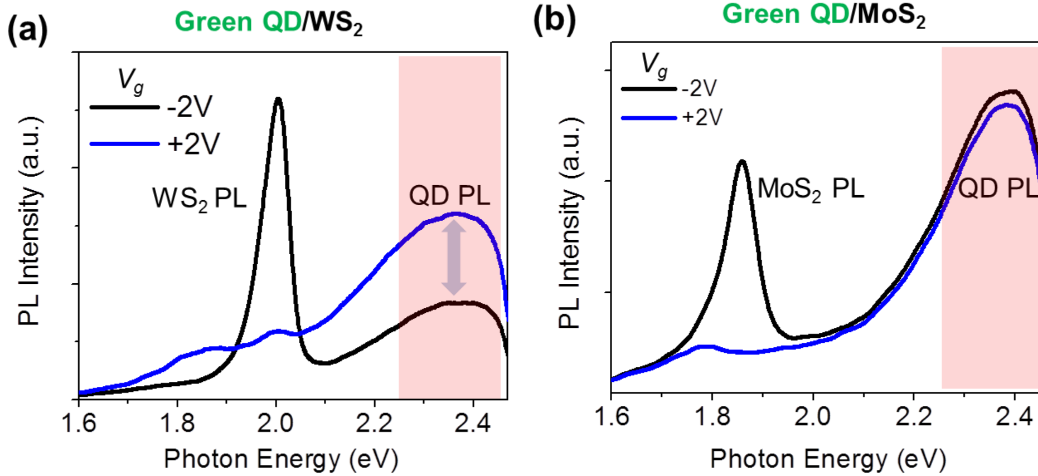

Figure 5.9 ***(a)*** *Green QD/WS$_2$ gated device showing modulation of green QDs which are in resonance with WS$_2$B B-peak* ***(b)*** *Same QDs are not modulated by MoS$_2$*

5.8 Conclusion and future work

In summary, we demonstrated electrical control of the near-field energy transfer between QDs and 2D semiconductors (MoS_2, WS_2). We found that it is related to modulation of excitonic absorption of 2D semiconductors, and achieved ~75% modulation of QD photoluminescence in the visible range. It is instructive to compare our approach to other existing schemes to control photoluminescence of QDs via electrical signals. Some of the existing schemes utilize electrochemical injection of charge carriers into QDs,[69, 70] electron-hole dissociation under applied electric fields,[77] or controlled Stark shifts [78]. In all of these schemes, electrical fields are applied directly to the QDs. In our approach the electric field changes the parameters of a 2D semiconductor and is absent at the location of QDs.[65] We do not expect electrochemical modification of QDs. The operating principle of our scheme – electrical control over the QD/2DSC FRET rate – can be extended to other nanoemitters. Finally, QDs emitting at different wavelengths over the visible and IR ranges can be modulated by choosing 2D semiconductors with varied bandgaps (e.g.: WSe_2, WS_2, $MoSe_2$).

We envision several potential improvements in our system. FRET efficiency, and hence the efficiency of PL modulation, can be increased by reducing the distance between QDs and 2DSCs (equations (1) and (3)). This can be achieved by either reducing QD shell-size or by shortening QD ligands. Additionally, 2DSCs could be gated more efficiently using ultrathin gate dielectrics. The advances in CVD growth[79, 80] of 2DSCs could lead to inexpensive fabrication of large-scale QD/2DSC hybrids. Overall, QD/2DSCs hybrids could be used as efficient and electrically tunable light sources operating anywhere in the visible to IR spectral range. Potential applications for such devices range from solid-state lighting and high-resolution passive ("e-ink") displays to biosensors.

CHAPTER 6: FUTURE DIRECTIONS AND CONCLUSION

6.1 Thesis summary

In this thesis, we demonstrated the potential uses of MoS_2 in both electronic and optoelectronic devices. We investigated the extrinsic scattering mechanism in n-type MoS_2 field effect transistors (FET) and explained the clarified role of electrical contacts and phonons to carrier mobility. We also investigated device structures to reduce scattering from impurities from the substrate. These findings may help in designing better MoS_2-FETs to complement current CMOS-based technology. With advancement in growth techniques, we could imagine the development and integration of future electronics completely based on 2D materials (channel: $MoS_{2,}$ contacts: graphene, dielectric: boron nitride).

We investigated the interaction of free charge carriers interact with excitons in MoS_2. We demonstrated strong tunability of the optical properties (absorption/photoluminescence) of MoS_2. We also examined near-field energy transfer between MoS_2 and quantum dots for possible hybrid optoelectronic applications. We demonstrated the ability to tune the rate of energy transfer between QDs and electrostatically gated MoS_2. We showed this effect to applicable to any nano-emitters which are in resonance with the excitonic features of monolayer TMDCs.

In the remaining part of this thesis, we discuss ongoing projects to study new approaches towards tailoring the optical properties of TMDCs and exploring new phenomenon in these materials.

6.2 Future directions: bandgap engineering in MoS_2 via vertical electrical fields

Multiple research groups have explored the use of TMDC materials for number of materials efficient photodetectors and electroluminescent devices [81-84]. Unfortunately, the limited TMDC family (MX_2, M = Mo, W; X = S, Se, Te) only allows access to limited number

of absorption bands values throughout the visible spectrum. Bandgap engineering via perpendicular electric fields could prove to be a very critical step towards tailoring the optical properties of TMDCs and making devices operating in the near and mid-IR range. This could also lead towards making photodetectors with desirable wavelength sensitivity. The Shockley-Queisser theory give predictions that semiconductors with a direct band gap near ~1.3eV and high mobility can lead to more efficient photovoltaics (Fig. 6.1a) [18]. Monolayer-TMDCs falls just above the Shockley-Queisser limit (Fig. 6.1a). Bandgap engineering can open up the possibility of using TMDCs for highly efficient photovoltaic devices. Bandgap engineering could enable multi-junction semiconductor devices with varying bandgaps to absorb a large party of the solar spectrum (Fig. 6.1b). Concept devices based on straining TMDCs have been proposed to recognize broad spectrum solar energy funnels [85, 86] (Fig. 6.1c).

It is therefore desirable to have a tunable bandgap that would allow for flexibility in device applications and optimization. Fortunately, the band gaps in TMDCs have the added benefit of being strongly tunable. For example, the bandgap of 2D semiconductors have been shown to be dependent on applied mechanical strain [85]. In this chapter, we investigate a different approach to control the bandgap of TMDCs – by applying perpendicular electrical field. Such an approach has been shown to work for bilayer graphene [12]. In that case, an electric field normal to the sheet of graphene breaks the inversion symmetry and opens up a bandgap up to 250meV [87]. Similarly, a perpendicular electric field applied to bilayer MoS_2 can redistribute charge density in the bilayers to the atomic planes and also delocalizes them within the planes [88] causing a decrease in the bandgap. Several theoretical studies have demonstrated that a similar approach can be used to modify the bandgap in TMDCs from optical energies (~2eV) all the way to zero [88, 89].

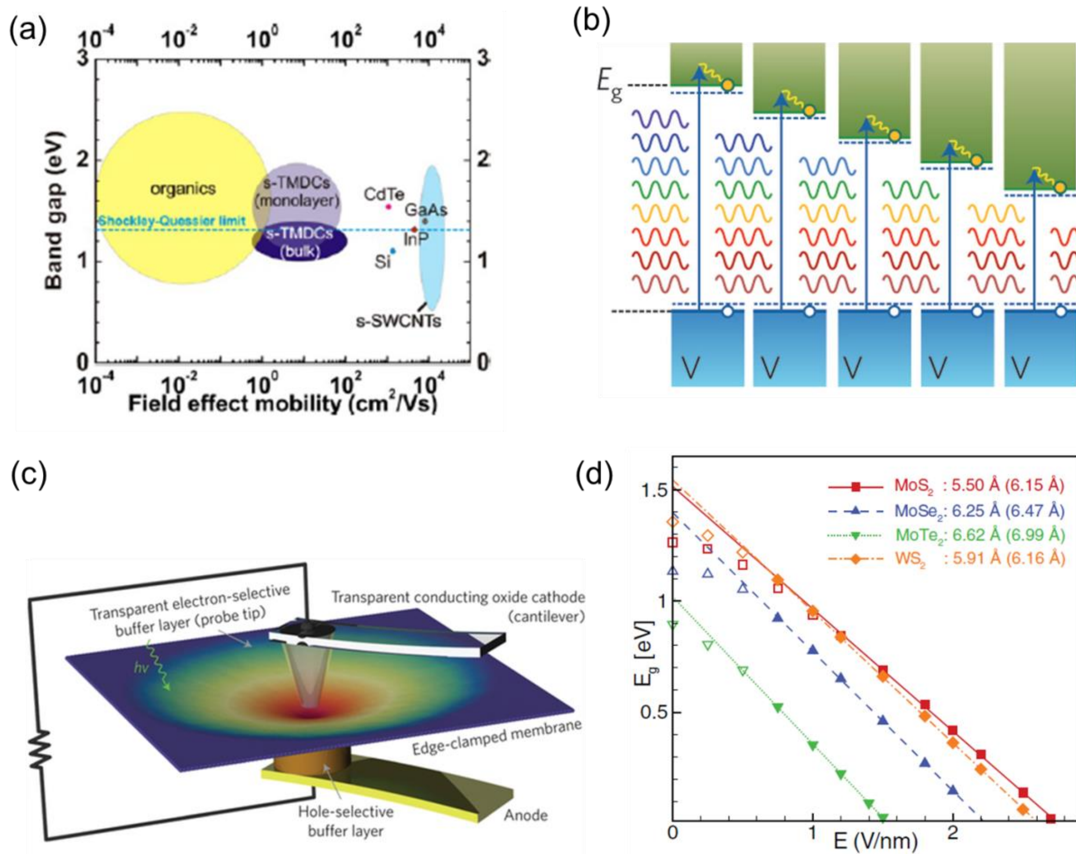

Figure 6.1 ***(a)*** *Band gap versus mobility for various materials used in current photovoltaic technologies. Semiconductors with high mobility and bandgap near Shockley-Quessier limit (1.3eV) are desired for more efficient photovoltaic devices. TMDC compare favorably to other materials. Bandgap engineering of TMDCs could further enhance the performance of solar cells based on TMDCs. Figure acquired from reference [18]* ***(b)*** *Schematic for multi-junction semiconductor solar cell designed to absorb larger part of the solar spectrum. Such device structures can potentially be achieved by using TMDCs with graded bandgaps. Figure acquired from reference [90]* ***(c)*** *Schematic of strain engineered* MoS_2 *device allowing capture of photons of different energies and guidance of concentrated charge carriers towards contacts. Figure acquired from reference [86] Bandgap versus applied electric field for bilayer TMDCs. Figure acquired from reference [87]*

6.3 Towards bandgap engineering in MoS_2: device geometries

In this section we present details of our ongoing approach to engineer the bandgap in bilayer MoS_2. Our goal is to explore various device geometries which would allow us to probe changes in MoS_2 bandgap vs. applying a perpendicular field. In a typical device, bilayer MoS_2 is sandwiched between two parallel electrodes. Electric field is applied between the two electrodes and allowing us to probe changes in the bandgap by measuring the photoluminescence spectra of MoS_2 *versus* applied field. For this device structure to work, one of the two-parallel electrodes needs to be transparent to optically excite and measure changes in of the photoluminescence spectrum of bilayer MoS_2. We also have to ensure that the two parallel electrodes do not come into contact. For this reason we encapsulate bilayer-MoS_2 between boron nitride flakes using transfer techniques described in Appendix:A6. MoS_2 sandwiched between Boron Nitride would then be transferred onto Au electrodes. Finally, a transparent electrode would be deposited atop the Au/BN/MoS_2/BN structure (Fig. 7.2d). Due to the high breakdown voltage of BN, we expect to reach fields as high as 1V/nm for ~10nm thick BN[91]. According to theoretical calculations, this could lead to ~500meV changes in the bandgap of bilayer MoS_2 [88](Fig. 6.1d).

The next challenge is to incorporate a transparent top electrode into our device structure. We first explored using indium tin oxide (ITO) due to its high conductance, good adhesion to substrates and high transmittance across relevant frequencies (1.5-4eV). We explored the transmittance of 50nm ITO films prepared through e-beam deposition [92]. We realized that ITO films prepared through such techniques are initially amorphous and fairly opaque. Annealing in ambient conditions changes amorphous ITO into a crystalline structure and increases its transmittance. The transmittance spectra of such prepared films before and after annealing are shown in Fig. 6.2a. Unfortunately, we later had difficulties trying to make Au electrical contacts

to ITO and realized the Au/ITO interface deteriorates severely during the ITO annealing step (Fig. 7.2b). Due to the complications with Au/ITO interface we are also exploring alternative transparent top gates. Thin layers of graphene are ideal as a top electrode since for optical energies >0.5eV graphene has a near constant absorbance (~2.3%) [93, 94]. We are currently developing transfer techniques to make multi-layer heterostructures to realize devices shown in Fig. 6.2d.

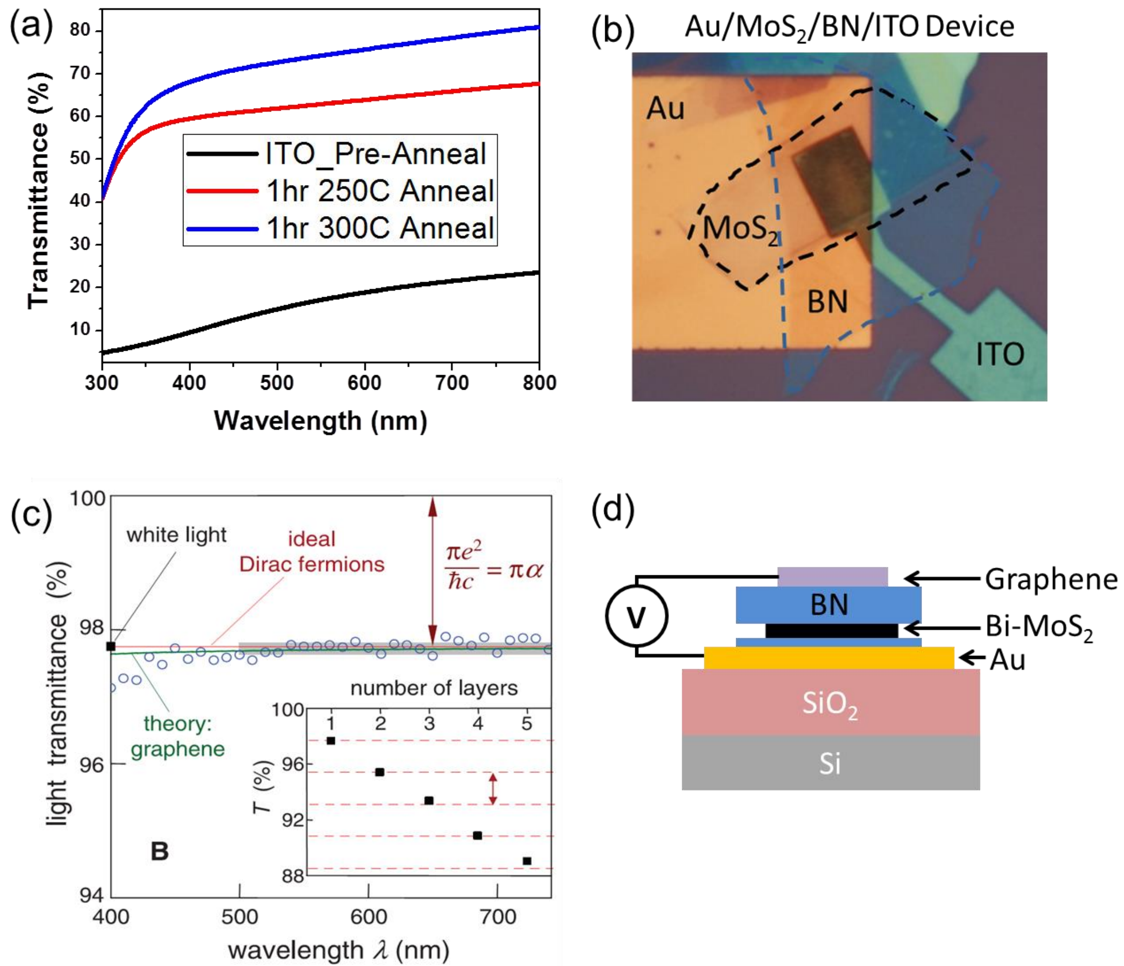

Figure 6.2 ***(a)*** *Transmittance of 50nm ITO films prepared through e-beam evaporation.* ***(b)*** *Au/bilayer MoS_2/BN/ITO devices. Optical image highlights damaged ITO at Au/ITO interface.* ***(c)*** *Transmittance of graphene. Figure acquired from reference [94]* ***(d)*** *Proposed device schematic for applying vertical electrical fields through bilayer MoS_2 using graphene as a top transparent electrode.*

6.4 Many body effects in TMDCs at high carrier density

As discussed in chapter 4, tightly bound excitons in MoS_2 strongly interact with gate-induced charge carriers. These strong interactions modify photoluminescence and absorption properties of monolayer TMDCs. Optical spectroscopy (photoluminescence/absorption) of monolayer TMDCS can therefore be used as an efficient tool to comprehensively study many-body phenomena such as trions, bound excitons and biexcitons. Electrostatic gating has already been used to demonstrate the formation of trions in monolayer TMDCs [48, 49]. However, the maximum carrier density achievable in such devices is limited due to the breakdown of SiO_2 at high fields. Here, we explore what happens to excitons/trions in TMDCs at very high charge carrier densities ($>10^{13}cm^{-2}$) induced through ionic gating.

Previous studies of trions in TMDC have reported binding energies to be ~20meV. Low temperature is therefore required to spectrally identify trions. We chose to study monolayer WS_2 based FETs due to the stability of trions in this material at room temperature. The trion binding energy ~30meV ($\sim X_0(eV) - X^-(eV)$, Fig. 6.3a) in our Si backgated WS_2-FETs is clearly distinguishable at room temperatures. We observe drastic changes in the PL spectra (Fig. 6.3b,c) at high carrier densities induced using solid electrolyte gating. We observe the emergence of a third peak below the trion peak at 1.95eV (labeled X^B, shaded region in Fig. 6.3b,c). This X^B peak shifts as far as ~200meV below the neutral exciton (Fig. 6.3d).

At the first glance this peak may be caused by defect-bound states previously observed in thermally annealed or α-particle irradiated devices [95]. Optically excited excitons are then bound to such defects and recombine radiatively at emission energies lower than the band-to-band optical transition energy. However, we can rule out since the X^B peak disappears upon

reversing the polarity of gate voltage. Therefore, no defects were created during the gating process.

What is the origin of this peak? We are currently carrying out sensitive low temperature spectroscopies to identify its origins. We suspect that it may be associated with a novel many body state of MoS_2. It could be due to formation of electron-hole droplets, a liquid phase of excitons, which have been observed for high exciton densities in Si and Ge [26].

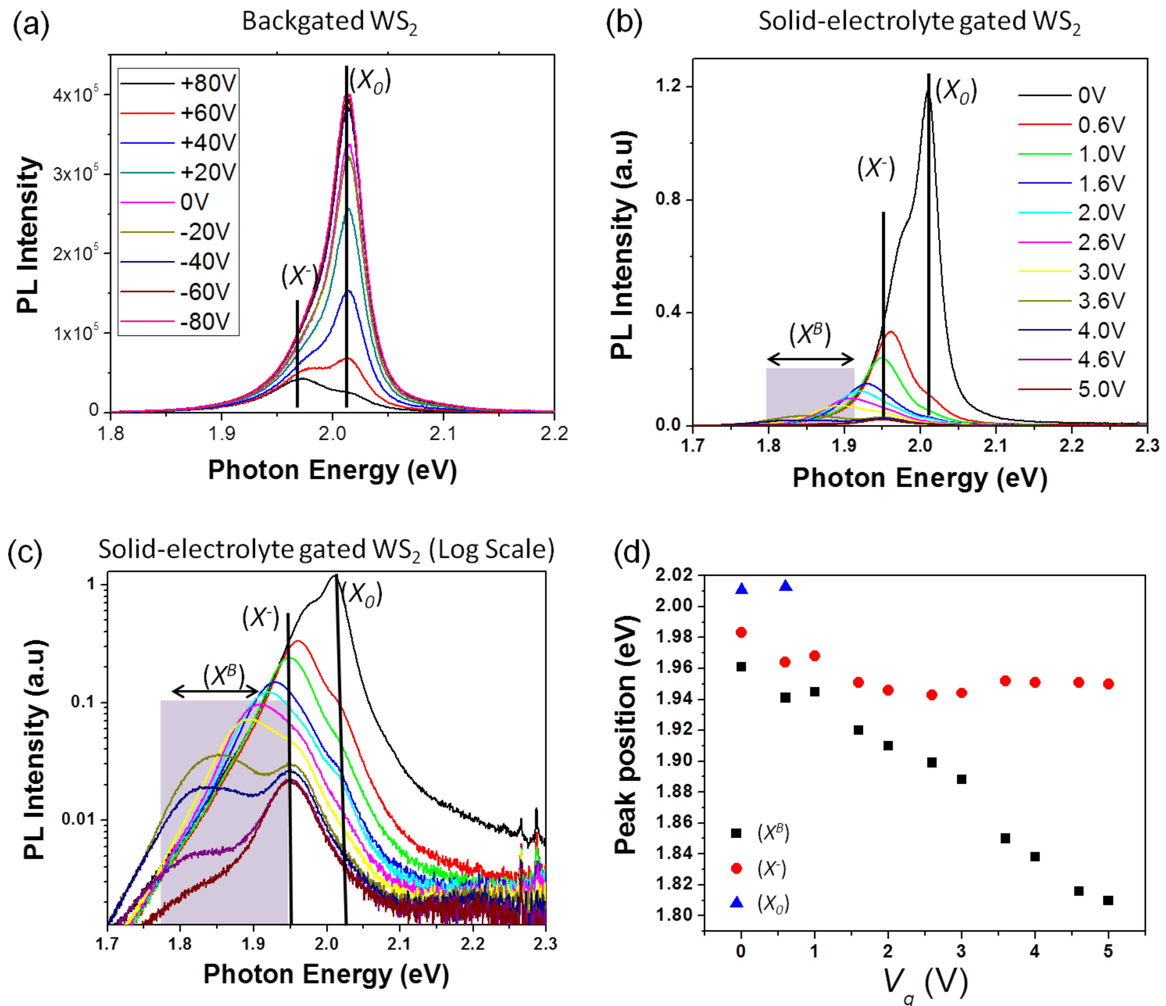

Figure 6.3 ***(a)*** *PL spectra of monolayer* WS_2 *vs. backgate.* X_0 *denotes the peak due to neutral band edge excitons while* X^- *denotes due to negatively charged trion peak.* ***(b)*** *PL spectra of ionically gated*

*monolayer WS_2 device. The evolution of the X^- into a new quasi state X^B is evident **(c)** PL spectra of ionically gated monolayer WS_2 device plotted in log scale to elucidate the evolution of X^B at energies lower than trion peak <1.95eV. **(d)** Peak position vs. gate voltage (upon electrolyte gating). Peak positions acquired using Gaussian fits. All data taken at room temperature.*

6.5 Conclusion

The findings presented in this thesis work are crucial for design and implementation of optoelectronic devices based on TMDCs. It is vital to identify scattering mechanisms in TMDC devices to probe the intrinsic electronic properties and realize device potential of this material. Similarly, understanding electron-exciton interaction is vital for understanding exciton physics in 2D systems and designing optoelectronic devices based on monolayer-TMDCs.

The major challenge for TMDC-based optoelectronic devices is to devise techniques to enhance light absorption and increase fluorescence quantum yields to compete with conventional semiconductors [16, 18]. Advancement in growth and high quality sample preparations could also expedite the use of TMDC in flexible electronics.

APPENDIX

Fabrication and Characterization

A1. Mechanical Exfoliation

In the exfoliation process, a small piece of HOPG is placed on a piece of scotch tape. The piece is then folded onto itself and ripped apart to separate layers in HOPG. This is done several times until thin layers are formed uniformly across the tape. Finally, the tape is placed on top of a SiO_2/Si and a pair of Teflon tweezers is used to gently push down the flakes onto the SiO_2 surface. Upon slow removal of the tape, monolayer flakes are dispersed randomly across the substrate. It is essential to have the right thickness of SiO_2 to be able to locate the monolayer flakes. Several studies have been conducted using Fresnel theory to maximize the contrast between the thin flakes of graphene and the underlying oxide layer.[96] Studies have shown that 300nm is a good oxide thickness to maximize contrast between the monolayer and the substrate. Similarly, single layers of MoS_2 can be extracted from the mineral Molybdenite as shown in Fig. A1 a, b, c.

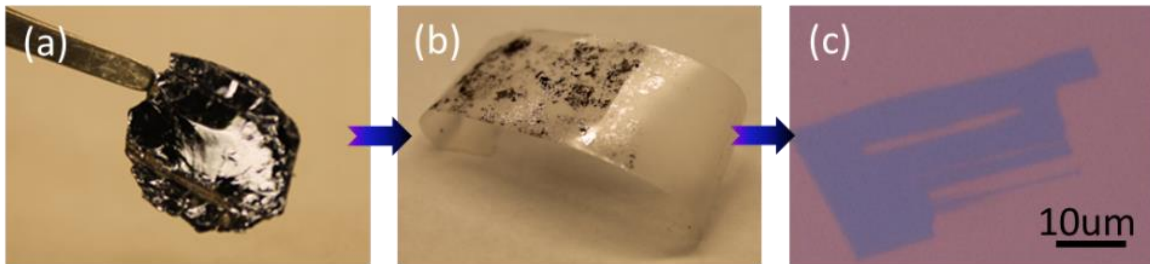

Figure A1 *(a) Molybdenite (b) Exfoliation of MoS_2 on Scotch tape. (d) Monolayer MoS_2 on Sio_2/Si*

A2. Raman Characterization

Raman spectroscopy is a non-destructive useful tool that can provide detailed structural and electronic information regarding 2D materials. It measures the energy shift of incident laser photons due to inelastic scattering with phonon vibrations in material's lattice. Raman spectroscopy is currently the common standard used by different groups to compare the quality of graphene.[97-99]

The Raman spectra of graphene and graphite are shown in Fig. A2b. Two characteristic peaks are observed at ~1580cm^{-1} (G) and ~2700cm^{-1} (2D). There is also a D peak at ~1350cm^{-1}, which is not visible in the figure. The D peak arises due to the carbon ring breathing mode (Fig. A2.a) and is activated due to defects in the graphene lattice. The 2D peak in graphene comes from two phonons with opposite momentum in the highest optical branch near the K point. This 2D peak is very sensitive to the number of graphene layers as can be seen in Fig. A2c. The 2D peak of graphene is considerably different than that of graphite and is about four times stronger than the G peak. This sensitivity and the shape of the 2D peak can be used to distinguish between single, bi-, and multi-layer graphene. Once the number of layers is higher than 5, the 2D peak resembles that of bulk graphite.

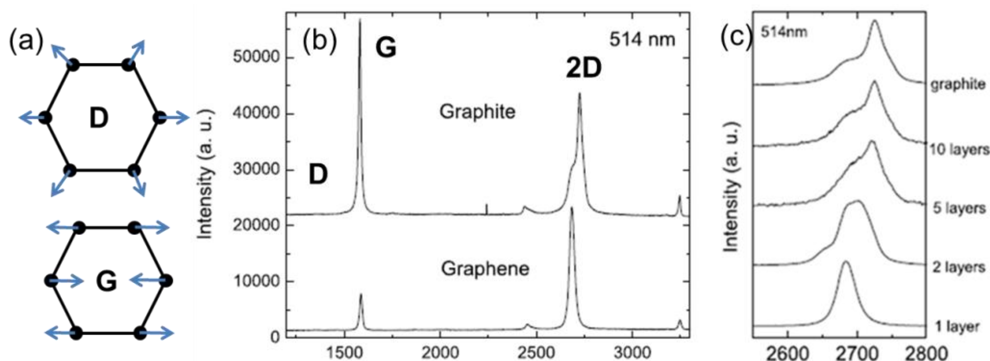

Figure A2 *(a) Phonon modes in Graphene. (b) Raman spectrum of graphene and graphite. (c) Evolution of 2D peak with number of graphene layers. Figure acquired from reference [97]*

Similarly, using Raman spectroscopy, we can also probe in-plane and out-of-plane phonon modes in MoS_2. These modes in MoS_2 show thickness dependence and the two modes start separating from one another in frequency with increasing layer number (Fig. A3b). Single-layer MoS_2 displays a strong in-plane vibrational mode ~384 cm^{-1} corresponding to the in-plane E^1_{2g} mode and an out-of-plane A_{1g} at ~404 cm^{-1} (Fig. A3a) [100, 101].

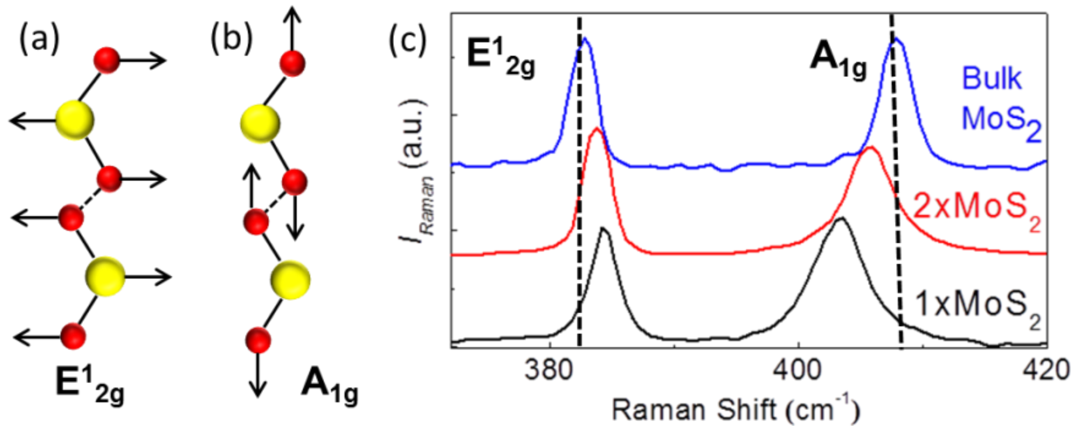

Figure A3 *(a) In-plane phonon mode. (b) Out-of-plane phonon mode. (c) Raman spectra of* MoS_2 *of various thicknesses.*

A3. Chemical Vapor Deposition Growth

i) Monolayer graphene growth

We grow graphene on copper (Cu) using the well-established recipes that yield high-quality, predominantly single layer graphene [102, 103]. 25 µm thick Cu foils are cut into small strips and placed inside a fused silica tube and heated using a hot wall furnace. The Cu foil is first heated at 1000°C under a 2 sccm flow of hydrogen while being simultaneously evacuated and filled. This is done to remove any contaminants and native oxide from the Cu surface. The pressure at the time of annealing is maintained close to 25 mTorr. Then 35 sccm of CH_4 (g) is

introduced along with the 2sccm of H_2 for 30 minutes (pressure maintained at ~250 mTorr), after which the furnace is slowly cooled to room temperature. A schematic of the growth system is shown in Fig. A4a. The growth process involves the decomposition of CH_4 over a copper substrate at 1000°C. Pre-treatment (annealing in H_2) of the Cu foil is deemed essential to remove native oxides such as CuO and Cu_2O which affects the catalytic activity as well as increases Cu grain size. This facilitates graphene growth. Effects of growth time on graphene nucleation are shown on Fig. A5 b,c,d.[103] After the growth procedure, we obtain a monolayer film of graphene on both sides of the Cu foil (Gr/Cu). The growth process is self-limiting and the film is predominantly monolayer.

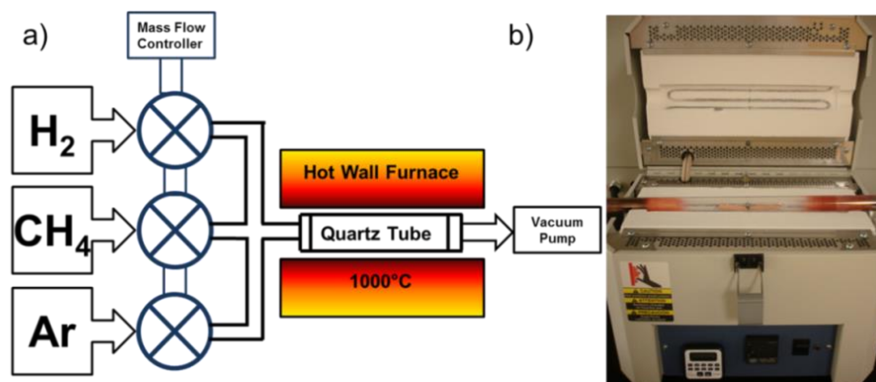

Figure A4 *(a) Schematic of CVD Growth System. Mass flow controller is used to control gas flow while a vacuum pump is used to evacuate the quartz tube (b) CVD Furnace with 25um thick Cu foils placed inside Quartz tube prior to growth.*

One significant difference between the graphene produced through CVD growth and the one obtained through mechanical exfoliation is that CVD graphene is a polycrystalline material. The properties of polycrystalline materials are dependent on the size and structure of the grain boundaries. The crystallinity significantly influences the properties of a 2D material such as

graphene. A lot of recent work suggests that the deposition parameters have little effect on the electrical and physical properties of as-grown graphene on Cu.

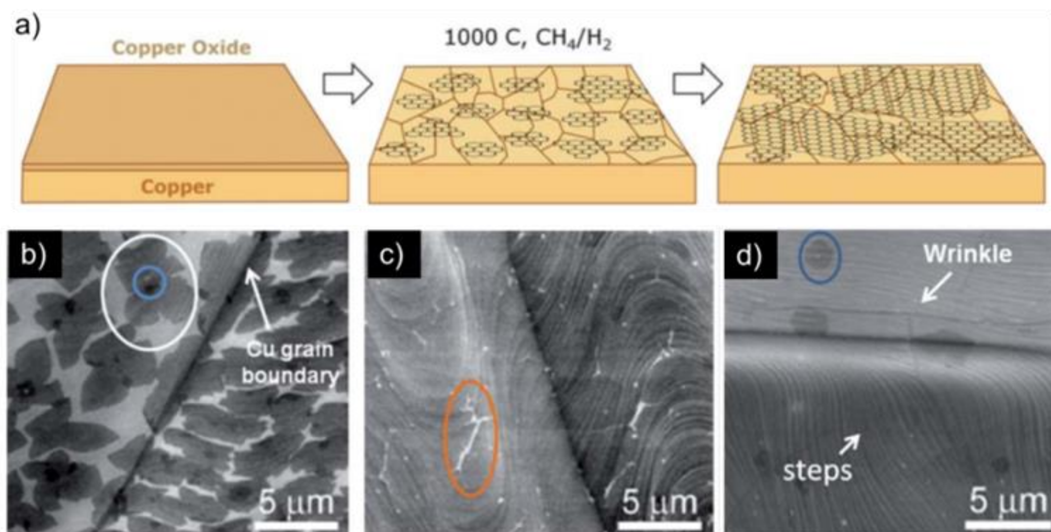

Figure A5 *(a) Schematic showing the 3 stages of graphene growth on Cu. (Cu with native oxide-nucleation of graphene islands – enlargement of graphene flakes). Scanning electron microscopy images of graphene on Cu for different growth times (b=1min, c=2.5min, d=10min). (b) Circles represent the nucleation site and graphene domain (c) Continuous graphene layer and blue circle representing small overlap causing bilayer formation. Figure acquired from reference [103].*

ii) 3D graphene growth

Recently developed [104] three-dimensional graphene foams (3DGFs) have been used in various applications such as battery technology[87] and electrochemical sensing[105]. In collaboration with the Hak-Joon Sun biomedical engineering group at Vanderbilt University, we studied 3DGFs as cell culture substrates for mesenchymal stem cells [106]. For such experiments we fabricated free-standing graphene foams through chemical vapor deposition under ambient pressure. Graphene was grown on a 3D nickel scaffold, allowing for the growth of an interconnected scaffold of 3D graphene according to a previous protocol [104]. Ni foams with a

thickness of 1.2 mm and 320 gm^{-2} areal density were purchased from Alantum Advanced Technology Materials (Shanghai, China). The nickel foams were cut into small pieces and placed inside a 25 mm quartz tube for growth. The foam was initially annealed at 1000℃ under 500 sccm of Ar and 100 sccm of H_2 to remove any contaminants. After annealing, 7 sccm of CH4 was introduced for 5 min which decomposes the CH_4 and deposits carbon atoms on the Ni foam. After growth, Raman microscopy was used to verify the growth of multilayer graphene on the Ni foams. Ni was removed by $FeCl_3$ etching: a drop of PMMA (A7) was placed on top of the freshly grown graphene/Ni hybrid structure and heated on a hotplate at 90 ℃ for 5 min. PMMA provided physical support and stops the graphene layers from collapsing onto themselves upon Ni etching. After Ni was etched, PMMA was removed in an acetone bath. GFs were characterized by SEM, EDX and Raman spectroscopy (Fig. A6).

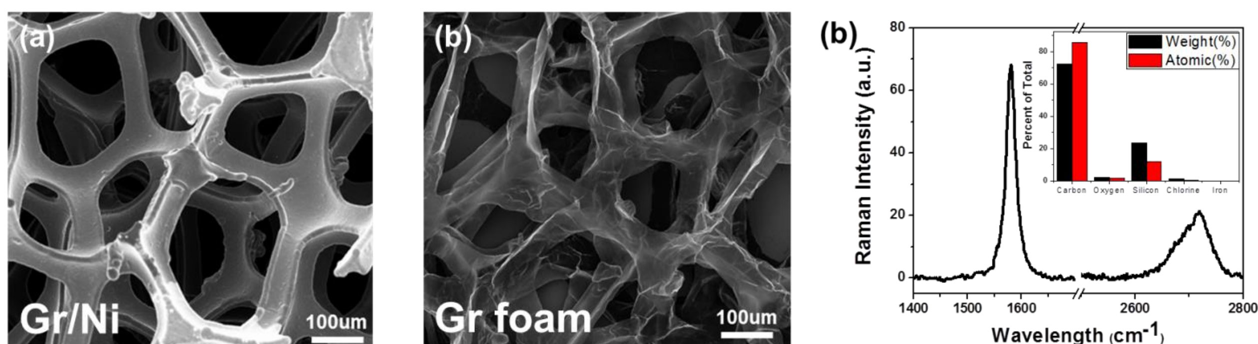

Figure A6 *(a) SEM image of multilayer graphene/Ni scaffolds. Image taken right after growth (b) SEM image of free-standing graphene foam after Ni etching (c) Raman spectra of graphene foams, Inset: EDX of graphene foams on SiO_2/Si substrates reveal that no Ni is detected and scaffolds are completely made out of interconnected graphene layers.*

iii) Monolayer MoS_2 growth

Recent demand for large area monolayers of MoS_2 has also led researchers to synthesizing large area MoS_2 with CVD [80, 107]. Lin *et al*. have developed a recipe that allowed them to use MoO_3 powder and Sulfur powder as precursors to grow MoS_2 directly on SiO_2/Si substrates pretreated by a spin coating of reduced graphene oxide (rGO). The rGO acts as a nucleation site and helps to form the MoS_2 seeds for the growth of MoS_2 films. In the growth process a SiO_2/Si substrate along with the precursors are placed inside the reaction chamber and heated at 650℃ in a nitrogen environment. At this elevated temperature, the MoO_3 is reduced by the sulfur to form volatile suboxide MoO_{3-x}, which diffuses into the substrate, and then reacts further with the sulfur vapor to form MoS_2. Fig. A7b depicts the nature of the nucleation growth on top of rGO/SiO2/Si substrate. Fig. A7c shows a photoluminescence image of as grown monolayer CVD MoS_2.

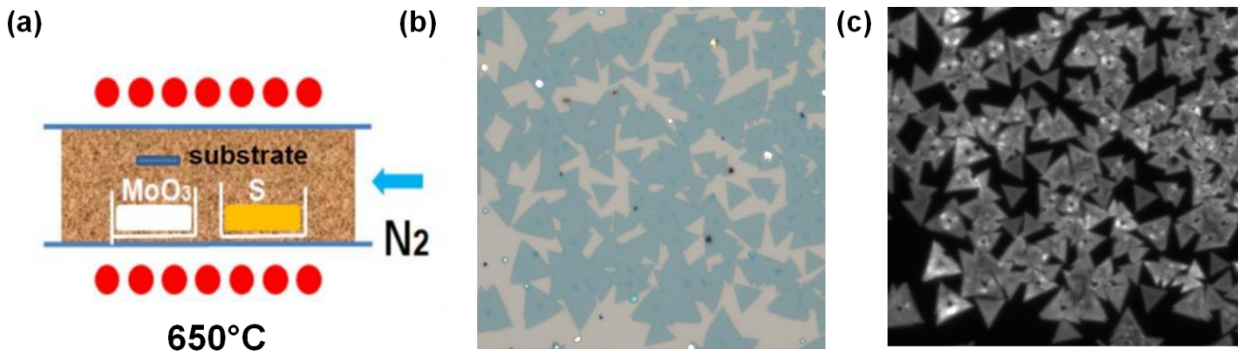

Figure A7 *(a) CVD growth schematic of MoS_2. MoO_3 and S precursors are placed in a ceramic boat along with the target rGO treated SiO2/Si substrates. Figure acquired from reference [80] (b) Optical images of MoS_2 layers grown on SiO_2/Si substrates. (c) PL image of same CVD grown MoS_2.*

A4. Polymer assisted transfer of 2D materials:

After growth the graphene/Cu foils are transferred onto arbitrary substrates using a PMMA mediated transfer technique[108]. The graphene/Cu foil is cut into 1cm x 1cm squares. Thermal release tape (Nitto Denko Revalpha, Semicorp.com, item no. 3198) is attached to the back of the graphene/Cu foil to provide rigidity so that the coil does not crumple during the transfer process. PMMA (A7, 950) is spun on top of the Graphene/Cu foils at 4000 RPM for 45 secs and heated at 100℃ to bake the release the underlying thermal release tape (Fig. A8 a-c). At this point we have a PMMA/graphene/Cu sandwich structure. Cu is then etched using Cu etchant ($FeCl_3$, type CE100, Transene) for ~1 hour. The PMMA/graphene stack is now fished out and placed in several DI-water baths for 15 minutes each until all $FeCl_3$ is washed off. The PMMA/graphene membrane is fished out onto a desired substrate. The sample is left in air to dry out any water droplets that might be trapped at the interface of the substrate and PMMA/graphene film. Once all the water is dried out, a drop of PMMA A4.5 is dropcast on top of the PMMA/graphene film. This aids in slow release of the A7 film from the graphene. Finally, PMMA is removed by placing the sample in a large beaker of Acetone for >3hours.

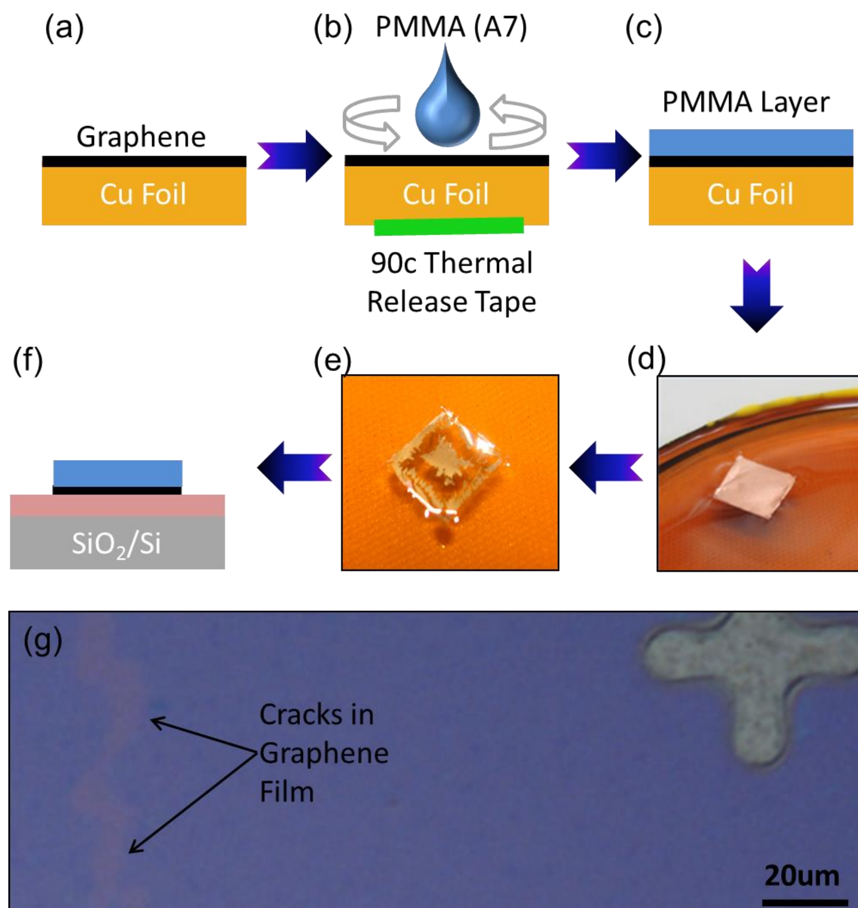

Figure A8 *Schematic illustration of PMMA assisted wet transfer of CVD monolayer graphene. (a)-(c): CVD grown on Cu foil, by spinning on PMMA support deposition of thermal release tape. (d) PMMA/graphene/Cu foil in $FeCl_3$ bath (e) PMMA/graphene and partially etched underlying Cu in $FeCl_3$ (f) Following several DI water baths PMMA/graphene transferred onto SiO_2/Si substrate (g) Large area CVD monolayer graphene on SiO_2 following removal of PMMA in acetone.*

A5. Suspending Monolayer Flakes and Films:

Due to the atomic thickness of both graphene and MoS_2, many researchers have demonstrated that the substrate can have a dominant role on electrical [10, 14] and optical properties of the 2D materials. Through STM and electrical measurements it has been shown that there is a significant amount of charge impurities on SiO_2 [109]. In fact it has been shown that by

etching away the underlying substrate and suspending graphene, its electron mobility can be significantly enhanced [14]. We developed several techniques to suspend graphene and MoS_2 to probe intrinsic material properties free of substrate effects. These techniques are highlighted below:

i. Dry transfer technique

We used this technique to suspend CVD graphene over an array of trenches. Using optical lithography we defined an array of holes 5μm in diameter. We used a combination of BOE etch and RIE in order to fabricate an array of deep trenches on SiO_2/Si substrates. We first coated the SiO_2/Si substrate with ~50nm of Cr. This assists in making deep straight edge walls during the Si etching process. Photolithography was done on AZ5214 photoresist that was developed using TMAH. After developing, the holes in the Cr layer were etched by immersing it in Cr etch (chromium etchant 1020, transene) for 10s. The 300nm of SiO_2 was etched in HF buffered oxide etch (J.T.Baker 50:1) for 20 mins and then rinsed in DI water. Finally, the silicon layer was etched using a fluorine gas based dry RIE process. The photoresist was dissolved in acetone and the remaining Cr layer was etched away for 5 min and thoroughly rinsed in DI-water. In the next step we transferred CVD-grown graphene on top of such trenches. The procedure is very similar to the wet transfer highlighted in the previous section. However, in this process a thin (50nm) membrane of PMMA (950, A2) is spun (4000 RPM, 45s) onto graphene/Cu films. The Cu foil was etched away as described earlier. Once the PMMA/graphene is transferred onto our array of trenches, the PMMA is removed through annealing at 300℃ for 2 hours.[110] The results are shown in Fig. A9 b, c. SEM images clearly show an array of four holes where 3 of them are covered with monolayer CVD graphene. A magnified SEM image of such a membrane shows monolayer graphene suspended over a 5μm hole.

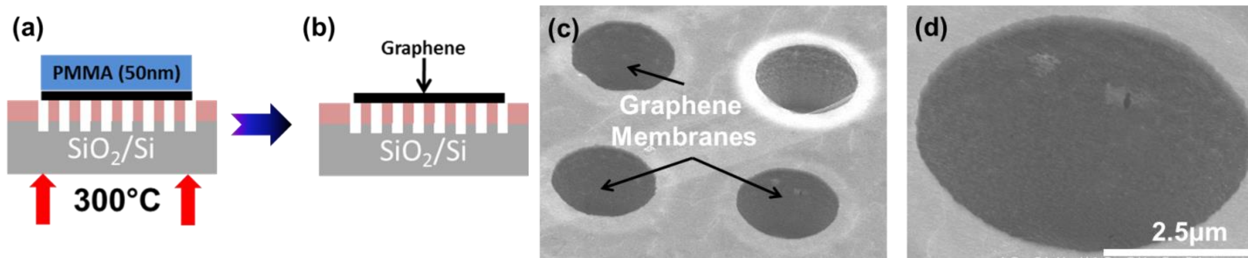

Figure A9 (a) Transfer of thin PMMA/graphene membrane onto an array of trenches on SiO_2/Si (b) Schematic of graphene film suspended across an array of trenches (c) SEM image of as prepared array of graphene membranes (d) Magnified SEM image of a suspended graphene membrane.

ii. BOE and Critical Point Drying (CPD)

In the process discussed above, graphene was transferred onto pre-prepared trenches. In this process suspension of graphene or MoS_2 was accomplished by first exfoliating monolayers of either MoS_2 or graphene from their bulk counterparts (Molybdenite or Graphite). The exfoliated monolayers were then clamped onto the SiO_2 by patterning metal electrodes using e-beam lithography followed by thermal evaporation of Cr (2nm)/Au (90nm). The suspension of the monolayer is accomplished by etching away ~200nm of the underlying SiO_2. The sample is placed in 50:1 BOE for 18 min followed by several rinses in deionized (DI) water baths for 5 min each. Now that the underlying substrate is etched away, the next step is to dry the sample without damaging the suspending monolayer flake/film. If we just take the sample out of water and allow it to dry in air then surface tension of the water would rip apart the now suspended flake. The presence of water molecules can also have detrimental effects in transport measurements. To preserve our suspended flake we have to take advantage of the continuity of state known as the critical point where there is no physical difference between the gaseous and liquid state, reducing surface tension to zero. Unfortunately the critical point of water is ~374℃ and 229 bar which is inconvenient and can damage devices. To overcome this problem, we used

critical point drying in CO_2. However, CO_2 has its own disadvantage and is not miscible with water. It is miscible with fluids like ethanol, acetone or IPA. So in order to critical point dry (CPD) the suspended samples, water must be replaced by the exchange fluid (isopropyl alcohol in our case). This dehydration is done gradually by transferring the suspended device into beakers with different concentrations of IPA and water (from IPA:Water – 20:80, 40:60, 60:40, 80:20, 0:100). Now the sample immersed in IPA can be placed into the CPD tool. The steps to using the CPD tool are as follows:

1. Turn on water cooler and set temp to 5-10℃.
2. Put suspended sample immersed in IPA into CPD sample holder and into CPD chamber.
3. Close all valves and slowly open CO_2 valve and crack open vent valve. Fill chamber with CO_2. (If you wait too long to do this step all the solvent will run out of the sample holder and your sample will dry out).
4. Now you need to replace all the solvent in the CPD with CO_2 so that the suspended flake does not collapse. This is done by leaving CO_2 valve and the bottom vent valve open. Watch the liquid level in the CPD chamber window to ensure that the sample is always submerged.
5. After venting the sample for 5 minutes close all valves and let the sample sit in liquid CO_2 for 30mins. Repeat the above step to ensure all IPA is displaced from inside the CPD chamber.
6. Now you need to take the CPD chamber to the critical point. This is done by first turning off the CO_2 and ramping up the temperature to 40℃.
7. Wait until the CPD chamber reaches 40℃ and slowly vent now-gaseous CO_2.

We use SEM to confirm that the monolayers are indeed suspended. Samples fabricated through this technique are shown in Fig. A10d and f. In Fig. A10d we can see monolayer MoS_2 being suspended across Ti/Au electrodes. Such suspended devices allowed us to remove detrimental substrate effects and experimentally measure the MoS_2 band gap and exciton binding energies [54]. The CPD technique can also be used to make graphene membranes as shown in Fig. A10e. A PMMA assisted technique can be used to first transfer graphene onto a pinhole. At the final step, when removing the PMMA with acetone, we follow our CPD technique to ensure that the membrane does not get collapse during the drying process.

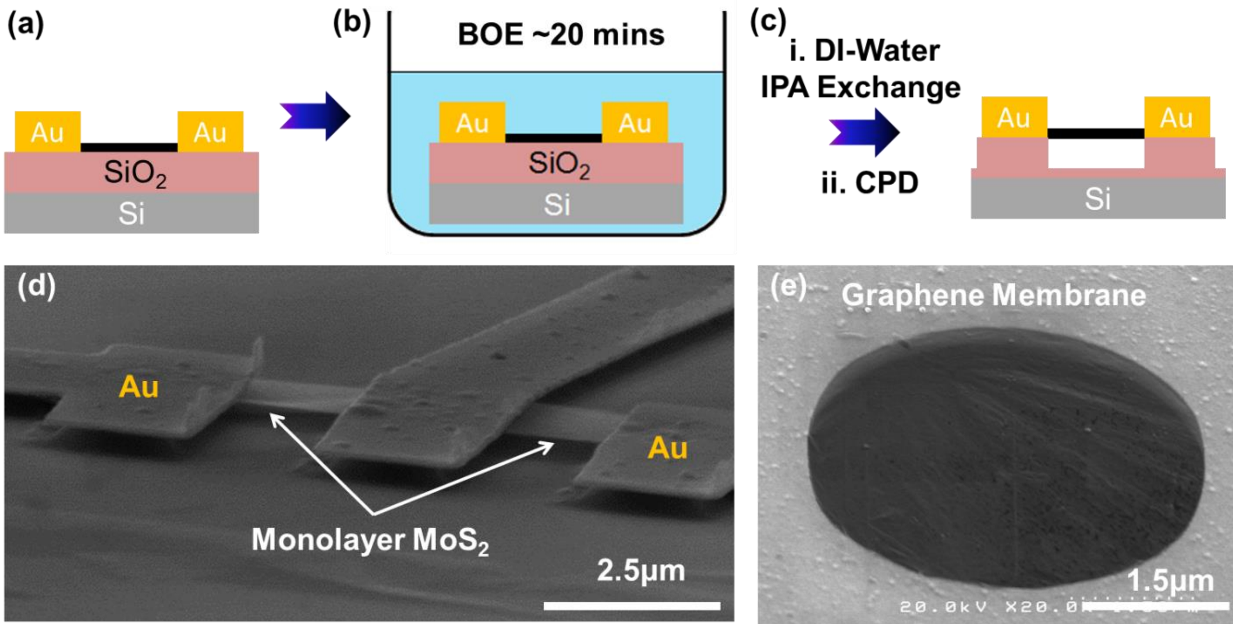

Figure A10 *Schematic illustration of fabrication process for electrically contacted suspended MoS_2 flakes (a) Illustration of Cr(2nm)/Au(90nm) contacted MoS_2 device. (b) Schematic of etching underlying SiO_2 in BOE bath (c) Illustration of suspended monolayer device after DI-water/IPA exchange and CPD process (d) SEM of as prepared suspended monolayer MoS_2 device (e) SEM of graphene membrane on Au/SiN pinhole prepared through wet PMMA transfer followed by CPD.*

iii. Polymer free transfer technique for TEM/STEM samples

In previous sections, all transfer techniques relied on PMMA-mediated transfer. The polymer mediated transfer required many wet chemical steps to clean the monolayer samples. For electron microscopy (TEM, STEM)[109] studies it is essential to develop a polymer-free technique to ensure that the flakes of 2D materials are unperturbed and clean.

Here, we discuss a method [27] to directly transfer large area CVD grown graphene onto Au 200M holey carbon (1.2/1.3µm diameter) quantifoil TEM grids purchased from SPI (SEM image of Quantifoil TEM Grid, Fig. A11a). This technique relies on using surface tension and evaporation to pull graphene/Cu into contact with the quantifoil TEM grid. The quantifoil TEM grid is placed directly onto a graphene/Cu with the holey carbon mesh directly in contact with the graphene. Best transfer is achieved when both the TEM grid and graphene/Cu foil are not crumpled ensuring good physical contact. A drop of IPA is drop cast on top of the TEM grid and left to evaporate (Fig. A11b-e). Once the IPA dries the monolayer of graphene on top of the Cu foil will attach itself to the holey carbon mesh. At this point, the TEM grid should not be moved or perturbed since this can cause the holey carbon mesh to rip. The TEM grid/foil is then placed on a hot plate at 200°C for 15 min, followed by $FeCl_3$ for 1~3 hours as necessary. Once the Cu is completely etched away, the monolayer of graphene remains attached to the TEM grid. The TEM Grid is placed in 10% HCl acid bath for 2 h then transferred over to a DI water bath. The sample is carefully fished out using self-closing TEM tweezers. The TEM grid should not be allowed to touch any lab surface. While it held with self-closing tweezers, 2-3 drops of IPA is gently placed on the TEM grid to clean it one final time. The sample is left to dry in air. A brightfield TEM image of a monolayer graphene film is shown in Fig. A11f. The TEM grid is then carefully stored in a TEM grid holder. This approach can also be used to pick up exfoliated

flakes on SiO_2/Si (Fig. A11 g-i). This process is a little trickier since it requires one to align the TEM grid over an exfoliated flake. This can be done under a microscope prior to the drop-casting IPA. Alignment has to be done in such a way so that the Au mesh on the TEM Grid does not cover the flake to be picked up. It is also useful to record an optical image of the TEM grid once the IPA has dried to assist in finding the flake later under a TEM/STEM microscope. Similar to the previous procedure, once the IPA has dried, the sandwich structure (TEM/flake/SiO_2) should be baked at 200℃ for 15 min to aid in adhesion. Finally, the underlying oxide can be etched away using BOE. The cleaning procedure is the same as earlier. SEM image of flakes picked up onto Quantifoil TEM grids through such a technique is shown in Fig. A11 i.

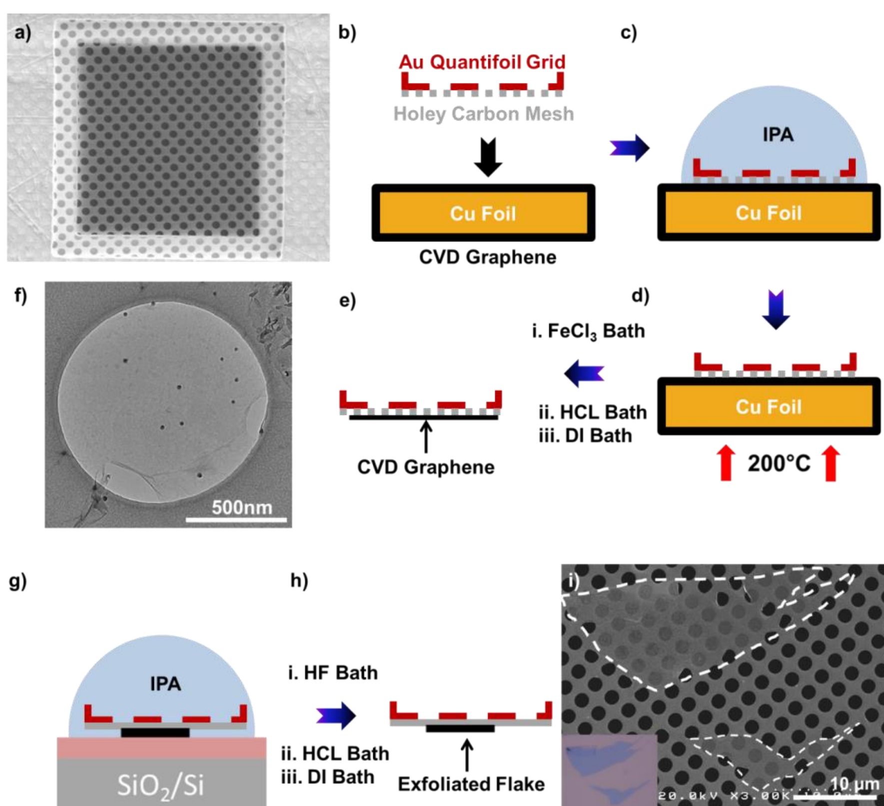

Figure A11 *Schematic of transferring monolayer graphene film onto TEM grids (a) SEM image of a Au Quantifoil TEM grid with holey carbon mesh (b) Illustration of how to place the quntifoil on top of*

graphene/Cu foil. The holey carbon mesh should be in contact with the graphene film (c) A drop of IPA is placed on top of the TEM grid to bring the graphene film into contact with the holey carbon mesh (d) Sample after IPA has dried (e) Quantifoil TEM grid with a film of graphene following Cu etch and HCl/DI water baths (f) Brightfield TEM image of graphene film suspended across holey carbon mesh. (g) Technique used to pick up individual flakes from SiO_2/Si substrates (h) Illustration of Quantifoil TEM grid with an individual monolayer flake (i) SEM image of a monolayer MoS_2 flake picked up onto a Quantifoil TEM grid. White dashed lines shows outline of flake on holey carbon mesh. Inset: same monolayer MoS_2 flakes on SiO_2/Si substrates prior to pickup

A6. Transfer of 2D material transfer using PDMS stamping

Traditionally heterostructures are typically created by advanced growth techniques such as molecular beam epitaxy. The ability to create artificially stacked 2D vertical- heterostructures with a clean interface can enable exploration of new material properties and potential applications. In our lab, we adopted a transfer technique from the work Zormer *et al.* [111]. This technique is based on directly stamping a 2D crystal on top of a desired target material. A standard procedure to transfer monolayer MoS_2 onto target BN flakes is given below:

i. Preparation of transfer slide:

A transparent transfer slide is made by placing a 1.2mm thick square piece of 20:1 polydimethylsiloxane (PDMS) on the end of a plain microscopic glass slide (Fig. A12a). The PDMS serves as a cushion during the transfer process and allows us to apply some pressure in case the target substrate and 2D crystal do not come into complete physical contact. Next we must add a layer of sacrificial polymer layer on top of the PDMS onto which we can exfoliate our 2D material. We use Elvacite 2550 acrylic resin dissolved in MIBK (7.5gm/50mL) as the sacrificial polymer layer. This polymer has a fairly low glass transition temperature (~36℃)

which means it can be easily melted onto the target substrate during the transfer process. Unfortunately the Elvacite polymer does not adhere well to the PDMS which causes problems during exfoliation. For this reason, we place a strip of transparent Scotch tape across the PDMS surface (Fig. A12b). The Elvacite is then spun at 3000rpm for 1 minute to yield ~1μm films top of the PDMS/Scotch tape structure. We then use standard exfoliation to deposit MoS_2 crystals on top of the polymer. Extra care must be taken during the exfoliation process since the polymer film is flimsy and can easily rip if either too much force is used during exfoliation or if the exfoliation tape is ripped off too fast. Flakes of MoS_2 can be easily identified and later verified using Raman microscopy (Inset: Fig. A12c). Small markers can be placed around the region with the monolayer flake to later assist in locating the flake.

ii. Transfer of 2D flakes

The target substrates with BN flakes were first cleaned using acetone and IPA. They are then annealed at ~250°C to remove any contaminants on the surface. The substrate with BN flakes is placed on a heated stage as shown schematically in Fig. A12d. The heated stage comprised of two heater cartridges and a thermocouple to monitor temperature. Our transparent glass slide with the MoS_2 flake is inverted and placed directly above the target using a custom built micromanipulator stage. This configuration (Fig. A12f) allows us to align the MoS_2 and target BN substrate under a confocal microscope. Once aligned, MoS_2 and BN target are brought into contact at room temperature and heated to 120°C. The PDMS/polymer layer is then mechanically separated from the MoS_2/QD stack at 80°C which detaches polymer/flake onto the target substrate. To remove the polymer residues, the device was soaked in acetone for ~ 1 hour and rinsed in IPA. An optical image of monolayer MoS_2 flake transferred on BN is shown in Fig. 1.14g. This technique can be used to transfer different 2D materials like graphene onto

plasmonic Au electrododes and even on SiN TEM grids with array of holes. If transferring solely onto Au electrodes, pre-cleaning the target substrate in piranha solution (1:3 H_2O_2:H_2SO_4) for 1 hour followed by O_2 plasma treatment (30s) significantly increases adhesion and yield of transfer.

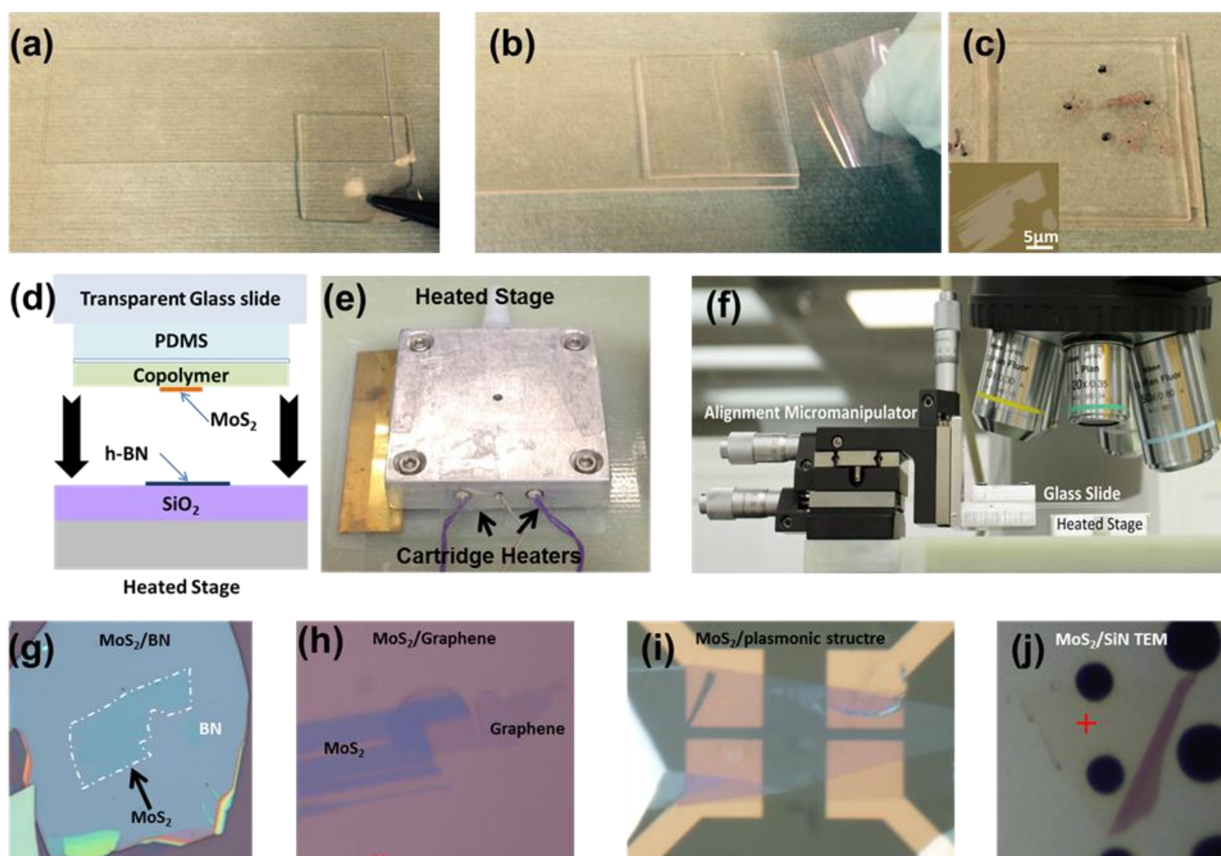

Figure A12 *(a)-(c) Transfer slide preparation steps (a) Placement of 20:1 PDMS square on the end of microscope glass slide (b) Pasting transparent Scotch tape on top of PDMS/glass slide (c) After mechanical exfoliation on ~1um thick Elvacite polymer/Scotch Tape/PDMS/glass slide. Monolayer flake is located roughly between four dots. Inset: Optical image of monolayer* MoS_2 *exfoliated on transfer slide (d) Schematic of transfer onto BN flakes sitting on* SiO_2*/Si substrate (e) Photo of heated stage used during transfer. Heated stage is fitted with two cartridge heaters and a thermocouple. Target substrates are placed facing up on center of heated stage (f) Full picture of a custom built transfer stage sitting under a*

microscope (g) Optical image of MoS_2 from (c) transferred onto BN flake using stamping procedure (h) Optical image of MoS_2/graphene heterostructure (i) Bilayer MoS_2 transferred on plasmonic device (j) MoS_2 selectively transferred over SiN membrane with holes for TEM measurement.

A7. He-cryostat for low temperature measurements:

All low temperature measurements presented in this thesis were done using a closed cycle He-cryostat from Cryogenic Limited. Such cryocoolers along with a variable temperature insert (VTI) allows us to cool our samples to low temperatures ~4K without the use of expensive liquid helium. Schematic diagram of VTI cooling circuit is given below (Fig. A13). Such closed cycle cryostat work by first compressing room temperature helium. The compressed helium is then cooled by expansion. The gas passes to the second stage of the cryo-cooler where it is cooled below 4.2K and condenses in the helium pot. Liquid helium then is passed through a needle valve and enters the main sample space. The helium is pumped back to the helium gas dump. The sample is inserted through an airlock inside a specifically designed vacuum probe. The outside of the probe is in contact with the VTI gas stream and the sample is cooled via a copper-link. The heat exchanger at the bottom of the VTI transfers heat to the sample.

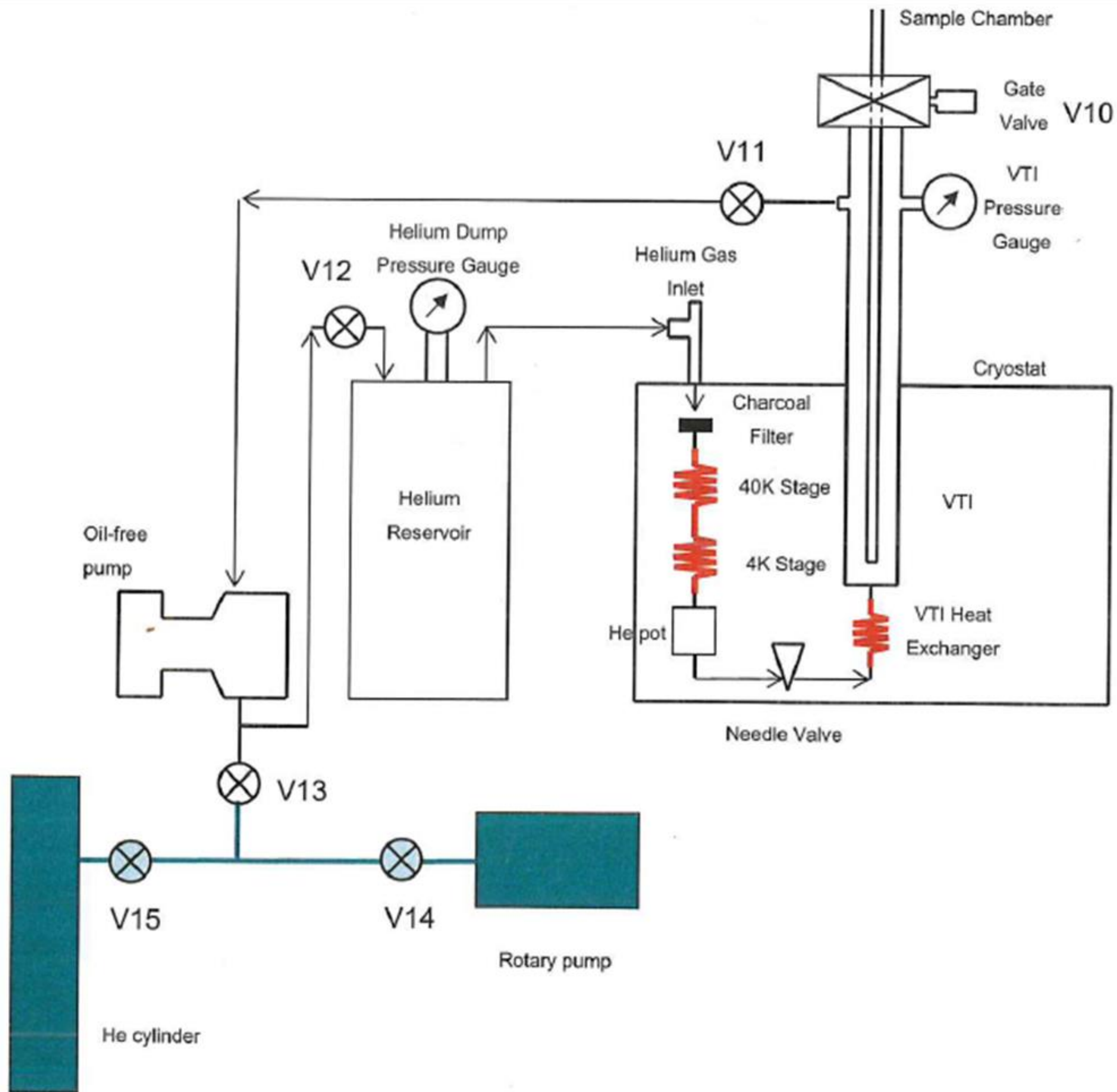

Figure A13 *Schematic of VTI cooling circuit*

i. System cooldown

In order to cool down the cryostat, the vacuum chamber (outer jacket) should be pumped out using a turbo pump capable of reaching base pressure below 10^{-5} mbar using preferably a short pumping line at least 25mm in diameter. This should be done overnight. The vacuum chamber can be accessed through the vacuum pumping port (Fig. A14)

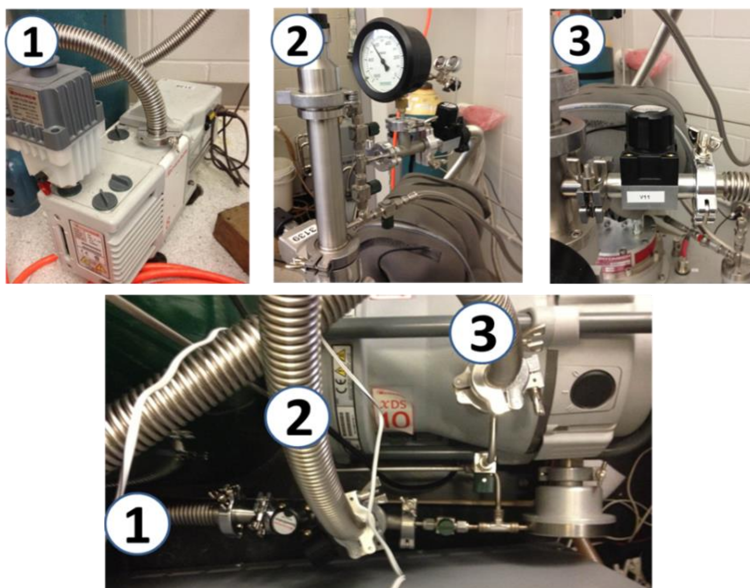

Figure A14 ***(a)*** *Turbo pump used to pump outer jacket* ***(b)*** *Configuration of rotary and scroll pump connected to VTI circuit*

ii. Flushing VTI circuit:

The next step is to ensure that the He circuit is clean. Even a small amount of contamination in the cooling circuit can clog the needle valve and hinder He flow necessary for cooldown. This is done by evacuating the VTI from both ends (Fig 3.5b). The rotary pump evacuates from the inlet end through the dump① while the the scroll pump evacuates from the top of the VTI③. The scroll and rotary pump should be connected as shown in Fig 3.5b.

1) Remove the sample and close the gate valve.
2) Open the needle valve
3) Check that V12 is open (This is the valve attached to the Helium dump).
4) Open V13 to atmosphere and allow the gas from the dump to escape. (V13 is the valve that connects the exhaust of the scroll pump to atmosphere).

5) Disconnect the pumping line from the air lock assembly. Connect this diffusion pump line to the flange behind V13.
6) Turn on the rotary pump.
7) Close the valve V16. This valve V16 bypasses the Scroll pump. V16 is connected from the front of the scroll pump to the pipe that goes to the He dump. V16 is closed so that the VTI circuit from the needle will be pumped by the scroll pump.
8) Open V11 and start the scroll pump(This is valve that is connected between the VTI circuit line and the scroll pump)

Once the VTI circuit has been pumped out for >6 hours, the needle valve can be closed. The scroll pump can also be closed. The He reservoir should be filled to 0.25 bar using the rotary pump and the gate valve. After this switch on flow of water to cool the compressor and ensure flow. We can then switch on the compressor and monitor the 1st stage temperature sensor. If the cryo-cooler is operating normally the temperature should drop at the rate of 5K/min. Once the 1st stage reaches 40K and 2nd stage reachers 4K the scroll pump can be turned on. The needle valve can now be opened to ~20mbar to cool the sample space through the VTI heat exchanger. Samples are mounted using the gate valve. First the sample space needs to be flushed with He several times using the rotary pump. Once the sample space has been flushed, it should be filled with 200mbar of He. The gate valve can now be opened and sample rod can be lowered.

A8. CdSSe QD Fabrication:

This one-pot synthetic procedure is based on a method published recently by Harrison *et al.*[60] First, 1 mmol CdO (0.128 g), 1.3 mL oleic acid (HOA), and 20 mL 1-octadecene (ODE) were heated to 100℃ under vacuum for 10 minutes, and subsequently purged with Ar. The

temperature was increased to 260℃ and the conversion of red CdO to colorless Cd-oleate was monitored to completion, after which the reaction temperature was reduced to 220℃. Solutions of S:Tributyl phosphate (0.75 M) and Se:Tributyl phosphate (0.75 M) in ODE were prepared separately and 0.8 mL aliquots of each were pulled into the same syringe. The S/Se aliquot was swiftly injected into the Cd-oleate flask at 220℃ and the reaction was allowed to proceed for 2hrs. The nanocrystals were cooled and precipitated with a 3:1 mixture of butanol and ethanol, resuspended in toluene, and precipitated twice more with pure ethanol. After being finally suspended in toluene, the nanocrystals were passed through a 0.45μm filter and stored.

A9. QD Layer Fabrication:

To overcome the challenge of physically bringing QDs and a 2DSC in close proximity, we developed a flexible approach to fabricate of uniform monolayer films of QDs. First, we used chemical self-assembly to deposit a uniform layer of QDs onto a SiO_2 substrate (Fig 5.2a). Then the SiO_2 substrate functionalized with (3-Mercaptopropyl) trimethoxysilane was submerged into a solution of oleic acid-ligated CdSSe QDs (Fig 5.2a).[112] The exposed thiol groups displace the oleic acid surface ligands and bind the QDs to the substrate.[113] Sub-monolayer films of CdSSe prepared through this method are shown in Fig. A15b. Photoluminescence image shows a uniform layer of QDs across a large area. With AFM we determined that the thickness of the QD film is ~7nm (Fig. A15b, Inset). This thickness is consistent with a sub-monolayer film of QDs that are ~5nm in diameter and have 1-2nm long oleic acid ligands.[71] Photoluminescence imaging indicates that as-fabricated QD films remain bright and are very uniform (Fig. A15b). Moreover, the position and the width of the PL peak for the QD film (Fig A15c, red line) do not

differ significantly from that of same QDs in solution (Fig A15c, black dotted line). This suggests that the

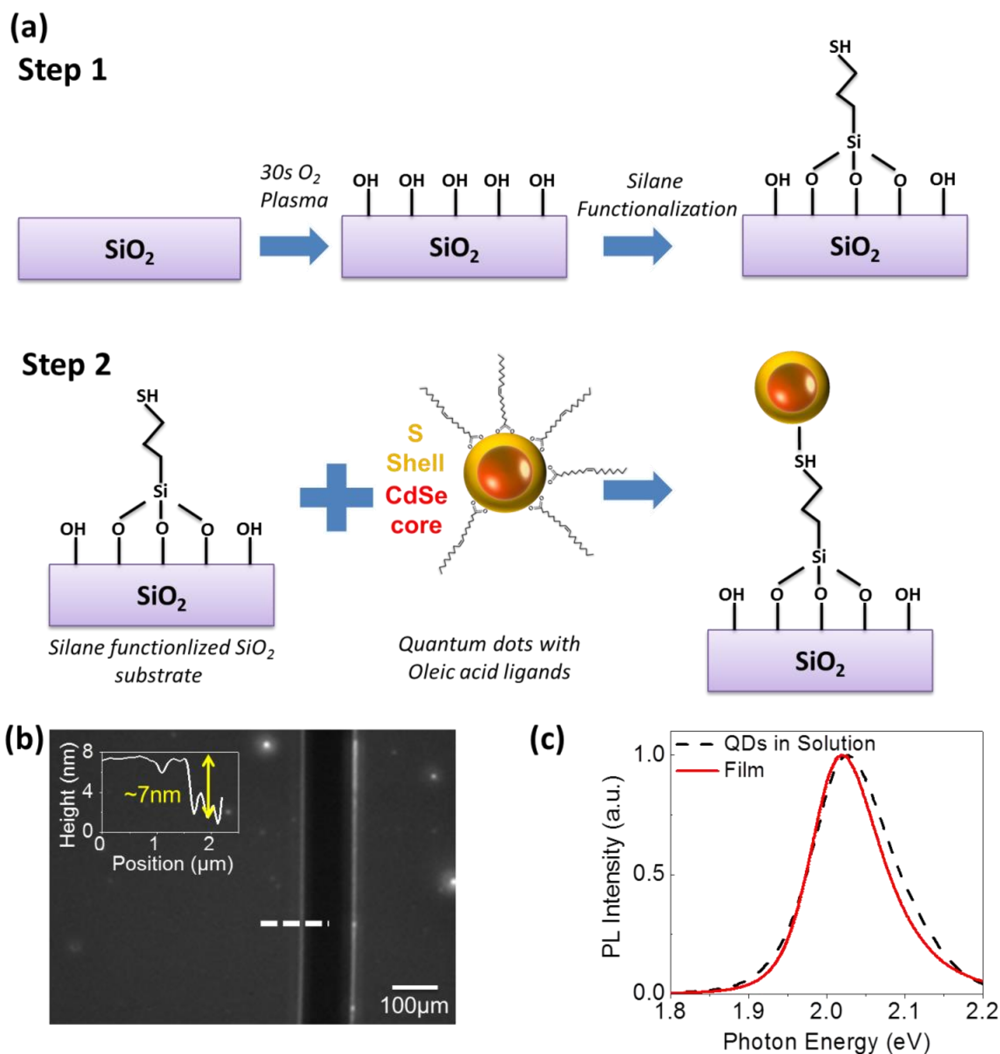

Figure A15 *(a) Schematic illustration of functionalization of SiO_2/Si substrates followed by self assembly of CdSSe QDs (b) PL image of a QD film. A striation made on the film is evident as a dark strip. Inset: AFM height profile of the film obtained along the white dashed line in (b).* ***(c)*** *Normalized PL spectra of a QD film on SiO_2 and of the same QDs in solution.*

A.10 Electrically contacted QD/MoS_2 Layer Fabrication:

Cr/Au (2nm/30nm) electrodes were deposited on SiO_2 substrates. The substrates were then cleaned in a piranha solution (1:3 H_2O_2:H_2SO_4) for 1 hour, made hydrophilic through O_2 plasma treatment (30s), and functionalized in 1mM solution of (3-Mercaptopropyl) trimethoxysilane in hexane for 10 min. Functionalized substrates were washed in a hexane bath for 1 min, rinsed in isopropanol, and blow-dried. To assemble a uniform film of QDs, functionalized substrates were placed into 5mg/ml solution of CdSSe for 30mins and rinsed gently afterwards with toluene. To transfer MoS_2 onto QDs, we followed the recipe developed by Zomer *et al.* [111] discussed in chapter 1. We spun Elvacite polymer (~1μm thick) onto PDMS/clear Scotch tape sandwich structure. The structure was baked at 90℃ for 5mins. Monolayer MoS_2 was exfoliated onto Elvacite and verified using optical microscopy and Raman spectroscopy. MoS_2 was aligned with Au electrodes, brought into contact with QD films and baked at 120℃. The PDMS/polymer layer was then mechanically separated from the MoS_2/QD stack. To remove the polymer residues, the MoS_2/QD stack was soaked in acetone for 15 min. Finally, we created the solid electrolyte gate by placing a drop of $CsClO_4$ salt in poly(ethylene) oxide (PEO) matrix dissolved in acetonitrile and drying it for 2hrs at room temperature. A second gate electrode close to MoS_2 was used to contact the solid electrolyte.

A11. Polymer-electrolyte ionic gating

In MoS_2-FETs fabricated on SiO_2/Si devices, the highest achievable carrier densities are $\sim 7 \times 10^{12} cm^2$. This is limited by the voltage one can apply before the dielectric breaks down. Factors limiting mobility and resistivity can be significantly different at high n as observed in graphene[114, 115]. In fact, a transition into a superconductive phase in multilayer MoS_2 has been observed at high n through electrolyte gating[116]. It is therefore of great interest to study

transport at high *n.* To overcome the obstacle posed by breakdown of SiO_2 dielectric, we can take advantage of an electrochemical concept called an electric double layer (EDL) that is formed when a conductive material is immersed in an electrolyte.

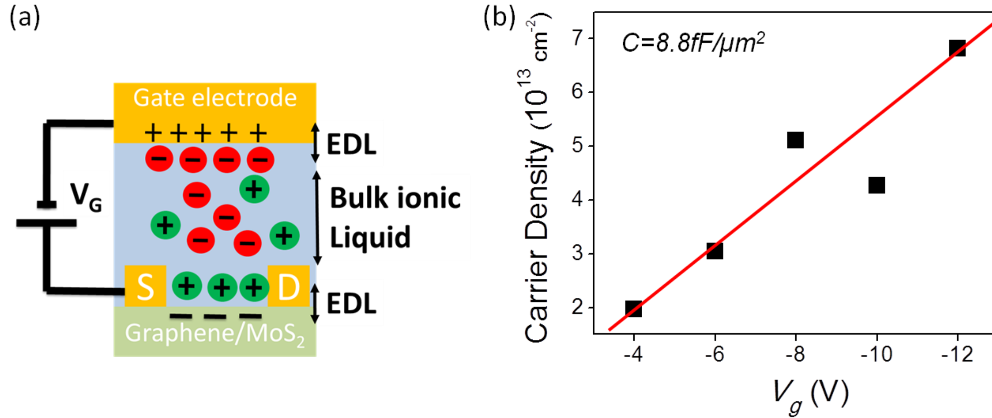

Figure A16 *(a) Schematic of polymer electrolyte gating in a typical Graphene/MoS_2 FET. EDL ~1nm. (b) Measured Carrier density n in a graphene-FET. Measured capacitance ~ 1µFcm^{-2}.*

Practically, we realize EDL gating by dissolving a salt like $CsClO_4$ in conductive poly(ethylene) and drop casting it onto MoS_2-FETs.[117] When we apply positive bias to the polymer electrolyte, Li^+ and ClO_4^- ions can percolate within the matrix and form an EDL with the metal electrode as shown in Fig A16a. We verified the capacitance value to be ~1µFcm^{-2} using a Hall shaped graphene-FET, Fig A16b. This system now allows us to look at electrical transport at high *n*.

REFERENCES

1. Novoselov, K.S., et al., *Electric field effect in atomically thin carbon films.* Science, 2004. **306**(5696): p. 666-669.
2. Geim, A.K. and K.S. Novoselov, *The rise of graphene.* Nat Mater, 2007. **6**(3): p. 183-191.
3. Splendiani, A., et al., *Emerging Photoluminescence in Monolayer MoS_2.* Nano Letters, 2010. **10**(4): p. 1271-1275.
4. Mak, K.F., et al., *Atomically Thin MoS2: A New Direct-Gap Semiconductor.* Physical Review Letters, 2010. **105**(13): p. 136805.
5. RadisavljevicB, et al., *Single-layer MoS_2 transistors.* Nat Nano, 2011. **6**(3): p. 147-150.
6. Mak, K.F., et al., *Atomically Thin MoS2: A New Direct-Gap Semiconductor.* Physical Review Letters, 2010. **105**(13).
7. Novoselov, K.S., et al., *Two-dimensional atomic crystals.* Proceedings of the National Academy of Sciences of the United States of America, 2005. **102**(30): p. 10451-10453.
8. Kaasbjerg, K., K.S. Thygesen, and K.W. Jacobsen, *Phonon-limited mobility in n-type single-layer MoS2 from first principles.* Physical Review B, 2012. **85**(11): p. 115317.
9. Castro Neto, A.H., et al., *The electronic properties of graphene.* Reviews of Modern Physics, 2009. **81**(1): p. 109-162.
10. Dean, C.R., et al., *Boron nitride substrates for high-quality graphene electronics.* Nat Nano, 2010. **5**(10): p. 722-726.
11. Lu, C.-P., et al., *Bandgap, Mid-Gap States, and Gating Effects in MoS_2.* Nano Letters, 2014. **14**(8): p. 4628-4633.

12. Zhang, Y., et al., *Direct observation of a widely tunable bandgap in bilayer graphene.* Nature, 2009. **459**(7248): p. 820-823.

13. Novoselov, K.S., et al., *Two-dimensional gas of massless Dirac fermions in graphene.* Nature, 2005. **438**(7065): p. 197-200.

14. Bolotin, K.I., et al., *Ultrahigh electron mobility in suspended graphene.* Solid State Communications, 2008. **146**(9-10): p. 351-355.

15. Kim, K.S., et al., *Large-scale pattern growth of graphene films for stretchable transparent electrodes.* Nature, 2009. **457**(7230): p. 706-710.

16. Wang, Q.H., et al., *Electronics and optoelectronics of two-dimensional transition metal dichalcogenides.* Nat Nano, 2012. **7**(11): p. 699-712.

17. Kaasbjerg, K., K.S. Thygesen, and K.W. Jacobsen, *Phonon-limited mobility in n-type single-layer MoS${}_{2}$ from first principles.* Physical Review B, 2012. **85**(11): p. 115317.

18. Jariwala, D., et al., *Emerging Device Applications for Semiconducting Two-Dimensional Transition Metal Dichalcogenides.* ACS Nano, 2014. **8**(2): p. 1102-1120.

19. Cheiwchanchamnangij, T. and W.R.L. Lambrecht, *Quasiparticle band structure calculation of monolayer, bilayer, and bulk MoS2.* Physical Review B, 2012. **85**(20): p. 205302.

20. Newaz, A.K.M., et al., *Electrical control of optical properties of monolayer* MoS_2. Solid State Communications, 2013. **155**(0): p. 49-52.

21. Prasai, D., et al., *Graphene: Corrosion-Inhibiting Coating.* Acs Nano, 2012. **6**(2): p. 1102-1108.

22. Prasai, D., et al., *Electrical Control of near-Field Energy Transfer between Quantum Dots and Two-Dimensional Semiconductors.* Nano Letters, 2015. **15**(7): p. 4374-4380.

23. Jones, D.A., *Principles and Prevention of Corrosion*. 2nd ed1995, New Jersey: Prentica Hall.

24. Chen, J.-H., et al., *Intrinsic and extrinsic performance limits of graphene devices on SiO2.* Nat Nano, 2008. **3**(4): p. 206-209.

25. Newaz, A.K.M., et al., *Probing charge scattering mechanisms in suspended graphene by varying its dielectric environment.* Nat Commun, 2012. **3**: p. 734.

26. Almand-Hunter, A.E., et al., *Quantum droplets of electrons and holes.* Nature, 2014. **506**(7489): p. 471-475.

27. Regan, W., et al., *A direct transfer of layer-area graphene.* Applied Physics Letters, 2010. **96**(11): p. 113102.

28. Mansfeld, F., *Electrochemical impedance spectroscopy (EIS) as a new tool for investigating methods of corrosion protection.* Electrochimica Acta, 1990. **35**(10): p. 1533-1544.

29. D Talbot, J.T., *Corrosion Science and Technology*. 2nd ed1998, New York: CRC Press.

30. Bard, A.J.F., L.R., *Electrochecmical Methods: Fundamentals and Applications*. 2nd Edition ed2000, New York: Wiley.

31. Kuila, T., et al., *A green approach for the reduction of graphene oxide by wild carrot root.* Carbon, 2012. **50**(3): p. 914-921.

32. Fan, Z., et al., *An environmentally friendly and efficient route for the reduction of graphene oxide by aluminum powder.* Carbon, 2010. **48**(5): p. 1686-1689.

33. Kaushik, N., et al., *Schottky barrier heights for Au and Pd contacts to MoS2.* Applied Physics Letters, 2014. **105**(11): p. 113505.

34. Das, S., et al., *High Performance Multilayer MoS2 Transistors with Scandium Contacts.* Nano Letters, 2013. **13**(1): p. 100-105.

35. Liu, W., et al., *Role of Metal Contacts in Designing High-Performance Monolayer n-Type WSe2 Field Effect Transistors.* Nano Letters, 2013. **13**(5): p. 1983-1990.

36. Jariwala, D., et al., *Band-like transport in high mobility unencapsulated single-layer MoS2 transistors.* Applied Physics Letters, 2013. **102**(17): p. -.

37. Mark, R.G., et al., *Experimental study of the Ioffe-Regel criterion for amorphous indium oxide films.* Journal of Physics: Condensed Matter, 1998. **10**(4): p. 809.

38. Radisavljevic, B. and A. Kis, *Mobility engineering and a metal–insulator transition in monolayer MoS2.* Nat Mater, 2013. **12**(9): p. 815-820.

39. Dean, C.R., et al., *Boron nitride substrates for high-quality graphene electronics.* Nature Nanotechnology, 2010. **5**(10): p. 722-726.

40. Xue, J., et al., *Scanning tunnelling microscopy and spectroscopy of ultra-flat graphene on hexagonal boron nitride.* Nature Materials, 2011. **10**(4): p. 282-285.

41. Liu, A.S., et al., *A high-speed silicon optical modulator based on a metal-oxide-semiconductor capacitor.* Nature, 2004. **427**(6975): p. 615-618.

42. Miller, D.A.B., et al., *Band-Edge Electroabsorption in Quantum Well Structures - the Quantum-Confined Stark-Effect.* Physical Review Letters, 1984. **53**(22): p. 2173-2176.

43. Kuo, Y.H., et al., *Strong quantum-confined Stark effect in germanium quantum-well structures on silicon.* Nature, 2005. **437**(7063): p. 1334-1336.

44. Liu, M., et al., *A graphene-based broadband optical modulator.* Nature, 2011. **474**(7349): p. 64-67.

45. Klingshirn, C.F., *Semiconductor Optics* 2007, New York: Springer.

46. Wang, F., et al., *Gate-Variable Optical Transitions in Graphene.* Science, 2008. **320**(5873): p. 206-209.

47. Schmitt-Rink, S., D.S. Chemla, and D.A.B. Miller, *Theory of transient excitonic optical nonlinearities in semiconductor quantum-well structures.* Physical Review B, 1985. **32**(10): p. 6601-6609.

48. Mak, K.F., et al., *Tightly bound trions in monolayer* MoS_2. Nat Mater, 2013. **12**(3): p. 207-211.

49. Ross, J.S., et al., *Electrical control of neutral and charged excitons in a monolayer semiconductor.* Nat Commun, 2013. **4**: p. 1474.

50. Swathi, R.S. and K.L. Sebastian, *Long range resonance energy transfer from a dye molecule to graphene has (distance)*$^{-4}$ *dependence.* The Journal of Chemical Physics, 2009. **130**(8): p. 086101.

51. Clegg, R.M., *Chapter 1 Förster resonance energy transfer—FRET what is it, why do it, and how it's done*, in *Laboratory Techniques in Biochemistry and Molecular Biology*, T.W.J. Gadella, Editor 2009, Elsevier. p. 1-57.

52. Federspiel, F., et al., *Distance dependence of the energy transfer rate from a single semiconductor nanostructure to graphene.* Nano Lett, 2015. **15**(2): p. 1252-8.

53. Mak, K., et al., *Atomically Thin* MoS_2*: A New Direct-Gap Semiconductor.* Physical Review Letters, 2010. **105**(13): p. 136805.

54. Klots, A.R., et al., *Probing excitonic states in suspended two-dimensional semiconductors by photocurrent spectroscopy.* Sci. Rep., 2014. **4**: p. 6608.

55. Chernikov, A., et al., *Exciton Binding Energy and Nonhydrogenic Rydberg Series in Monolayer WS_2.* Physical Review Letters, 2014. **113**(7): p. 076802.

56. Ye, Z., et al., *Probing excitonic dark states in single-layer tungsten disulphide.* Nature, 2014. **513**(7517): p. 214-218.

57. Molina-Sánchez, A., et al., *Effect of spin-orbit interaction on the optical spectra of single-layer, double-layer, and bulk MoS_2.* Physical Review B, 2013. **88**(4): p. 045412.

58. Zhang, C., et al., *Absorption of light by excitons and trions in monolayers of metal dichalcogenide MoS_2: Experiments and theory.* Physical Review B, 2014. **89**(20): p. 205436.

59. Schmitt-Rink, S., D.S. Chemla, and D.A.B. Miller, *Linear and nonlinear optical properties of semiconductor quantum wells.* Advances in Physics, 1989. **38**(2): p. 89-188.

60. Harrison, M.A., et al., *CdSSe Nanocrystals with Induced Chemical Composition Gradients.* Israel Journal of Chemistry, 2012. **52**(11-12): p. 1063-1072.

61. Hemdana, I., M. Mahdouani, and R. Bourguiga, *Investigation of the radiative lifetime in core–shell CdSe/ZnS and CdSe/ZnSe quantum dots.* Physica B: Condensed Matter, 2012. **407**(17): p. 3313-3319.

62. Korn, T., et al., *Low-temperature photocarrier dynamics in monolayer MoS_2.* Applied Physics Letters, 2011. **99**(10): p. 102109.

63. Chen, Z., et al., *Energy Transfer from Individual Semiconductor Nanocrystals to Graphene.* ACS Nano, 2010. **4**(5): p. 2964-2968.

64. Prins, F., A.J. Goodman, and W.A. Tisdale, *Reduced Dielectric Screening and Enhanced Energy Transfer in Single- and Few-Layer MoS_2.* Nano Letters, 2014. **14**(11): p. 6087-6091.

65. Larentis, S., et al., *Band Offset and Negative Compressibility in Graphene-MoS2 Heterostructures.* Nano Letters, 2014. **14**(4): p. 2039-2045.

66. Efetov, D., et al., *Multiband transport in bilayer graphene at high carrier densities.* Physical Review B, 2011. **84**(16): p. 161412.

67. Empedocles, S., D. Norris, and M. Bawendi, *Photoluminescence Spectroscopy of Single CdSe Nanocrystallite Quantum Dots.* Physical Review Letters, 1996. **77**(18): p. 3873-3876.

68. Sharma, S.N., Z.S. Pillai, and P.V. Kamat, *Photoinduced Charge Transfer between CdSe Quantum Dots and p-Phenylenediamine.* The Journal of Physical Chemistry B, 2003. **107**(37): p. 10088-10093.

69. Jha, P.P. and P. Guyot-Sionnest, *Photoluminescence Switching of Charged Quantum Dot Films.* The Journal of Physical Chemistry C, 2007. **111**(42): p. 15440-15445.

70. Jha, P.P. and P. Guyot-Sionnest, *Electrochemical Switching of the Photoluminescence of Single Quantum Dots.* The Journal of Physical Chemistry C, 2010. **114**(49): p. 21138-21141.

71. Gunawan, A.A., et al., *Ligands in PbSe Nanocrystals: Characterizations and Plasmonic Interactions.* Microscopy and Microanalysis, 2013. **19**(SupplementS2): p. 1506-1507.

72. Li, S., M.L. Steigerwald, and L.E. Brus, *Surface States in the Photoionization of High-Quality CdSe Core/Shell Nanocrystals.* ACS Nano, 2009. **3**(5): p. 1267-1273.

73. Paul, A., et al., *Distance Dependence of the Charge Transfer Rate for Peptide Nucleic Acid Monolayers.* The Journal of Physical Chemistry B, 2010. **114**(45): p. 14140-14148.

74. Geick, R., C.H. Perry, and G. Rupprecht, *Normal Modes in Hexagonal Boron Nitride.* Physical Review, 1966. **146**(2): p. 543-547.

75. Chen, X., et al., *Probing the electron states and metal-insulator transition mechanisms in molybdenum disulphide vertical heterostructures.* Nat Commun, 2015. **6**: p. 6088.

76. Zhao, W., et al., *Evolution of Electronic Structure in Atomically Thin Sheets of WS2 and WSe2.* ACS Nano, 2013. **7**(1): p. 791-797.

77. Liu, S., et al., *Exciton storage in CdSe/CdS tetrapod semiconductor nanocrystals: Electric field effects on exciton and multiexciton states.* Physical Review B, 2012. **86**(4): p. 045303.

78. Bennett, A.J., et al., *Giant Stark effect in the emission of single semiconductor quantum dots.* Applied Physics Letters, 2010. **97**(3): p. 031104.

79. van der Zande, A.M., et al., *Grains and grain boundaries in highly crystalline monolayer molybdenum disulphide.* Nat Mater, 2013. **12**(6): p. 554-561.

80. Lee, Y.-H., et al., *Synthesis of Large-Area MoS_2 Atomic Layers with Chemical Vapor Deposition.* Advanced Materials, 2012. **24**(17): p. 2320-2325.

81. Lopez-Sanchez, O., et al., *Ultrasensitive photodetectors based on monolayer MoS2.* Nat Nano, 2013. **8**(7): p. 497-501.

82. Yin, Z., et al., *Single-Layer MoS2 Phototransistors.* ACS Nano, 2012. **6**(1): p. 74-80.

83. Lee, H.S., et al., *MoS2 Nanosheet Phototransistors with Thickness-Modulated Optical Energy Gap.* Nano Letters, 2012. **12**(7): p. 3695-3700.

84. Sundaram, R.S., et al., *Electroluminescence in Single Layer MoS_2.* Nano Letters, 2013. **13**(4): p. 1416-1421.

85. Conley, H.J., et al., *Bandgap Engineering of Strained Monolayer and Bilayer MoS2.* Nano Letters, 2013. **13**(8): p. 3626-3630.

86. Feng, J., et al., *Strain-engineered artificial atom as a broad-spectrum solar energy funnel.* Nat Photon, 2012. **6**(12): p. 866-872.

87. !!! INVALID CITATION !!!

88. Ramasubramaniam, A., D. Naveh, and E. Towe, *Tunable band gaps in bilayer transition-metal dichalcogenides.* Physical Review B, 2011. **84**(20): p. 205325.

89. Liu, Q., et al., *Tuning Electronic Structure of Bilayer MoS2 by Vertical Electric Field: A First-Principles Investigation.* The Journal of Physical Chemistry C, 2012. **116**(40): p. 21556-21562.

90. Polman, A. and H.A. Atwater, *Photonic design principles for ultrahigh-efficiency photovoltaics.* Nat Mater, 2012. **11**(3): p. 174-177.

91. Hattori, Y., et al., *Layer-by-Layer Dielectric Breakdown of Hexagonal Boron Nitride.* Acs Nano, 2015. **9**(1): p. 916-921.

92. Fallah, H.R., et al., *The effect of annealing on structural, electrical and optical properties of nanostructured ITO films prepared by e-beam evaporation.* Materials Research Bulletin, 2007. **42**(3): p. 487-496.

93. Mak, K.F., et al., *Measurement of the Optical Conductivity of Graphene.* Physical Review Letters, 2008. **101**(19).

94. Nair, R.R., et al., *Fine structure constant defines visual transparency of graphene.* Science, 2008. **320**(5881): p. 1308-1308.

95. Tongay, S., et al., *Defects activated photoluminescence in two-dimensional semiconductors: interplay between bound, charged, and free excitons.* Scientific Reports, 2013. **3**: p. 2657.

96. Blake, P., et al., *Making graphene visible.* Applied Physics Letters, 2007. **91**(6): p. 063124-3.

97. Ferrari, A.C., et al., *Raman Spectrum of Graphene and Graphene Layers.* Physical Review Letters, 2006. **97**(18): p. 187401.

98. Malard, L.M., et al., *Raman spectroscopy in graphene.* Physics Reports, 2009. **473**(5–6): p. 51-87.

99. Ferrari, A.C., *Raman spectroscopy of graphene and graphite: Disorder, electron–phonon coupling, doping and nonadiabatic effects.* Solid State Communications, 2007. **143**(1–2): p. 47-57.

100. Lee, C., et al., *Anomalous Lattice Vibrations of Single- and Few-Layer MoS2.* ACS Nano, 2010. **4**(5): p. 2695-2700.

101. Molina-Sánchez, A. and L. Wirtz, *Phonons in single-layer and few-layer MoS2 and WS2.* Physical Review B, 2011. **84**(15): p. 155413.

102. Li, X., et al., *Large-Area Synthesis of High-Quality and Uniform Graphene Films on Copper Foils.* Science, 2009. **324**(5932): p. 1312-1314.

103. Mattevi, C., H. Kim, and M. Chhowalla, *A review of chemical vapour deposition of graphene on copper.* Journal of Materials Chemistry, 2011. **21**(10): p. 3324-3334.

104. Chen, Z., et al., *Three-dimensional flexible and conductive interconnected graphene networks grown by chemical vapour deposition.* Nat Mater, 2011. **10**(6): p. 424-428.

105. Dong, X., et al., *3D Graphene Foam as a Monolithic and Macroporous Carbon Electrode for Electrochemical Sensing.* ACS Applied Materials & Interfaces, 2012. **4**(6): p. 3129-3133.

106. Crowder, S.W., et al., *Three-dimensional graphene foams promote osteogenic differentiation of human mesenchymal stem cells.* Nanoscale, 2013. **5**(10): p. 4171-4176.

107. Zhan, Y., et al., *Large-Area Vapor-Phase Growth and Characterization of MoS2 Atomic Layers on a SiO2 Substrate.* Small, 2012. **8**(7): p. 966-971.

108. Li, X., et al., *Transfer of Large-Area Graphene Films for High-Performance Transparent Conductive Electrodes.* Nano Letters, 2009. **9**(12): p. 4359-4363.

109. Burson, K.M., et al., *Direct Imaging of Charged Impurity Density in Common Graphene Substrates.* Nano Letters, 2013. **13**(8): p. 3576-3580.

110. Suk, J.W., et al., *Transfer of CVD-Grown Monolayer Graphene onto Arbitrary Substrates.* ACS Nano, 2011. **5**(9): p. 6916-6924.

111. Zomer, P.J., et al., *A transfer technique for high mobility graphene devices on commercially available hexagonal boron nitride.* Applied Physics Letters, 2011. **99**(23): p. 232104.

112. Zhu, M.-Q., et al., *Surface modification and functionalization of semiconductor quantum dots through reactive coating of silanes in toluene.* Journal of Materials Chemistry, 2007. **17**(8): p. 800-805.

113. Ravindran, S., et al., *Covalent Coupling of Quantum Dots to Multiwalled Carbon Nanotubes for Electronic Device Applications.* Nano Letters, 2003. **3**(4): p. 447-453.

114. Efetov, D.K. and P. Kim, *Controlling Electron-Phonon Interactions in Graphene at Ultrahigh Carrier Densities.* Physical Review Letters, 2010. **105**(25): p. 256805.

115. Pachoud, A., et al., *Graphene transport at high carrier densities using a polymer electrolyte gate.* EPL (Europhysics Letters), 2010. **92**(2): p. 27001.

116. Ye, J.T., et al., *Superconducting Dome in a Gate-Tuned Band Insulator.* Science, 2012. **338**(6111): p. 1193-1196.

117. Efetov, D.K., et al., *Multiband transport in bilayer graphene at high carrier densities.* Physical Review B, 2011. **84**(16): p. 161412.